The Harvard Center for Biological Imaging Presents

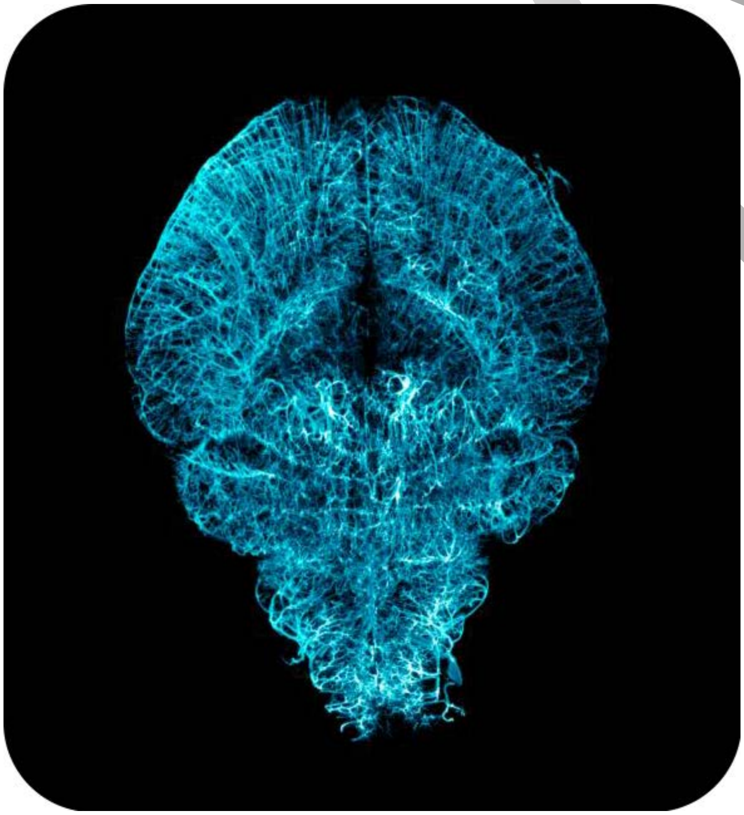

Tissue Clearing Workshop 2024

January 22-24
Harvard University
Cambridge, MA

TABLE OF CONTENTS

To connect to WIFI
Connect to "eduroam"
or connect to "Harvard University" and visit getonline.harvard.edu

Welcome

Welcome to the Harvard Center for Biological Imaging and our forth Tissue Clearing Workshop! Over the next three days we will investigate a number of techniques and concepts related to the field of tissue clearing. We will hear insights and technology updates from many of the leaders in the field and provide you with access to some of the most cutting-edge microscopy technologies available. We hope you will leave this course with the confidence to use these techniques and imaging systems to the best of your abilities.

We look forward to working with you and hope you enjoy your time here!

Douglas Richardson	**Heather Brown-Harding**	**Alex Lovely**	**Linda Liang**
Director of Imaging	Imaging Specialist	Imaging Specialist	Embedded Specialist
HCBI	HCBI	HCBI	HCBI/Zeiss

8:30 AM	Registration	Coffee	Coffee
9:00 AM	Welcome & Announcements	Annoucements	Announcements
9:15 AM	Jeff Lichtman	Adam Glaser	Ed Boyden
9:45 AM	Kwanghun Chung	Fabian Voigt	Erin Diel
10:15 AM	*Coffee Break*	*Coffee Break*	*Coffee Break*
10:30 AM	Elizabeth Engle & Gabriela Carrillo	Ya-chieh Hsu	Doug Richardson
11:00 AM	Li Ye	Ted Zwang	Observation and discussion of samples from Clearing Lab
11:30 PM	David Wong-Campos, Nika Gvazava		Chetan Poudel + Soheila Sabouri +Charles Gora
12:00 PM	*Lunch*	*Lunch*	*Lunch Sponsored by* ***Logos Biosystems***
1:00 PM	Clearing Lab Biological Labs Rms 5096 and 5088	Rotation #1	Rotation #5
2:00 PM		Rotation #2	Rotation #6
3:00 PM		*Break*	*Break*
3:15 PM		Rotation #3	Rotation #7
4:15 PM		Rotation #4	Rotation #8
6:00 PM	*Networking Dinner* *Sponsored by* ***ZEISS*** *Harvard Faculty Club* *20 Quincy St, Cambridge*		

Hands-on Groups

GROUP 1	**GROUP 2**	**GROUP 3**
Taeyong Ahn	Sara Lelek-Greskovic	April Reedy
Martina Krakora Compagno	Adrienne Wells	Xiaomeng Han
Steven Zwick	Benjamin Holmes	Shabnam Ghiasvand
Mandira Katuwal	Andrew Stone	Asier Marcos Vidal
Gayani Senevirathne	Michael Fernandes de Almeida	Khadija El Jellas
Reena Paink	Mohammed Mahamdeh	

GROUP 4	**GROUP 5**	**GROUP 6**
Charles Gora	Manalee Surve	Juan Tapia
Felix Sigmund	Christine Mirjam Molenda	Diego Ramirez
Jaime David Wong Campos	Nikolai Hoermann	Rachel Davis
Eric Moult	Nika Gvazava	Alexis Franklin
Soheila Sabouri	Changwoo Seo	Fadwa Joud

GROUP 7	**GROUP 8**
Chetan Poudel	Aqua Asberry
Zuri Sullivan	Katie Shirley
Wai-Man Chan	Humbert Ibarra
Dharmendra Puri	Yifan Liu
Gabby Carrillo	Aniwat Juhong

Important Locations

52 Oxford
Underground Parking

Northwest Building
B103 Lecture Hall (tues)

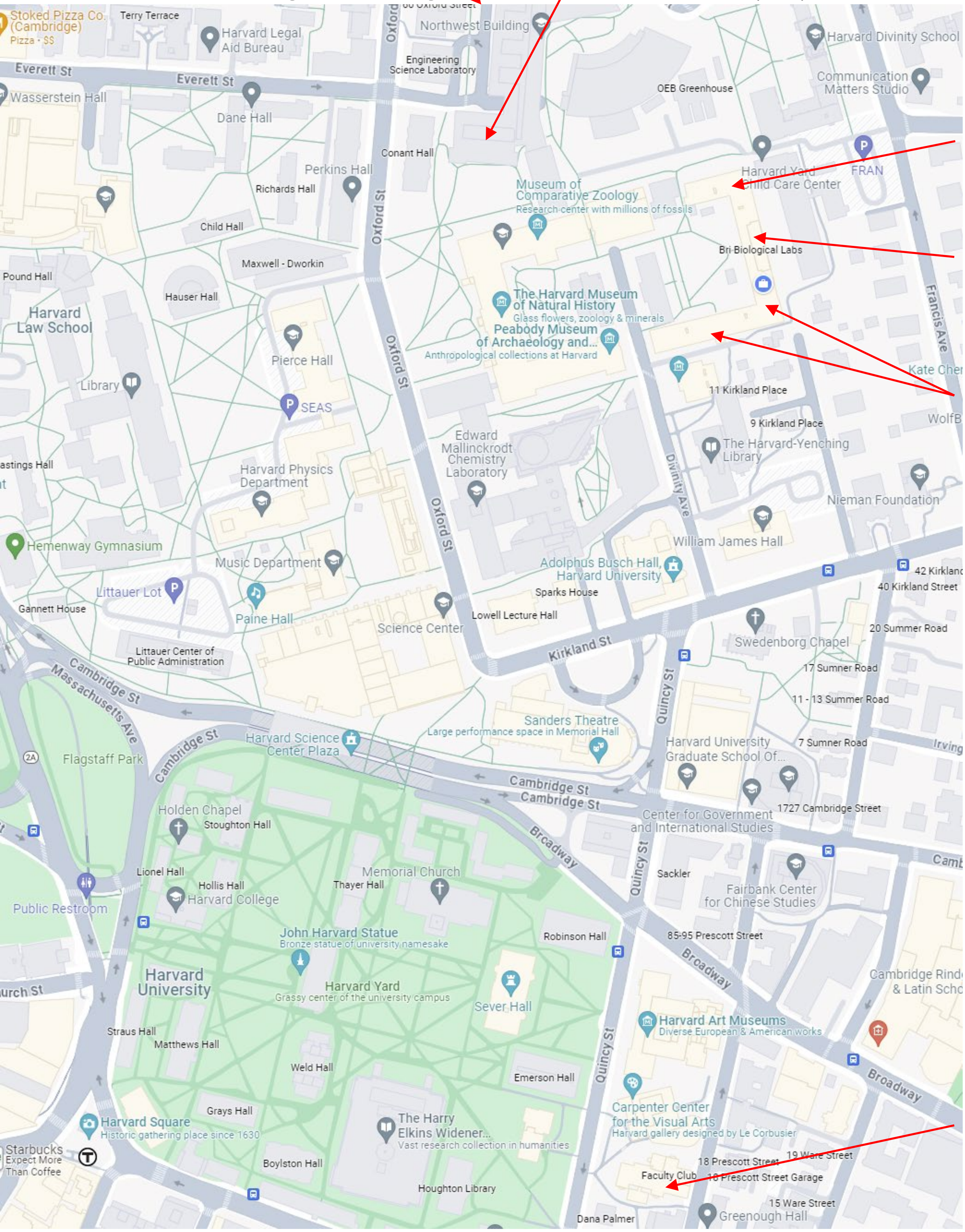

Biolabs 5088
Wet Lab

Biolabs 1080
Lecture Hall
(mon, wed)

Microscope
demos1st and
2nd floors

Networking
Dinner
Faculty Club,
20 Quincy St.

FIRST FLOOR

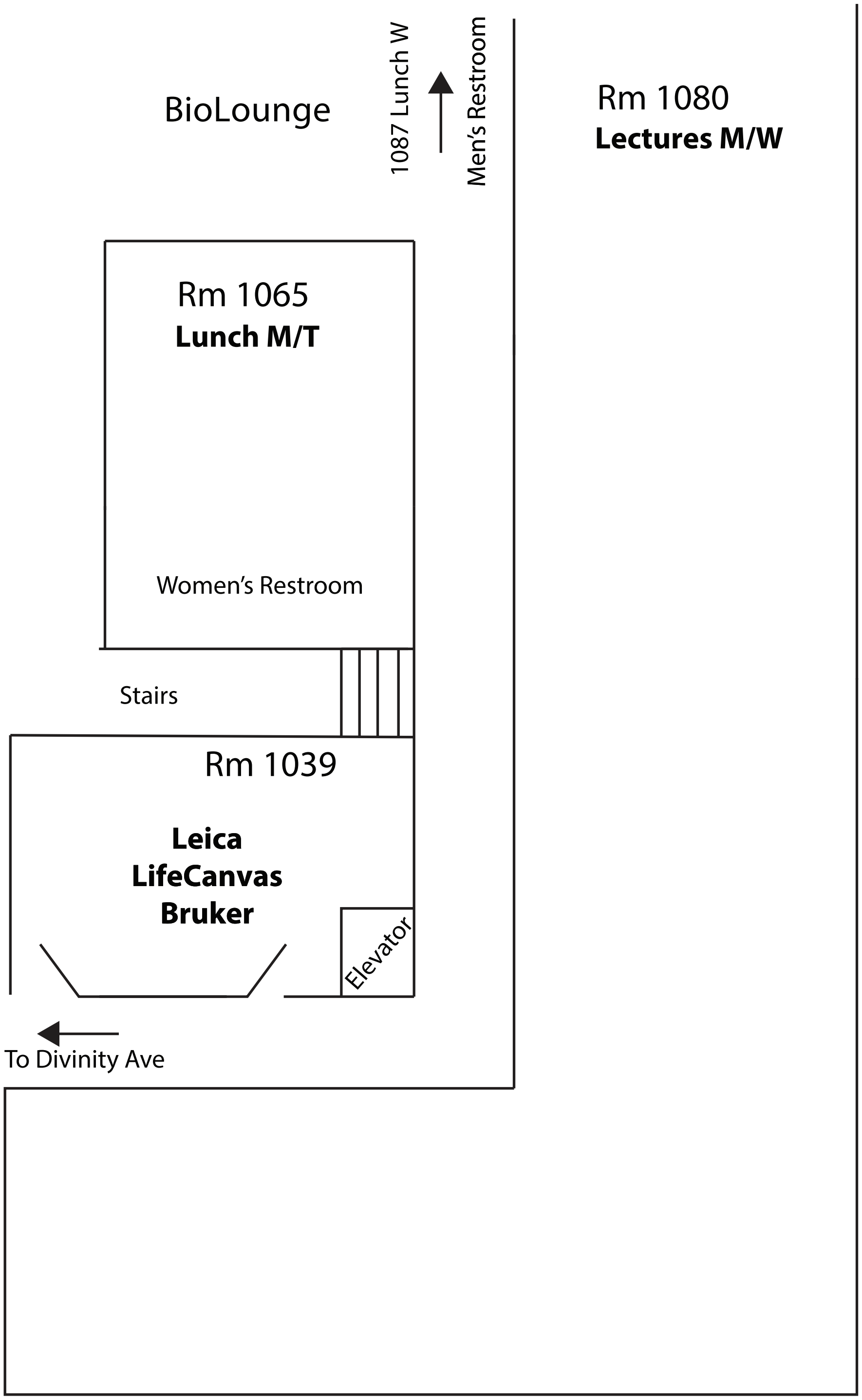
BioLounge
1087 Lunch W
Men's Restroom
Rm 1080
Lectures M/W
Rm 1065
Lunch M/T
Women's Restroom
Stairs
Rm 1039
Leica
LifeCanvas
Bruker
Elevator
To Divinity Ave

SECOND FLOOR

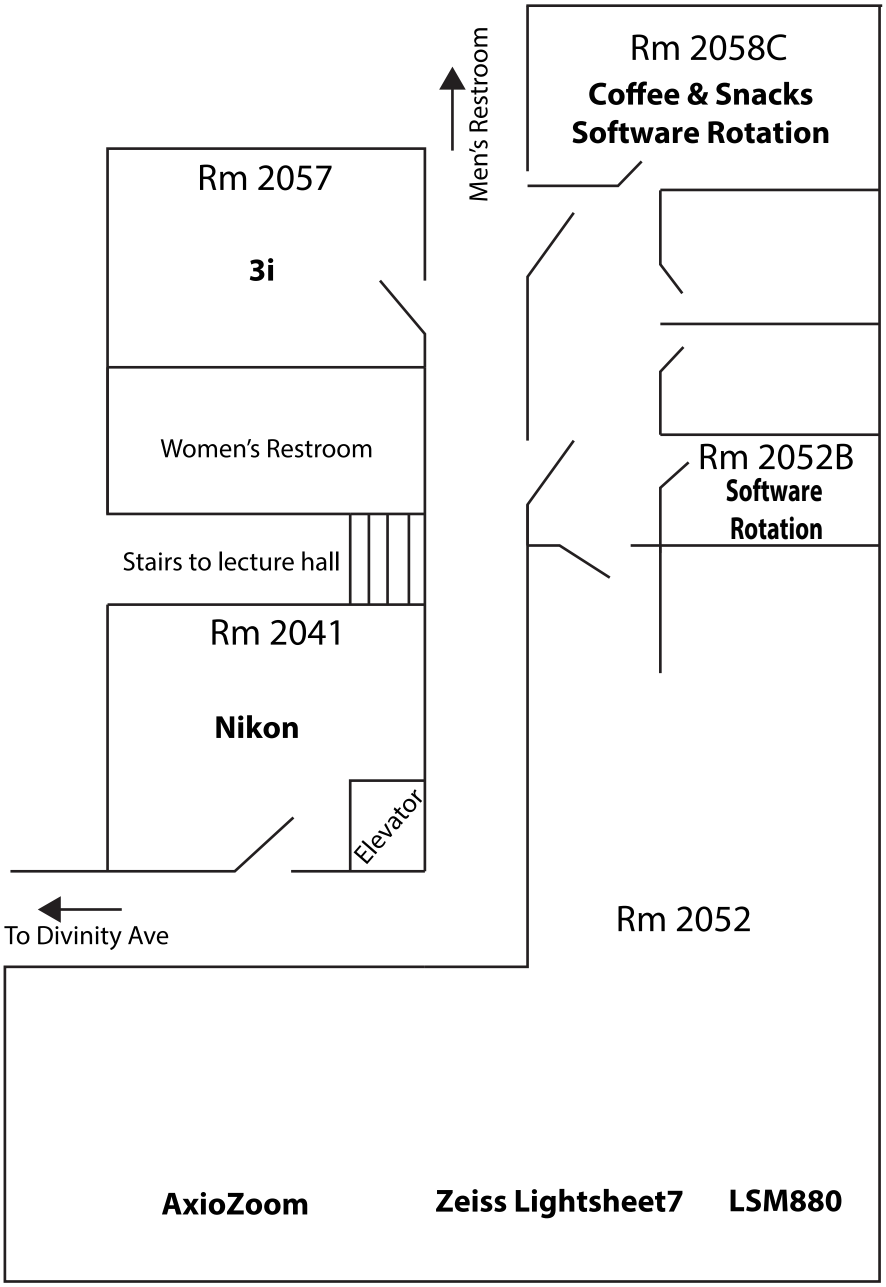

Tissue Clearing Protocols

Please note: Some substances used in these protocols are highly toxic. Please take care to read MSDS data sheets and follow the suggested handling guidelines. Also, ensure that all animal experimentation is approved by your local animal ethics panel.

Clearing modules

No published protocol exists that matches your tissue, label, and objective. Therefore, tissue clearing should be thought of as a series of modules, the correct selection of which will lead to a perfectly clear, labelled sample. Today we will practice the following common modules on a variety of different tissues:

1) **Decolorization/Bleaching**
2) **Decalcification**
3) **Delipidation**
4) **Refractive index matching**
5) **Expansion**

We are performing these techniques in a "quick" manner for the purpose of demonstrating them to you in a short amount of time. Therefore, you should not consider this to be a direct comparison of the modules/techniques or an indication of their best possible performance.

Please use caution and follow all outlined safety precautions, some of the chemicals used here are toxic/dangerous.

Here is a quick description of each method, refer to the references above for more comprehensive protocols.

Decolorization/Bleaching

1) You will be provided with 4 pieces of fixed, pigmented tissue:
    a. Groups 1-2: Octopus arm
    b. Groups 3-4: Axolotl arm
    c. Groups 5-6: Mouse kidney
    d. Groups 7-8: Zebrafish
2) Each sample will be placed in one of the following solutions:
    a. 20% v/v Quadrol/THEED (amino alcohol), 2% Triton X-100
    b. 10% H_2O_2 (v/v) in PBS (chromophore oxidizer)
    c. 10% H_2O_2 (v/v) in Methanol (chromophore oxidizer)
    d. 15 wt% 1-methylimidazole in PBS (N-alkyl imidazole), 2% Triton X-100

Decalcification

1) You will be provided with a mouse limb bone.
2) The sample will be transferred to 10% EDTA, 2% Triton X-100 in PBS.

Delipidation

1) You will be able to speak to Logos Biosystems and Life Canvas technologies about hydrogel embedding and lipid extraction via detergent. A representative from translucence can also speak to you about solvent-based solutions for delipidation.
2) You will be provided with a 1 mm thick mouse brain section that has been:
   a. Groups 1 –4: Dehydrated in methanol.
   b. Groups 5 - 8: Partially delipidated in 10% (w/v) CHAPS, followed by methanol dehydration.
3) Samples a and b will be placed in dichloromethane (DCM) to remove lipid (2x, 1 hour each).

Refractive Index Matching

1) You will be provided with a 1 mm thick mouse brain section that has been hydrogel embedded and delipidated in SDS. You will also use samples a or b from the delipidation module.
2) Groups 1 – 4: Place the hydrogel embedded samples in 80% Glycerol (RI = 1.43)
   Groups 5 – 8: Place the hydrogel embedded samples in Easy index (RI = 1.52)
3) Transfer your delipidation sample from DCM to Ethyl Cinnamate.

Expansion

1) You will be provided with a 200 µm thick brain section that has been embedded in an acrylate gel.
2) You will incubate the sample with Proteinase K at 37 C for 2 hours.
3) You will place the sample in pure H2O.

Schedule/Plan

1:30 – Lab safety discussion (Room 5096)

1:40 – A modular approach to tissue clearing (Doug Richardson) (Room 5096)

2:00 – Experiment #1 (Rooms 5088 and 5096)

2:30 – Rotation #1 (Rooms 5088 and 5096)

3:00 – Experiment #2 (Rooms 5088 and 5096)

3:30 – Rotation #2 (Rooms 5088 and 5096)

4:00 – Experiment #3 (Rooms 5088 and 5096)

4:30 – Rotation #3 (Rooms 5088 and 5096)

5:00 – Experiment #4 (Rooms 5088 and 5096)

5:30 – Rotation #4 (Rooms 5088 and 5096)

5:45 – Wrap-up/discussion/clean up (Room 5096)

2:00PM

Experiment #1 (Groups 1-4 in Room 5096; Groups 5-8 in Room 5088)

1) **Delipidation** – Transfer the Methanol dehydrated brain section (Groups 1-4) or the CHAPS+Methanol dehydrated sample (Groups 5 –8) to DCM (use fume hood!!).
2) **Expansion** - Place ExM sample in Proteinase K solution and transfer to 37C incubator.

Rotation #1

1) Groups 1, 2 – Logos Biosystem (Room 5088)
2) Groups 3, 4 – Life Canvas (Room 5096)
3) Groups 5, 6 – Translucence (Room 5088)
4) Group 7, 8 – Coffee Break (Room 2058C)

3:00PM

Experiment #2 (Groups 1-4 in Room 5096; Groups 5-8 in Room 5088)

1) **Delipidation –** Refresh the DCM on the methanol and CHAPS + methanol samples from Experiment #1 (use fume hood!).
2) **Decolorization/Bleaching** - Locate and obtain 4 pieces of the correct pigmented sample for your group:

   Groups 1-2: Octopus arm
   Groups 3-4: Axolotl arm
   Groups 5-6: Mouse kidney
   Groups 7-8: Zebrafish

   Place each piece of tissue in one of the following solutions:

   20% v/v Quadrol/THEED (amino alcohol), 2% Triton X-100
   10% H_2O_2 (v/v) in PBS (chromophore oxidizer)
   10% H_2O_2 (v/v) in Methanol (chromophore oxidizer)
   15 wt% 1-methylimidazole in PBS (N-alkyl imidazole), 2% Triton X-100

Rotation #2

1) Group 3, 4 – Logos Biosystem (Room 5088)
2) Groups 5, 6 – Life Canvas (Room 5096)

3) Groups 7, 8 – Translucence (Room 5088)
4) Groups 1, 2 – Coffee Break (Room 2058C)

4:00PM

Experiment #3 (Groups 1-4 in Room 5096; Groups 5-7 in Room 5088)

1) **Refractive Index Matching (Solvent)** - Transfer the brain slices in DCM to 5 mL Ethyl Cinnamate (use fume hood!!). Immediately mix the sample by slow inversions and continue to observe the sample for the next 5 minutes.
2) **Refractive Index Matching (Aqueous)** -Place one of the hydrogel embedded brain samples that are currently in PBS into 80% glycerol (Groups 1-4) or EasyIndex (Groups 5-8). Again, rotate and observe for 5 minutes.

Rotation #3

1) Group 5, 6 – Logos Biosystem (Room 5088)
2) Groups 7, 8 – Life Canvas (Room 5096)
3) Groups 1, 2 – Translucence (Room 5088)
4) Groups 3, 4 – Coffee Break (Room 2058C)

5:00PM

Experiment #4 (Groups 1-4 in Room 5096; Groups 5-7 in Room 5088)

1) **Expansion** - Retrieve the ExM sample from the incubator and transfer to a 6 cm petri dish. Add distilled water to the petri dish and observe.
2) **Decalcification** – Place the bone sample into EDTA solution.

Rotation #4

1) Group 7, 8 – Logos Biosystem (Room 5088)
2) Groups 1, 2 – Life Canvas (Room 5096)
3) Groups 3, 4 – Translucence (Room 5088)
4) Groups 5, 6 – Coffee Break (Room 2058C)

5:45 PM

1) Questions/discussion (Room 5096)
2) Clean up (Rooms 5088 and 5096)

Imaging Rotations

	Bruker	**Leica**	**LifeCanvas**	**Nikon**	**Zeiss Lightsheet**	**Zeiss LSM900/ AxioZoom**	**Software Show**	**3i**
ROOM	**1039**	**1039**	**1039**	**2041**	**2052**	**2052**	**2052/ 2058**	**2057**
Tuesday January 23rd								
1:00PM	Group 1	Group 2	Group 3	Group 4	Group 5	Group 6	Group 7	Group 8
2:00PM	Group 8	Group 1	Group 2	Group 3	Group 4	Group 5	Group 6	Group 7
3:15PM	Group 7	Group 8	Group 1	Group 2	Group 3	Group 4	Group 5	Group 6
4:15PM	Group 6	Group 7	Group 8	Group 1	Group 2	Group 3	Group 4	Group 5
Wednesday January 24th								
1:00PM	Group 5	Group 6	Group 7	Group 8	Group 1	Group 2	Group 3	Group 4
2:00PM	Group 4	Group 5	Group 6	Group 7	Group 8	Group 1	Group 2	Group 3
3:15PM	Group 3	Group 4	Group 5	Group 6	Group 7	Group 8	Group 1	Group 2
4:15PM	Group 2	Group 3	Group 4	Group 5	Group 6	Group 7	Group 8	Group 1

TCW 2024 Rotation #6
LSM 880 RI mismatch lab instructions

This tutorial will reinforce how spherical aberration induces axial distortion when imaging through a refractive index mismatched interface (as can often happen when imaging cleared tissue). If you look through the tissue clearing literature, you'll see many "pancaked" images where researchers forget to correct for SA. For more information, see Diel et al., Nature Protocols, 2020.

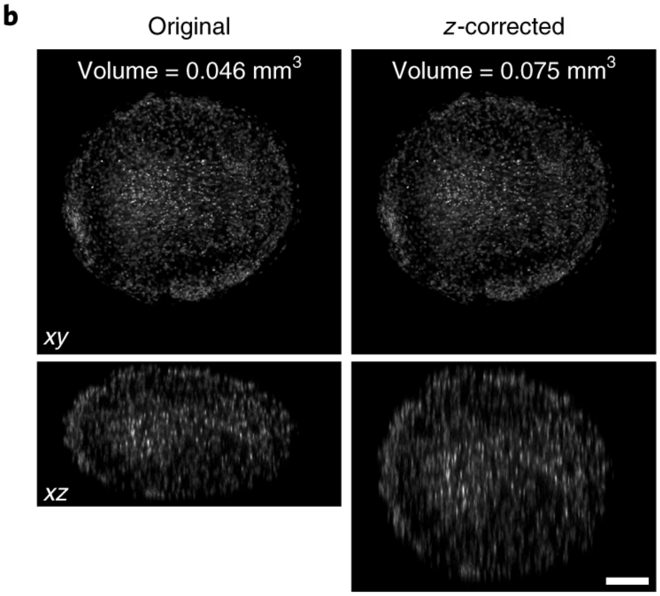

Let's get started!

1. You will be provided with a slide to which 2 um fluorescent beads have been absorbed to the surface. A coverslip has been placed ~ 100 um above the beads and a drop of immersion oil (RI = 1.518) has been placed between the beads and the coverslip. We will try to image a field of view that contains beads in air and oil (air RI = 1.000 and oil RI = 1.518). See red box in figure below.

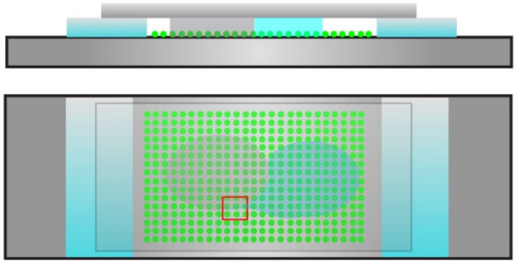

2. Make sure you are on the “LOCATE” tab and set up the Microscope Control Window as seen here:

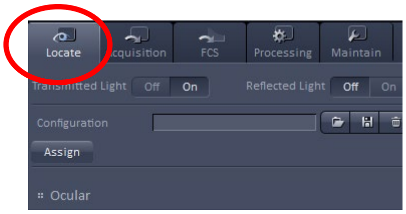

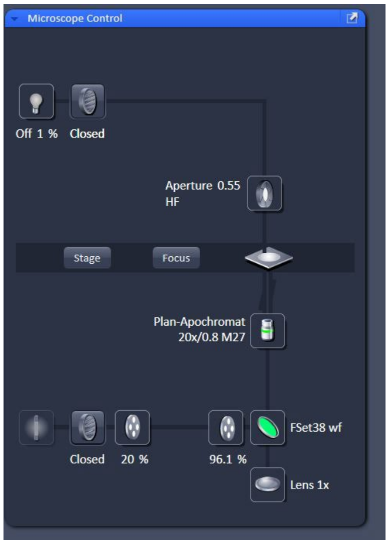

3. Focus on the sample and try to find an interface of air and the oil immersion fluid.
4. Turn on the fluorescence lamp to make sure there are green/yellow beads on the oil and air side of the interface.

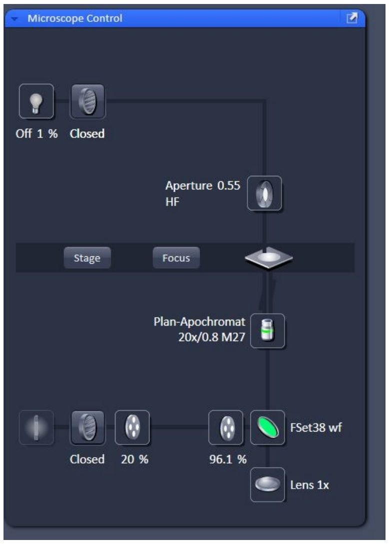

5. Close the shutter and move to the “ACQUISITION” tab.
6. Click on the “Smart Setup button”

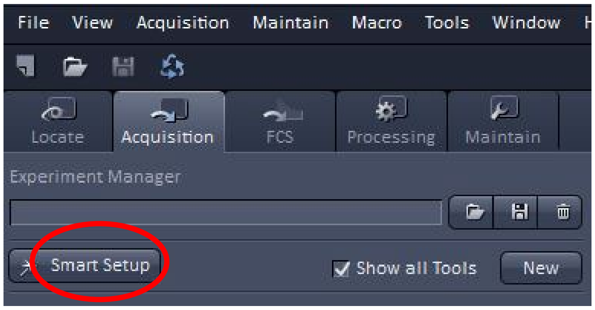

7. Click on the small black down arrow below and to the left of the word “Color” (arrow in Figure 3). A search box will appear. Type “488” and click on “Alexa Fluor 488” to add it to the experiment.

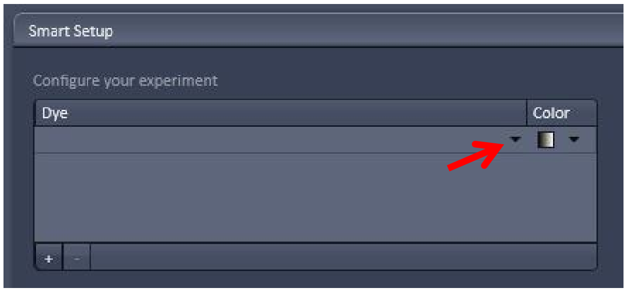

8. On the next window, choose Fastest and click “Apply.”
9. The imaging setup window should look something like the image below. Be sure to check the “T-PMT” box. Can you trace the light path from the laser to both detectors? What do the different components do? Hint: Hovering the mouse over the toptop or clicking on components may help.

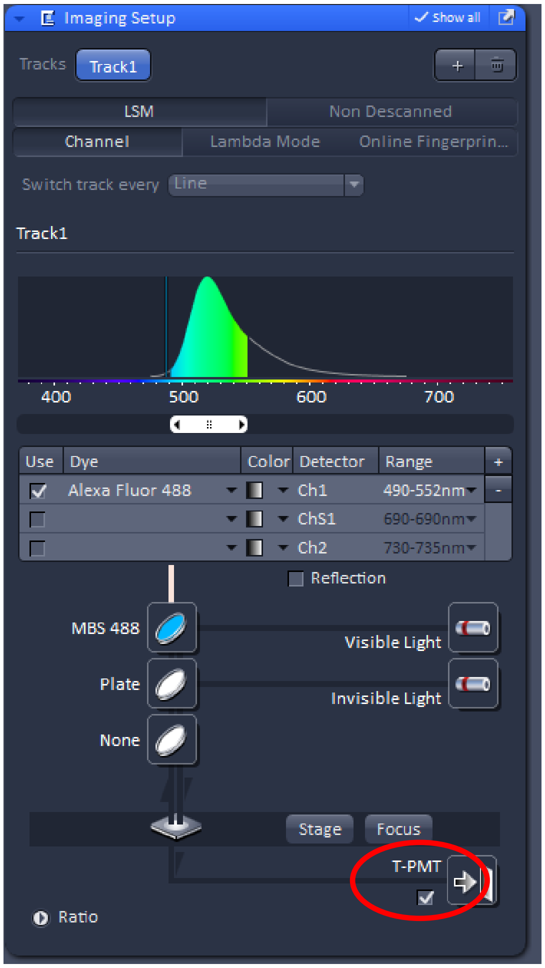

Switch track every Line

Use	Dye	Color	Detector	Range
☑	Alexa Fluor 488	◨	Ch1	490-552nm
☐		◨	ChS1	690-690nm
☐		◨	Ch2	730-735nm

☐ Reflection

T-PMT ☑

10. Next, we will setup the Acquisition mode window. Next to “Frame Size” click the “Optimal” button. The number of pixels you put into the image determines the resolution. This is likely a large number. Click on X*Y and select 1024 x1024. Why would we not want that many pixels? How have we affected the resolution of the microscope? Hint: You can see the effective pixel size in the “Scan Area” Region of this dialog window.

Acquisition Mode

Objective: Clr Plan-Neofluar 20x/1.0 Corr nd=1.45 M:

Scan Mode: Frame

Frame Size: X 1024, Y 1024

Line Step: 1

Speed: 7

Pixel Dwell 1.02 µsec, Scan Time 2.52 sec

Averaging

Number: 2

Bit Depth: 16 Bit

Mode: Line

Direction: <-->

Method: Mean

Corr X: 0.00

Corr Y: 0.00

☐ HDR

Scan Area

Image Size: 425.1 µm x 425.1 µm

Pixel Size: 0.42 µm

Zoom: 1.0

11. Change the “Speed” setting so that you have a dwell time of ~1 microsecond per pixel
12. Set the “Averaging” to 2. Why would we want to average the image?
13. Change the “Direction” setting to collect data in both directions (Bidirectional scan)
14. Finally, let’s setup the “Channels” window. These settings will be continually adjusted during the experiment.
15. First, check that the 488 laser is set to 1% (1.0 in the software).
16. Next, set the pinhole to 1 AU. What does AU stand for?
17. Ensure the gains are set low (usually <200 – some detectors will only go as low as 500, this is OK).

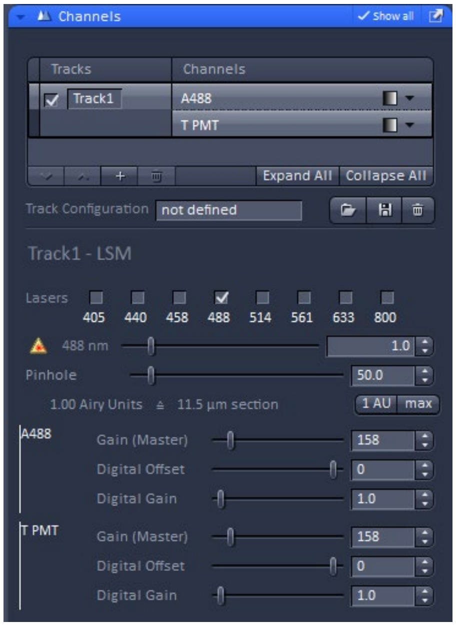

Channels

Tracks	Channels
☑ Track1	A488
	T PMT

Track Configuration: not defined

Track1 - LSM

Lasers: ☐ 405 ☐ 440 ☐ 458 ☑ 488 ☐ 514 ☐ 561 ☐ 633 ☐ 800

488 nm: 1.0

Pinhole: 50.0

1.00 Airy Units ≙ 11.5 µm section

A488

Gain (Master): 158

Digital Offset: 0

Digital Gain: 1.0

T PMT

Gain (Master): 158

Digital Offset: 0

Digital Gain: 1.0

18. We are now ready to image!
19. Click the “Live” button (below Smart Setup)

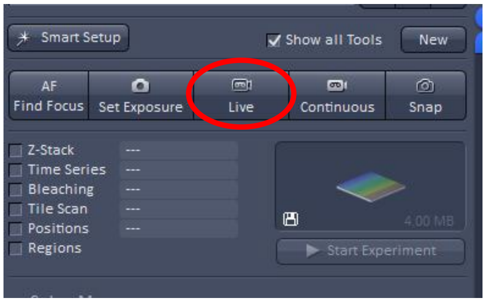

20. Click on the “Range Indicator” below the image window and slowly increase the “Master Gain” on the detectors until you see a DIM signal on the screen.
21. Adjust your focus (there is a focus knob under the monitor) until you see as many beads as possible in focus. Adjust your Master Gain so that there are only a few red (statured pixels) and that any areas outside the sample are blue (black or ‘0’ values pixels). (See image below)

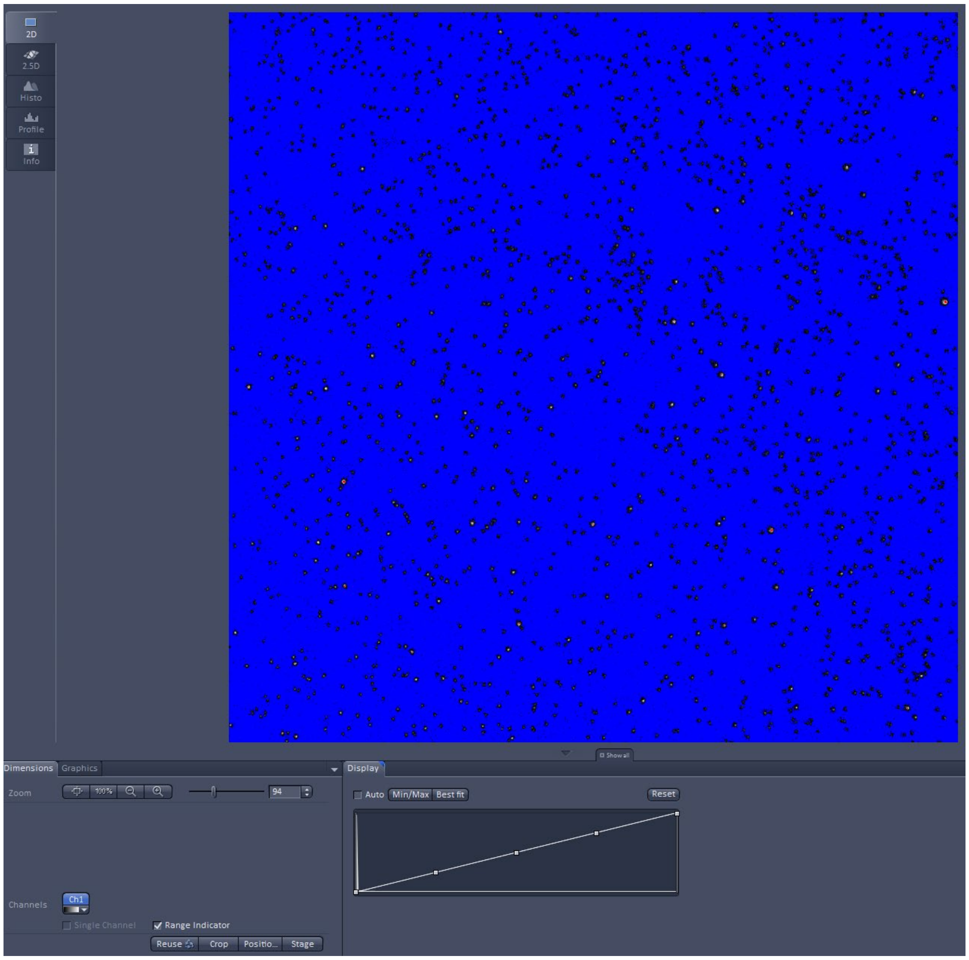

22. Press the stop sign that now appears over the live button to end the scan.
23. Press the “Snap” button. This will take a single image using the settings we selected in the “Acquisition Mode” window.
24. Next, let’s add a reflection track so that we can see the bottom of the coverslip and the top of the microscope slide
25. Turn on the Z-stack function

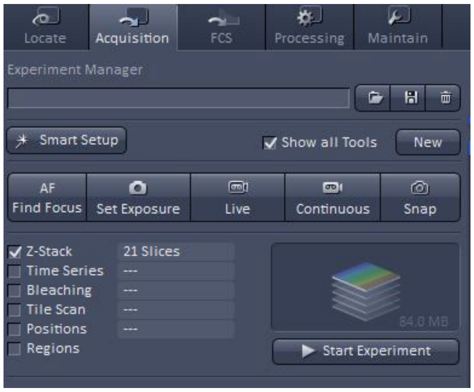

☑ Z-Stack 21 Slices
☐ Time Series ---
☐ Bleaching ---
☐ Tile Scan ---
☐ Positions ---
☐ Regions

26. Click the “+” button in the channels window and setup the Imaging setup and channels windows as shown below.

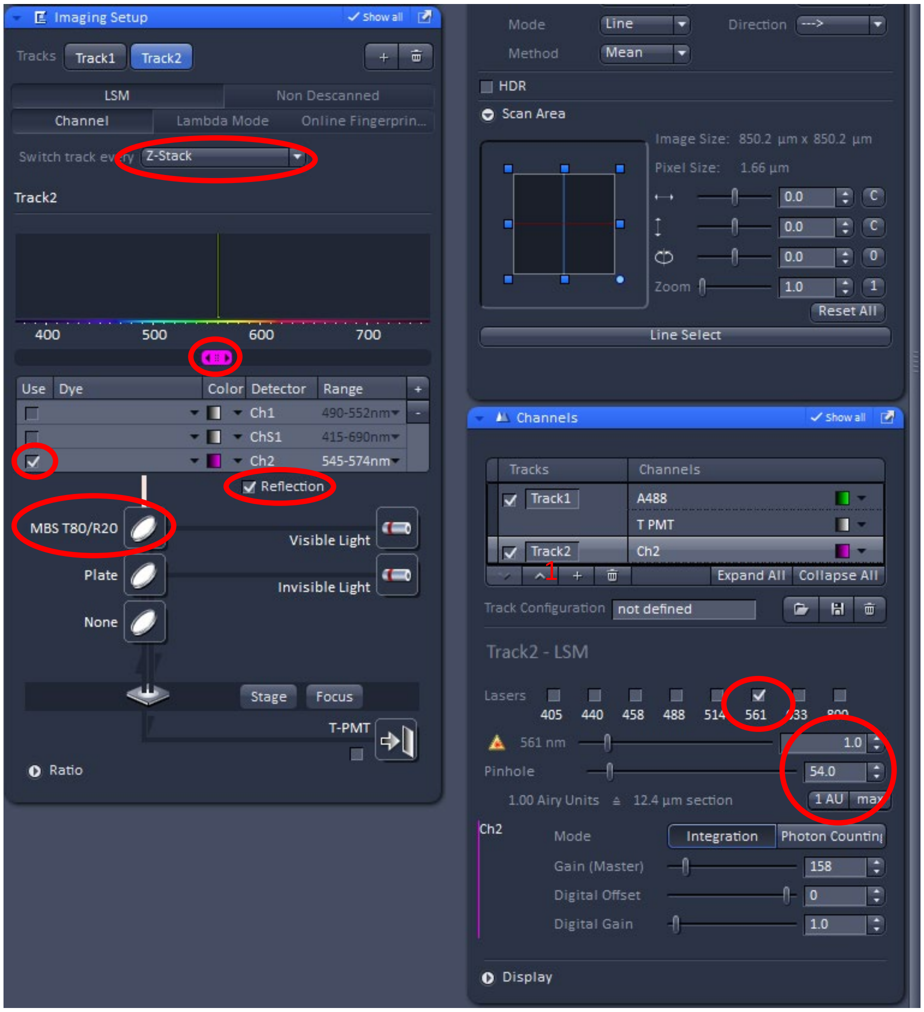

Switch track every Z-Stack

Use	Dye	Color	Detector	Range
☐			Ch1	490-552nm
☐			ChS1	415-690nm
☑			Ch2	545-574nm

☑ Reflection

MBS T80/R20

Mode Line
Direction --->
Method Mean
☐ HDR

Image Size: 850.2 µm x 850.2 µm
Pixel Size: 1.66 µm
0.0
0.0
0.0
Zoom 1.0

Tracks	Channels
☑ Track1	A488
	T PMT
☑ Track2	Ch2

Track Configuration not defined

Lasers ☐ 405 ☐ 440 ☐ 458 ☐ 488 ☐ 514 ☑ 561 ☐ 633 ☐ 800
561 nm 1.0
Pinhole 54.0
1.00 Airy Units ≙ 12.4 µm section 1 AU max

Ch2
Mode Integration Photon Countin
Gain (Master) 158
Digital Offset 0
Digital Gain 1.0

27. Remove the checkmark from Track one and click “live” focus up and down until you see a bright reflection from the coverslip or slide. You will only see this reflection on the air side of the air/oil interface (why?). Adjust you gain so that there is no saturation.
28. Next let’s set the Z-range.
29. The Z-stack window will have appeared below the channels window (click the blue bar to expand it)

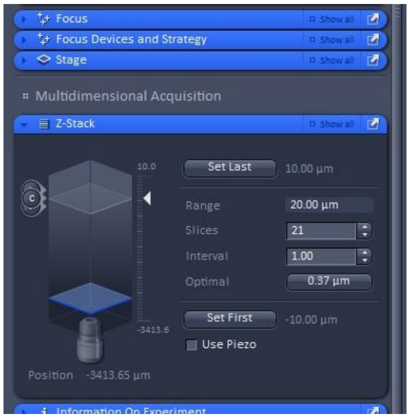

Set Last 10.00 µm

Range 20.00 µm

Slices 21

Interval 1.00

Optimal 0.37 µm

Set First -10.00 µm

☐ Use Piezo

Position -3413.65 µm

30. Turn on the live scan with track 2 (reflection) and focus to the coverslip or slide. In the Z-stack window, click “Set First”
31. Focus to the other side of the sample and click “Set Last.”
32. Stop the Live Scan.
33. Click the Optimal button. Is this really the optimal Z-slice? Should you make it larger or smaller?
34. Click on “Track 1”
35. Now click, “Start Experiment”
36. The microscope should image the stack twice. First it will image the transmitted light and fluorescent bead channels. Second, it will image the reflection channel.
37. When the experiment is complete, save the file and open the Orthogonal viewer (“Ortho” button the right of image window). Are the beads all on the same Z-plane?
38. Click the “3D” button to the left of the image to assist you in better determining this or perform a color-coded Z-projection (an instructor can aid you with this).
39. Determine the distance between the two planes that the beads appear to be on (estimate the number of Z-slices in between each plane and multiply by the step-size.
40. Does this match theory? Here is the original equation used to calculate the shift:

$$SA\ shift = (n_{\text{sample}}/n_{\text{immersion}})\text{objective movement}$$

41. This is an overestimate at high NA. A more accurate equation can be found in Diel et al., 2020.

Proceed to the AxioZoom, it is also part of this rotation!

Harvard Center for Biological Imaging
TCW 2020 AxioZoom Demo Instructions

The AxioZoom is an all-around multi-use microscope. Here we will use the darkfield function to assess quality of clearing. Darkfield is essentially a measure of light scatter. Should well cleared samples appear bright or dark (answer on next page)? **Be VERY careful when focusing, it is possible to crash the objectives into the stage!!** If you are unsure of anything, or have questions along the way, please ask an instructor.

Let's get started!

1. First, place an uncleared brain sample (from yesterday's hands-on session) under the microscope (1.0x objective).
2. If no one in your group is familiar with the AxioZoom, ask an instructor to quickly show you the controls for focusing, zooming, and moving the stage.
3. Click on the "Acquisition" tab

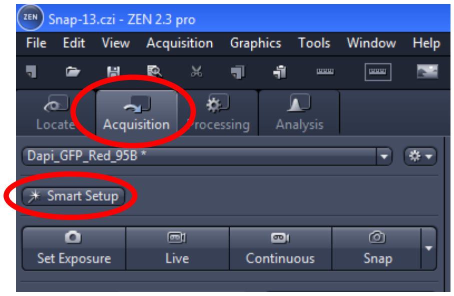

4. Click on "Smart Setup"
5. Add a track by clicking the "+" button. In the popup window, under contrasting methods, select "TL Darkfield."

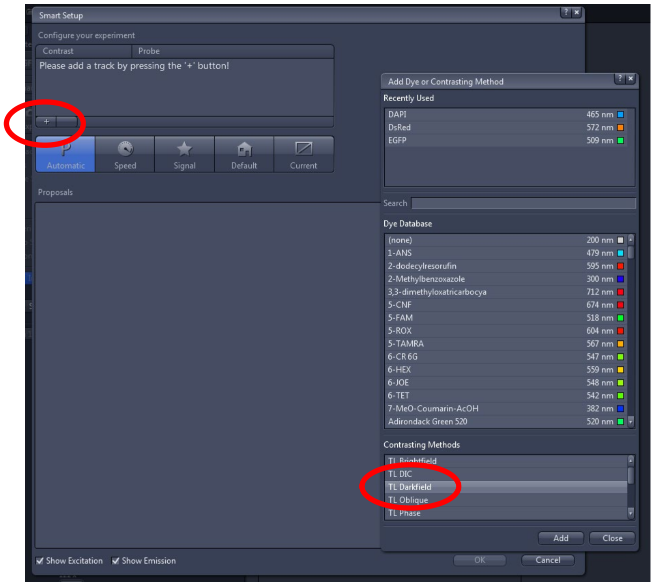

Please add a track by pressing the '+' button!

Recently Used

DAPI	465 nm	🟦
DsRed	572 nm	🟧
EGFP	509 nm	🟩

Dye Database

(none)	200 nm	⬜
1-ANS	479 nm	🟦
2-dodecylresorufin	595 nm	🟥
2-Methylbenzoxazole	300 nm	🟦
3,3-dimethyloxatricarbocya	712 nm	🟥
5-CNF	674 nm	🟥
5-FAM	518 nm	🟩
5-ROX	604 nm	🟥
5-TAMRA	567 nm	🟧
6-CR 6G	547 nm	🟩
6-HEX	559 nm	🟨
6-JOE	548 nm	🟩
6-TET	542 nm	🟩
7-MeO-Coumarin-AcOH	382 nm	🟦
Adirondack Green 520	520 nm	🟩

Contrasting Methods

- TL Brightfield
- TL DIC
- TL Darkfield
- TL Oblique
- TL Phase

6. Close the “Add Dye or Contrasting Method“ window and click OK in the Smart Setup window.

Darkfield allows for the quantitation of bent (scattered) light. Light rays are directed out of the lamp in the base so that they will miss the objective. This gives a black (dark) background. If the light passes through something that causes it to bend, it will be able to enter the objective and appear as a bright spot on the camera. Therefore, the dimmer an object is in darkfield, the better it was cleared.

7. Check that the Axiocam_512_color camera is selected in the “Channels” window. Set the exposure time to 75 ms.

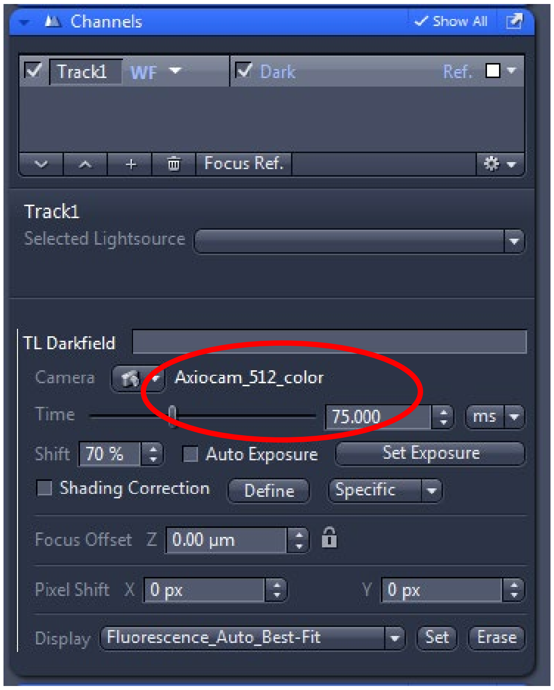

☑ Track1 WF ☑ Dark

Track1

Selected Lightsource

TL Darkfield

Camera Axiocam_512_color

Time 75.000 ms

Shift 70 % ☐ Auto Exposure

☐ Shading Correction

Focus Offset Z 0.00 µm

Pixel Shift X 0 px Y 0 px

Display Fluorescence_Auto_Best-Fit

8. Set the Transmitted light base to 85% brightness (Click on the blue square called “Darkfield” in the Imaging Setup window.

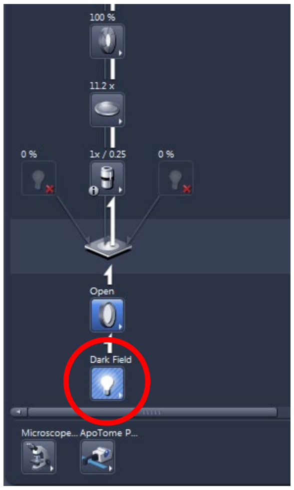

9. Check that the manual camera changer is pushed all the way in (ask an instructor)
10. Click “Live” and focus on the tissue.
11. Click “Snap” to take a picture. A thumbnail image will appear on the right. Click on the disk underneath to save the image. Save it in D:\Users\TCW2020\Group#
12. Now move to the iDISCO sample and repeat the measurement. What do you notice?
13. Try the CLARITY and CUBIC samples as well.

Module based clearing protocols for imaging demos

Octopus Arm:

Fixation

1. Submerged in 3% (w/v) paraformaldehyde in PBS overnight at 4C
2. Washed 3x for 1 hour each with PBS

Pretreatments

1. **Decolorization 1** – Incubated overnight in 10% (v/v) Quadrol in PBS

   - Washed 3x for 1 hour each in PBS

2. **Decolorization 2** – Incubated overnight in 10% H_2O_2 in PBS

   - Washed 3x for 1 hour each in PBS

3. **Dehydration 1** – Dehydrated through a methanol gradient (20%, 40%, 60%, 80%, 100% in PBS; 30-60 mins each step)
4. **Rehydration 1** – Reverse step 3

Labeling

1. **Primary antibody** – Incubated sample for 3 days in primary antibody solution:
   i. 0.2% (v/v) Triton X-100
   ii. 5% (v/v) DMSO
   iii. 2 µg/mL Primary antibody (Monoclonal Anti-Tubulin, MilliporeSigma T6793)
   iv. In PBS
   - Washed 3x in large volume of PBS (30 mL). Changed solution 3x over 24 hours
2. **Secondary antibody** – Incubated sample for 3 days in primary antibody solution (in PBS):
   i. 0.2% (v/v) Triton X-100
   ii. 5% (v/v) DMSO
   iii. 2 µg/mL Secondary antibody (Anti-Mouse IgG (H+L) CF568, MilliporeSigma SAB4600309)
   - Washed 3x in large volume of PBS (30 mL). Changed solution 3x over 24 hours
3. **Post-fix** – Fixed sample in 3% PFA in PBS for 3 hours
   - Washed 3x for 1 hour each with PBS

Delipidation

1. **Dehydration 2** – Dehydrated through a methanol gradient (20%, 40%, 60%, 80%, 100% in PBS; 30-60 mins each step)
2. **Delipidation 1** – Delipidated sample in 100% DCM for 1 hour
3. **Delipidation 2** – Delipidated sample in 100% DCM until sample sunk to bottom

Refractive Index Matching

1. Placed sample in 100% Ethyl Cinnamate and incubated for a minimum of 12 hours before imaging

7-day old mouse pup brain (subset of neurons GFP and mScarlett +ve):

Fixation

1. Mouse was transcardially perfused with 20 mL PBS
2. Mouse was transcardially perfused with 10 mL 3% PFA in PBS
3. Brain was removed and submerged in 3% (w/v) paraformaldehyde in PBS overnight at 4C
4. Brain was washed 3x for 1 hour each with PBS

Pretreatments

1. **Decolorization 1** – Incubated overnight in 5% (v/v) Quadrol in PBS

   - Washed 3x for 1 hour each in PBS

2. **Hydrogel Embedding 1** – Incubated overnight in hydrogel solution at 4C
   i. 3% Paraformaldehyde
   ii. 3% (w/v) Acrylamide
   iii. 0.02% (w/v) Bisacrylamide
   iv. 2.5 mg/mL VA044 Thermal Polymerization Initiator

   Made in PBS

3. **Hydrogel Embedding 2** – Polymerized gel under vacuum @ 37C for 3 hours
   - Removed excess gel by rolling tissue on paper towel
   - Washed overnight in large volume of PBS (30 mL)

Delipidation

1. **Delipidation 1** - Passively delipidated sample in Logos ETC Solution for 24 hours
   i. 4% SDS
   ii. 2% Boric Acid
   iii. pH 8.5 (adjusted with NaOH)
2. **Delipidation 2** – Delipidated sample in Logos ETC Buffer using X-CLARITY ETC chamber at 0.8 A for 12 hours
3. **Delipidation 3** – Passively delipidated sample in Logos ETC Solution for 12 hours
   - Washed overnight in large volume of PBS (30 mL) **AT ROOM TEMP**

Refractive Index Matching

1. **RI Matching 1** - Placed sample in 5 mL of Easy Index RI = 1.52 solution from LifeCanvas overnight
2. **RI Matching 2** – Placed sample in fresh 30 mL of Easy Index RI = 1.52 solution overnight

Adult mouse brain (vasculature labelling):

Labelling

1. DiI dye solution was prepared immediately prior to perfusion:
    a. 1 mg DiI (CellTracker™ CM-DiI Dye, Product #C7001 ThermoFisher) was dissolved in 1 mL pure ethanol
    b. 200 uL of DiI/Ethanol solution was diluted in 10 mL of PBS supplemented with 5% (w/v) glucose
2. Mouse was transcardially perfused with 20 mL PBS
3. Mouse was transcardially perfused with 10 mL DiI dye solution

Fixation

1. Mouse was transcardially perfused with 10 mL 3% (w/v) PFA in PBS
2. Brain was removed and submerged in 3% PFA in PBS overnight at 4C
3. Brain was washed 3x for 1 hour each with PBS

Pretreatments

1. **Dehydration** – Brain was dehydrated through a methanol gradient (20%, 40%, 60%, 80%, 100% in PBS; 30-60 mins each step)

Delipidation

1. **Delipidation 1** – Delipidated sample in 100% DCM for 1 hour
2. **Delipidation 2** – Delipidated sample in 100% DCM until sample sunk to bottom

Refractive Index Matching

3. **RI Matching 1** - Placed sample in 30 mL of Ethyl Cinnamate

Adult axolotl (GFP neuron labeling):

Fixation

1. Axolotl was fixed with 3% PFA in PBS overnight
2. Washed 3x for 1 hour each with PBS

Pretreatments

1. **Decalcification** – Axolotl was decalcified in 15% 1-methylimidizole and 10% EDTA for minimum 4 days
    - Washed overnight in large volume of PBS (30 mL)

2. **Decolorization** – Axolotl was decolorized overnight in 20% Quadrol in PBS.
3. **Dehydration** – Axolotl was dehydrated through a tert-butanol gradient (20%, 40%, 60%, 80%, 100% in PBS; 30-60 mins each step)

Delipidation

3. **Delipidation 1** – Delipidated sample in 100% DCM for 1 hour
4. **Delipidation 2** – Delipidated sample in 100% DCM until sample sunk to bottom

Refractive Index Matching

4. **RI Matching 1** - Placed sample in 30 mL of 75% Ethyl Cinnamate + 25% PEG

Axolotl arms and tails:

Fixation

1. Axolotl was fixed with 3% PFA in PBS overnight
2. Washed 3x for 1 hour each with PBS

Pretreatments

1. **Decolorization 1** – Incubated overnight in 10% H2O2 in PBS

   - Washed 3x for 1 hour each in PBS

2. **Hydrogel Embedding 1** – Incubated overnight in hydrogel solution at 4C
   i. 3% Paraformaldehyde
   ii. 3% (w/v) Acrylamide
   iii. 0.02% (w/v) Bisacrylamide
   iv. 2.5 mg/mL VA044 Thermal Polymerization Initiator

   Made in PBS

3. **Hydrogel Embedding 2** – Polymerized gel under vacuum @ 37C for 3 hours
   - Removed excess gel by rolling tissue on paper towel
   - Washed overnight in large volume of PBS (30 mL)

Delipidation

1. **Delipidation 1 – Delipidated sample in Logos ETC Buffer using X-CLARITY ETC chamber at 0.8 A for 24 hours**
   - Washed overnight in large volume of PBS (30 mL) **AT ROOM TEMP**

Labeling

1. **Primary antibody** – Incubated sample for 3 days in primary antibody solution:
   i. 0.2% (v/v) Triton X-100
   ii. 5% (v/v) DMSO
   iii. 2 µg/mL Primary antibody (Monoclonal Anti-Tubulin, MilliporeSigma T6793)
   iv. In PBS

- Washed 3x in large volume of PBS (30 mL). Changed solution 3x over 24 hours

2. **Secondary antibody** – Incubated sample for 3 days in primary antibody solution (in PBS):
    1. 0.2% (v/v) Triton X-100
    2. 5% (v/v) DMSO
    3. 2 µg/mL Secondary antibody (Anti-Mouse IgG (H+L) CF568, MilliporeSigma SAB4600309)
    - Washed 3x in large volume of PBS (30 mL). Changed solution 3x over 24 hours

3. **Post-fix** – Fixed sample in 3% PFA in PBS for 3 hours
    - Washed 3x for 1 hour each with PBS

Refractive Index Matching

1. **RI Matching 1** - Placed sample in 5 mL of Easy Index RI = 1.52 solution from LifeCanvas overnight
2. **RI Matching 2** – Placed sample in fresh 30 mL of Easy Index RI = 1.52 solution overnight

Check for updates

Tissue clearing

Douglas S. Richardson[1,2]✉, *Webster Guan*[3], *Katsuhiko Matsumoto*[4,5], *Chenchen Pan*[6,7], *Kwanghun Chung*[4,9,10,11,12,13,14], *Ali Ertürk*[6,7,8], *Hiroki R. Ueda*[4,5] *and Jeff W. Lichtman*[1,2,15]

Abstract | Tissue clearing of gross anatomical samples was first described more than a century ago and has only recently found widespread use in the field of microscopy. This renaissance has been driven by the application of modern knowledge of optical physics and chemical engineering to the development of robust and reproducible clearing techniques, the arrival of new microscopes that can image large samples at cellular resolution and computing infrastructure able to store and analyse large volumes of data. Many biological relationships between structure and function require investigation in three dimensions, and tissue clearing therefore has the potential to enable broad discoveries in the biological sciences. Unfortunately, the current literature is complex and could confuse researchers looking to begin a clearing project. The goal of this Primer is to outline a modular approach to tissue clearing that allows a novice researcher to develop a customized clearing pipeline tailored to their tissue of interest. Furthermore, the Primer outlines the required imaging and computational infrastructure needed to perform tissue clearing at scale, gives an overview of current applications, discusses limitations and provides an outlook on future advances in the field.

Tissue clearing refers to a collection of techniques that render biological samples transparent. These techniques enable the deep imaging of large volumes of tissues using light microscopy approaches that are usually limited by the scattering of light by the tissue. Tissue clearing allows researchers to avoid time-consuming tissue sectioning approaches that can introduce artefacts and to examine biological tissues in their native, 3D state. Furthermore, light microscopy enables the use of individual-molecule labelling techniques and imaging at submicrometre spatial resolutions, unlike traditional approaches for volume imaging such as MRI, computed tomography (CT) and ultrasound imaging.

Tissue clearing protocols facilitate the passage of light through a biological sample by minimizing the refractive index (RI) differences between components of the tissue[1]. In general, this requires the removal of lipids (RI 1.47) and replacement of intracellular and extracellular fluids (RI 1.35) with a solution of equivalent RI to the remaining protein constituents (RI >1.50). Despite this simple underlying principle, the design of a tissue clearing project can easily become complex and requires optimization of multiple variables. Factors that should be considered include the need for retention of molecules of interest during processing (for example, proteins or mRNA), maintenance of the structural integrity of the sample, conformational protection of endogenously expressed fluorescent proteins, enhanced porosity to allow for the diffusion of small-molecule or immunoglobulin labels, and preservation of the structure of relevant epitopes if immunolabelling.

Previous reviews have highlighted the basic physics[1] and chemistry[2] behind tissue clearing and highlighted the promise of tissue clearing for the field of neuroscience[3]. This Primer instead focuses on the methodology for clearing various tissue types, the technologies for imaging cleared tissue and how to store and analyse image data. Specifically, the Primer enables a researcher to understand the purpose of each step in a clearing protocol and assemble a clearing pipeline specifically designed for their sample. It discusses the advantages and disadvantages of several imaging techniques and describes several common image analysis and quantification routines. This comprehensive description of clearing, imaging and data analysis aims to provide the necessary information for individual researchers to design simple clearing experiments and also to guide institutional core facilities and commercial entities on how to clear samples at scale.

Experimentation

Historically, clearing techniques were assigned to one of two categories on the basis of the composition of their final clearing solution: solvent-based (hydrophobic) or aqueous-based (hydrophilic). Originally, solvent-based techniques were faster, provided a closer RI match to the delipidated, proteinaceous sample and shrunk the sample in size. Conversely, aqueous techniques better preserved the emission of fluorescent proteins (if present), retained biomolecules to a higher degree and expanded

✉e-mail: drichardson@fas.harvard.edu

https://doi.org/10.1038/s43586-021-00080-9

Author addresses

[1]Harvard Center for Biological Imaging, Harvard University, Cambridge, MA, USA.
[2]Department of Molecular and Cellular Biology, Harvard University, Cambridge, MA, USA.
[3]Department of Chemical Engineering, MIT, Cambridge, MA, USA.
[4]Department of Systems Pharmacology, Graduate School of Medicine, The University of Tokyo, Tokyo, Japan.
[5]Laboratory for Synthetic Biology, RIKEN Center for Biosystems Dynamics Research, Osaka, Japan.
[6]Institute for Tissue Engineering and Regenerative Medicine (iTERM), Helmholtz Zentrum München, Munich, Germany.
[7] Institute for Stroke and Dementia Research, Klinikum der Universität München, Ludwig Maximilians University of Munich, Munich, Germany.
[8]Munich Cluster for Systems Neurology (SyNergy), Munich, Germany.
[9]Picower Institute for Learning and Memory, MIT, Cambridge, MA, USA.
[10]Institute for Medical Engineering and Science, Massachusetts Institute of Technology, Cambridge, MA, USA.
[11]Department of Brain and Cognitive Sciences, MIT, Cambridge, MA, USA.
[12]Broad Institute of Harvard University and MIT, Cambridge, MA, USA.
[13]Center for Nanomedicine, Institute for Basic Science (IBS), Seoul, Republic of Korea.
[14]Nano Biomedical Engineering (Nano BME) Graduate Program, Yonsei-IBS Institute, Yonsei University, Seoul, Republic of Korea.
[15]Center for Brain Science, Harvard University, Cambridge, MA, USA.

samples in size. However, many of the original limitations of each category have been addressed, and solvent and aqueous techniques have become nearly equivalent[4–6]. In fact, it is now recognized that combining aqueous-based and solvent-based delipidation steps can be advantageous, and aqueous RI-matching solutions can be combined with solvent-based delipidation (and vice versa). Therefore, it no longer seems relevant to label techniques as aqueous-based or solvent-based but instead to view tissue clearing as a pipeline composed of several modules that can be mixed and matched. These modules are sample fixation, pre-treatment, delipidation, fluorescent labelling, RI matching and image acquisition and analysis (FIG. 1). Each clearing protocol must be customized to the sample type and the labelling method used, and the imaging modalities (such as microscopes) or IT infrastructure available to a researcher can influence the choice of clearing technique and inform the scale of the project. Below is an in-depth discussion of the various modules that can be combined to create a complete tissue clearing workflow, with details summarized in TABLE 1.

Sample choice

Many commonly studied biological tissues from a host of organisms have been shown to be compatible with tissue clearing approaches. Entire rodents have been cleared and imaged while intact[7–11], as have several other model organisms including *Drosophila*[12,13] and zebrafish[14,15]. Human tissues, including an entire human brain and kidney, have also been cleared successfully[6]. However, there are limitations to clearing and not all tissues clear equally well. For example, successful clearing of whole rodents usually requires the removal of the skin from the animal. Additionally, tissues with pigments (such as skin), calcification (bone) or extensive extracellular matrix and/or structural proteins (tumours and cardiac tissues) do not obtain the same level of clearing as tissues without these features.

Specific and bright fluorescent labelling is essential for imaging, regardless of the tissue. Small-molecule organic dyes, dye-conjugated antibodies and genetically encoded fluorescent proteins are commonly used labels. Small-molecule dyes can rapidly penetrate and label thick tissue, but are limited in their recognizable targets. Antibodies have the widest utility but have long labelling times and reproducibility issues owing to batch-to-batch variation. Genetically encoded fluorescent proteins may label a higher percentage of target molecules and allow labelling of specific cell types[16]. Viral expression of fluorescent proteins avoids the complex molecular biology of stably introducing a transgene to a tissue and can achieve high levels of fluorescence emission depending on virus titre, serotype and choice of promoter[17,18]. However, care must be taken as many fluorophores are susceptible to bleaching with hydrogen peroxide, and fluorescent protein emission can be quenched by dehydration (see below).

Finally, it is important to match the final size of the sample to available imaging systems and data storage capacity. It is of note that cleared samples that are millimetres or centimetres in size can exceed the working distance of many microscope objectives and can produce terabytes of data.

Fixation

Fixation of tissue is always required before clearing to avoid excessive loss of target biomolecules or tissue integrity. Fixing covalently crosslinks proteins and/or nucleic acids in the tissue to preserve the mechanical integrity and biomolecular architecture of the tissue. Fixation is a balancing act; if fixation is too weak, the tissue will not withstand chemical treatments in later clearing steps. Conversely, over-fixation can result in fixative molecules blocking access to the epitopes required for fluorescent labelling.

The degree of fixation is determined by the concentration of the fixative and the amount of time the tissue spends immersed in it. The most commonly used tissue fixative is paraformaldehyde (PFA), which crosslinks the tissue's biomolecules by reacting with amine groups on proteins and nucleic acids. PFA is usually used at a concentration of 3–4% w/v in phosphate-buffered saline (PBS). PFA diffuses rapidly into tissue, making it a good molecule for quickly and uniformly fixing samples >500 μm in diameter. Glutaraldehyde (GA) can be used as an alternative to PFA; although it is chemically similar, it reacts with biomolecular amine groups more quickly, resulting in more intermolecular covalent crosslinking and enhanced tissue fixation[19]. However, as GA is a larger molecule than PFA, diffusion into tissues is slower, leading to non-uniform tissue preservation. To address issues caused by diffusion, the SWITCH method can be used[20]. In this method, inactivated GA molecules diffuse through the sample in a low-pH 'OFF' buffer, and once the GA molecules are uniformly distributed, the tissue is transferred to a neutral pH 'ON' buffer to initiate fixation. Using this protocol, GA was demonstrated to provide improvements in biomolecular preservation (3–5% protein loss) over PFA tissues (30–40% protein loss)[20].

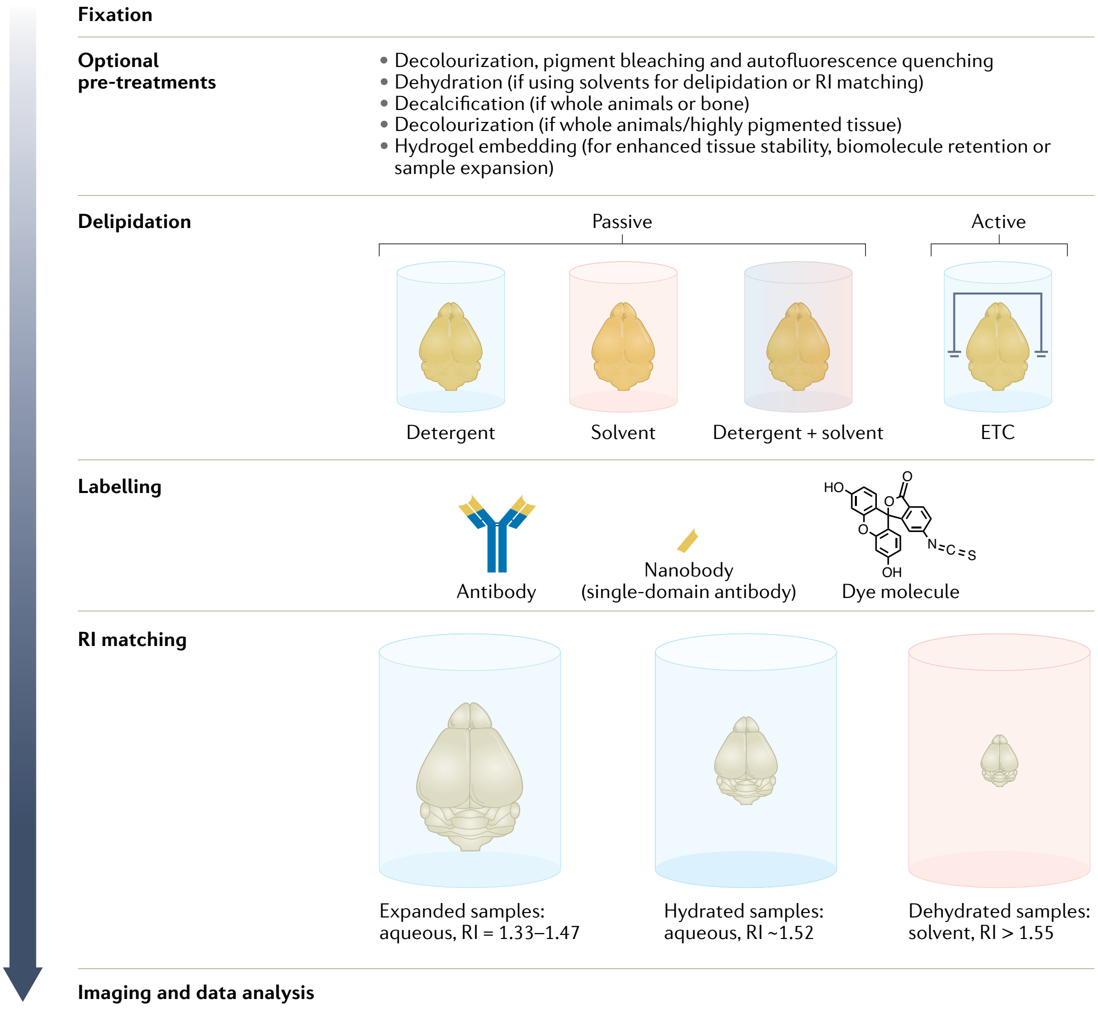

Fig. 1 | **An overview of the components of a tissue clearing experiment.** Tissue clearing workflows are numerous, making them difficult to summarize. However, workflows can be defined as a series of modules (fixation, pre-treatment, delipidation, labelling and refractive index (RI) matching), in which each module can be customized to suit the tissue that is to be cleared. Multiple modules must be combined to clear large organoids, organs and whole animals, whereas small samples (<0.5 mm) may only require a RI-matching step. Blue shading indicates that samples are immersed in polar, water-based, aqueous solutions whereas red shading indicates samples are in less polar or non-polar solvent. Expanded samples are hyperhydrated and grow in size, whereas dehydrated samples commonly shrink. ETC, electrophoretic tissue clearing.

GA-preserved tissues exhibit high autofluorescence in the 500–600 nm range[21] and retain mRNA molecules less well than PFA, and therefore GA is most suitable for strengthening delicate tissues or retaining poorly expressed proteins if imaging proteins in downstream imaging pipelines.

Chemical crosslinks formed by aldehyde fixatives can block antibody access to epitopes and reduce the effectiveness of downstream immunostaining (see below). Enzymatic digestion and/or high heat and pressure treatment is routinely used to permeabilize tissue, reduce aldehyde crosslinks and restore antibody accessibility in thin histology sections — a process referred to as antigen retrieval. However, applying these treatments to intact tissue is detrimental to its integrity. Interestingly, a combination of detergent, solvent and mild heat has been shown to have an antigen retrieval effect when included in a tissue clearing protocol (FLASH, see REF.[12]).

Using polyepoxide molecules as fixatives, such as polyglycerol-3-polyglycidyl ether (P3PE), enables a high degree of intermolecular and intramolecular crosslinking for several biomolecules. Use of P3PE in the SHIELD protocol produces tissue that is more rigid and mechanically stable than tissue fixed with PFA or GA[4]. Additionally, this fixation method produces cleared tissue with significantly higher protein retention, mRNA retention and fluorescent protein emission than GA-fixed or PFA-fixed tissue. P3PE concentrations can be adjusted between 2% and 20% w/v, with epitope availability, chemical penetrability and label penetrability enhanced at low concentrations and protein preservation, mRNA preservation and tissue rigidity enhanced at high concentrations. In addition to the above fixation methods, 1-ethyl-3-(3-dimethylaminopropyl) carbodiimide (EDC) hydrochloride has shown utility for fixing genetic material in place[4].

It is best to evaluate several fixation protocols, including various concentrations and durations of each fixative,

Autofluorescence
Fluorescence that arises from endogenous fluorescent molecules contained within a biological specimen. Can also be introduced exogenously (that is, some hydrogels autofluoresce).

Table 1 | **Tissue clearing modules**

Modules and reagents	Indications for use	Required equipment	Additional considerations	Originating protocol
Fixation (1–12 h)				
Paraformaldehyde (PFA)	General fixation protocol	None	Concentration and timing require optimization	Scale[173], CLARITY[33]
Glutaraldehyde (GA)	Used to retain low-abundance biomolecules Used to stabilize fragile tissues	None	Concentration and timing require optimization Often combined with PFA	SWITCH[20]
Polyglycerol-3-polyglycidyl ether (P3PE)	Used to retain low-abundance biomolecules Used to stabilize fragile tissues Used to preserve fluorescent protein emission Used to retain mRNA	None	High protein and mRNA fixation efficiency	SHIELD[4]
1-ethyl-3-(3-dimethylaminopropyl) carbodiimide (EDC) hydrochloride	Used to retain mRNA	None	High mRNA fixation efficiency Poor protein fixation efficiency	STARmap[174]
Sodium dodecyl sulfate (SDS), urea, borate and heat	Used for antigen retrieval	Oven	May enhance antibody staining Concentration of reagents and incubation length should be carefully determined	CLARITY[33], FLASH[12]
Decolourization (5–24 h)				
Amino alcohols (such as THEED)	Used for tissues that contain pigments such as kidney, liver, spleen and muscle (haem); skin (melanin); brain (lipofuscin)	None	Used to remove haem from blood (haemoglobin) and muscle (myoglobin)	CUBIC[24], FlyClear[13]
N-alkyl imidazole		None	Effective at haem removal	CUBIC[25]
N-methyl diethanolamine (NMDEA)		None	Effective at haem removal	SHANEL[6]
Bleaching by hydrogen peroxide		None	Widely effective across many pigments Can cause tissue damage if left too long or used at too high a concentration	iDISCO[47]
Quenching autofluorescence (12–24 h)				
Photobleaching with high-intensity light	Used when tissues have high autofluorescence (human brain)	LED array inside refrigeration unit	Broadband white light is most effective Will bleach genetically encoded fluorescent proteins	ELAST[31], multispectral LED array[30]
Use of red and far-red fluorophores		Antibody-conjugated fluorescent dyes	Use dyes with emission at wavelengths >600 nm	iDISCO[47]
Hydrogel embedding (12–24 h)				
Acrylamide, bis-acrylamide and PFA	Used to retain low-expression biomolecules Used to stabilize fragile tissues Used to retain mRNA Required when performing tissue expansion	Heat block under vacuum	Best for retention of mRNA and low-expression proteins Gel density can be adjusted to promote clearing and labelling (less dense) or biomolecule retention (more dense)	CLARITY[33], PACT/PARS[34]
Acrylamide		Heat block under vacuum	Acrylamide is polymerized in the absence of crosslinking molecules (bis-acrylamide), creating a stretchable gel	ELAST[31]
Acrylamide, acrylate, protein enzymes, detergents and imidazole		Incubator	Hydrogels can expand many-fold when placed in pure water (or an imidazole solution in the case of CUBIC-X)	ExM[35], ProExM[36], MAP[37], CUBIC-X[38], iExM[39]
Decalcification (12 h–3 weeks)				
EDTA and imidazole	Required when clearing tissue containing calcified bone	None	Used to remove calcification in tissue	CUBIC-B[25], PEGASOS[42], PACT-deCAL[43], bone CLARITY[44], vDISCO[45]

Table 1 (cont.) | **Tissue clearing modules**

Modules and reagents	Indications for use	Required equipment	Additional considerations	Originating protocol
Delipidation (1 h–3 days)				
By solvent	Required to clear any tissue >0.2 mm thick	None	Tissue must first be dehydrated with tetrahydrofuran (THF) or alcohol If tissue contains fluorescent proteins, dehydrating solutions must be maintained at 4 °C and pH >9.0. Consider supplementing with: butylated hydroxytoluene or THEED and polyethylene glycol (PEG) Complete delipidation requires additional incubation in dichloromethane (DCM)	fDISCO[49], sDISCO[50], uDISCO[9], a-uDISCO[52], FluoClearBABB[51], PEGASOS[42]
By detergent		Optional: electrophoretic tissue clearing (ETC) device	Most common detergents: SDS, Triton X-100, CHAPS Degree of clearing increased by alkaline pH, increased temperature and increased incubation time	CLARITY[33], PACT-PARS[34], CUBIC[23]
By solvent and detergent		None	Must be performed sequentially	Adipo-Clear[57], SHANEL[6]
Refractive index matching (1 h–2 days)				
In solvent	Required for all tissue clearing experiments	None	Commonly used solvents: BABB, dibenzyl ether (DBE) and ethyl cinnamate If tissue contains fluorescent proteins, a pH >9.0 should be maintained. Consider supplementing with triethylamine, THEED, DL-α-tocopherol, propyl gallate, DPE or PEG RI should be ~1.56	sDISCO[50], uDISCO[9], PEGASOS[42]
In aqueous solution		None	Commonly used reagents are antipyrine and nicotinamide; *N*-methylacetamide and Histodenz; or TDE, DMSO and iohexol RI should be ~1.52	CUBIC[70], Ce3D, ELAST[31]
With expansion		None	Use pure water with RI 1.33 (ExM, ProExM, iExM, MAP) or 5% imidazole/55% antipyrine with RI 1.467 (CUBIC-X) solutions for RI matching	ExM[35], ProExM[36], MAP[37], CUBIC-X[38], iExM[39]

BABB, benzyl alcohol benzyl benzoate; CHAPS, 3-[(3-cholamidopropyl)dimethylammonio]-1-propanesulfonate; DMSO, dimethyl sulfoxide; DPE, diphenyl ether; EDTA, ethylenediaminetetraacetic acid; LED, light-emitting diode; RI, refractive index; TDE, 2,2-thiodiethanol; THEED, *N*,*N*,*N*′,*N*′-tetrakis(2-hydroxypropyl) ethylenediamine.

to determine which best retains your targets of interest while still allowing for sufficient and timely clearing. For example, thicker or denser tissues may require use of the SWITCH method coupled with relatively low fixative concentrations to enable uniform fixation within a reasonable amount of time.

Optional pre-treatments

Preparing a cleared sample most often involves removing lipids from the sample and placing it in a solution matched to the RI of the remaining tissue components (usually protein, RI >1.5). Refractive index matching alone may be adequate for clearing thin (<0.2 mm), non-pigmented samples; however, most tissues require additional processing. The pre-treatment steps below are optional. Some are needed for specific tissue types, while others have a more general application. Experimentation on smaller samples is advised to identify which are necessary for a particular tissue of interest.

Decolourization. Many tissues contain natural endogenous pigments that can absorb light and prevent effective clearing and imaging, and in large tissue volumes even sparse pigments are obstacles to acquiring high-contrast images[2,3,10,22]. Haem is the most abundant chromophore found throughout tissues and is associated with haemoglobin and myoglobin pigments found in the blood and muscles, respectively. Blood can be removed after an animal is sacrificed by transcardial perfusion of large volumes of isotonic buffer; however, perfusion with PBS alone is insufficient to remove all haem from blood-rich and muscle-rich tissues such as the kidney, heart, muscle and liver. Extensive chemical screening has identified that amino alcohols effectively elute haem from both blood and muscle[23]; these chemicals (specifically *N*,*N*,*N*′,*N*′-tetrakis(2-hydroxypropyl)ethylenediamine (THEED; also known as Quadrol)) also assist in lipid extraction, are compatible with fluorescent proteins and are a key component in the CUBIC tissue clearing protocols[11,24].

The amino alcohol *N*-methyldiethanolamine (NMDEA), in conjunction with 3-[(3-cholamidopropyl)dimethylammonio]-1-propanesulfonate (CHAPS) detergent can effectively remove haem while permeabilizing and delipidating tissue[6]. *N*-alkylimidazole also has high utility for haem elution[25]. Killed animals can be perfused with any of these haem-solvating chemicals, or individual tissues — including human tissue — can be incubated with them after dissection.

Additional endogenous chromophores may be present depending on the tissue. Pigments of the compound eye such as pteridine and ommochrome and melanin in skin can be particularly difficult to remove. THEED has been shown to be effective at removing pigments of the compound fly eye while preserving green fluorescent protein (GFP) and mCherry emission (FlyClear[13]).

A more generalized method for decolourization is to break the chemical bonds of pigments using peroxides, a process often referred to as bleaching[15,26–29]. Bleaching gives powerful decolourization performance, although it requires optimization of the peroxide concentration and treatment duration to avoid excessive damage to the tissue. Furthermore, as peroxide treatment destroys the central chromophore of fluorescent proteins and bleaches some organic dye molecules, downstream immunostaining is required to visualize quenched fluorescent proteins, and any fluorescent labelling must be carried out after the bleaching step.

Quenching autofluorescence. Autofluorescence can decrease the signal to noise ratio (SNR) and reduce contrast when imaging. To avoid this, samples can be photobleached to eliminate autofluorescence before staining. Photobleaching can be accomplished by exposing the tissue to broadband light for an extended period; for example, exposure using a custom device containing broadband visible light-emitting diodes (LEDs) in a cold room for up to 3 days can reduce autofluorescence in thick tissue samples[30,31] (the cold room prevents tissue from overheating and degrading). A key disadvantage to this method is the need for immunostaining, as genetically encoded fluorescent proteins will be photobleached. A more common and efficient method to overcome autofluorescence is to select red and far-red dyes that fluoresce outside the 500–600 nm range within which most autofluorescence occurs. If red and far-red dyes are selected, autofluorescence in the 500–550 nm range can be imaged to derive useful information, for example, to identify anatomical structures or register the dataset against other samples or atlases (see Results section).

Hydrogel embedding. Hydrogel embedding techniques were originally developed to improve the mechanochemical properties of fixed tissue over standard PFA fixation. Hydrogel embedding technologies for tissue clearing employ the polymerization of monomer solutions containing varying compositions of acrylamide (AA), sodium acrylate (SA) and bis-acrylamide (Bis) molecules to generate polyacrylamide (pAAm) meshes that physically or chemically fix biomolecules in place. In recent years, researchers have harnessed the unique properties of hydrogels — such as their expandability and elasticity — to further enhance the applications of hydrogel embedding technologies. The fundamental principles and novel methods in tissue–hydrogel transformation technologies are covered in-depth in a recent review paper on the subject[32].

CLARITY was the first widely used hydrogel embedding technique[33]. CLARITY and its variants covalently anchor endogenous tissue biomolecules to a pAAm mesh that is generated from AA, PFA and Bis (FIG. 2). Bis serves to chemically crosslink separate acrylamide chains to form the pAAm mesh, while PFA serves to crosslink tissue molecules to the mesh and decrease protein loss. Bis and PFA can be excluded from the monomer solution to increase pore size for enhanced clearing and immunostaining, with a reduction in mechanochemical preservation and stability[34].

More recently, the elastic properties of pAAm hydrogels have been harnessed to increase the toughness of hydrogel-embedded tissue in a process called ELAST[31]. By significantly decreasing the Bis crosslinker concentration, more physical entanglement and less covalent crosslinking of long pAAm chains occurs. This decreases the rigidity and brittleness of the resulting tissue–gel, making it reversibly stretchable and more resistant to wear and tear when handled.

Certain hydrogels, such as the pAAm gels used in CLARITY, polymerize best when maintained in an oxygen-free environment, and their polymerization is often activated by a temperature-sensitive initiator. Custom (or commercial) equipment can be used to perform these steps; for example, a basic set-up involves placing a conical tube or plate warmer inside a vacuum chamber. The samples are placed under vacuum before heating the sample to 37 °C for approximately 3 h.

Another interesting property of hydrogels is their ability to expand. These expansion properties have been harnessed to physically expand hydrogel-embedded tissue–gels and thus increase the achievable spatial resolution of conventional light microscopy[35]. Although expansion occurs during the final RI-matching step, the fixed tissue must first be embedded in a polyacrylamide–polyacrylate gel that will later facilitate expansion in each dimension. Additionally, protein digestion or denaturation is required to permit final tissue expansion. This has been achieved using proteinase K (ExM[35]), LysC (Pro-ExM[36]), sodium dodecyl sulfate (SDS) (MAP[37]) or imidazole (CUBIC-X[38]). LysC, SDS and Triton X-100 are now the preferred strategies as these reagents are the least destructive to tissue and better preserve biomolecules for post-expansion labelling[36–38]. Recent protocols expand tissue up to 20× (iExM[39]) and allow for fine tuning of the degree of expansion (ZOOM[40]).

Decalcification. The clearing of limbs or whole vertebrates requires the decalcification of bone, as calcified bone is a strong light scatterer[2,3,10,22]. Between 50% and 70% of bone consists of carbonated hydroxyapatite (HAp) crystals distributed throughout a collagen matrix. Elution of calcium ions from HAp reduces light scattering and renders bony material transparent. Decalcification can be performed by submerging the sample in an acidic solution (as illustrated by the classic classroom experiment in which immersing an egg in vinegar renders the shell transparent); however, this causes substantial soft tissue damage. Neutral buffered saline solutions that contain the calcium ion chelator ethylenediaminetetraacetic acid (EDTA) are preferred[41], and EDTA has been used in many tissue clearing methods, including CUBIC-B[25], PEGASOS[42], PACT-deCAL[43], bone CLARITY[44] and vDISCO[45]. Interestingly, imidazole may further enhance the decalcifying and clearing effects of EDTA on bone tissue[25].

Delipidation

Removing lipids (delipidation) is crucial for successful tissue clearing as lipids act as an optical barrier to light and a physical barrier to fluorescent probe delivery.

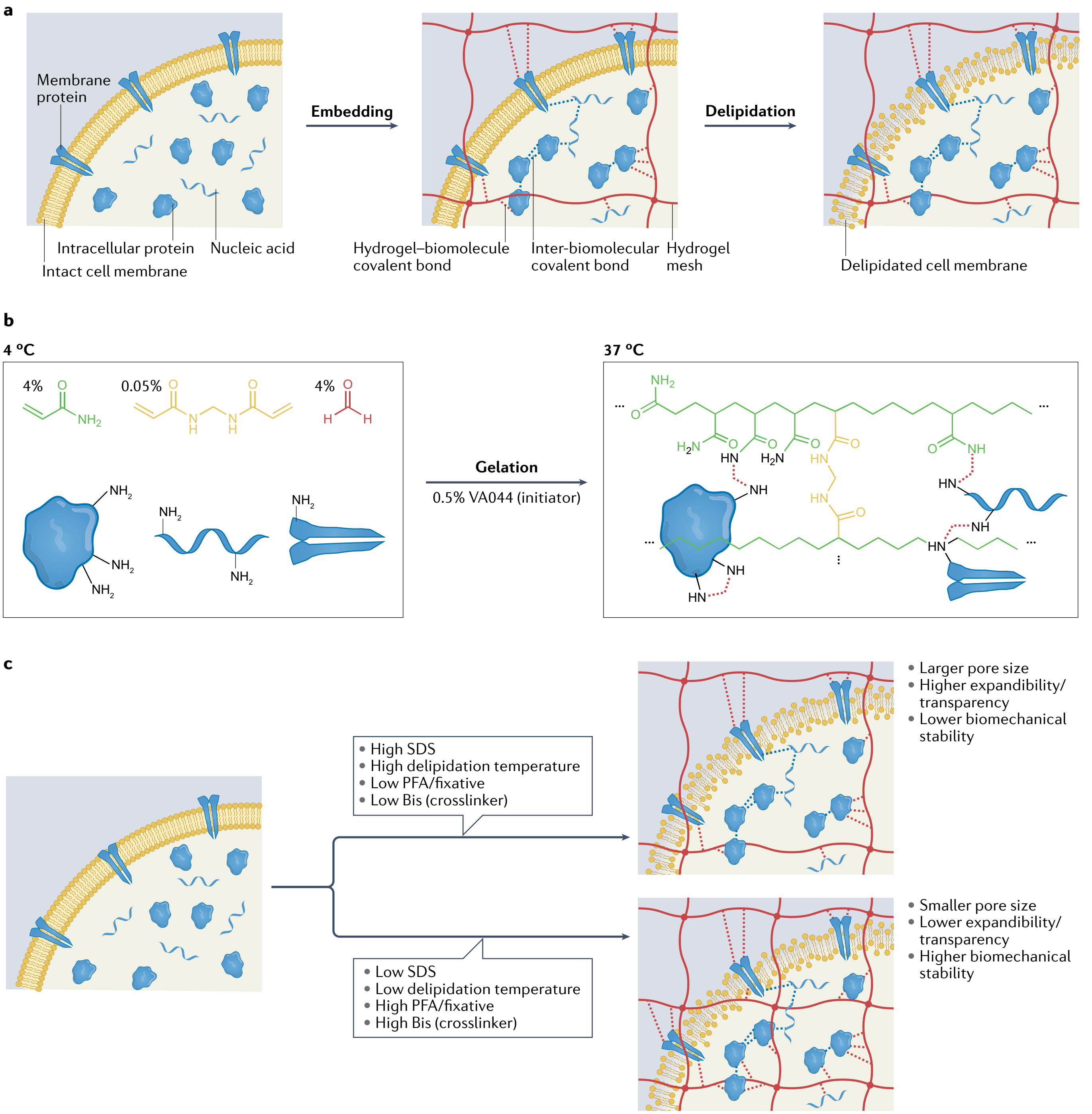

Fig. 2 | **Concept of hydrogel embedding. a** | Tissue biomolecules are fixed chemically or physically to a hydrogel mesh generated in situ, and then cell membranes are removed during delipidation to enable chemical transport and optical transparency. **b** | In CLARITY hydrogel embedding, paraformaldehyde (PFA, red), bis-acrylamide (Bis, yellow) and acrylamide (green) are used to covalently link the primary amines of proteins and nucleic acids to a polyacrylamide hydrogel mesh generated through free radical polymerization. Free radical generation and subsequent polymerization is initiated by the chemical VA044 when it is warmed to a temperature of 37 °C. **c** | The pore size, expandability, transparency and biomechanical stability of a tissue–hydrogel can be modulated on the basis of delipidation temperature and the concentrations of the sodium dodecyl sulfate (SDS) delipidation detergent, the PFA fixative and the Bis crosslinker.

	Pre-treatment/ co-treatment	Active molecules	Methodology
Solvent-based	Pre-treatment: dehydration (required)	• DCM	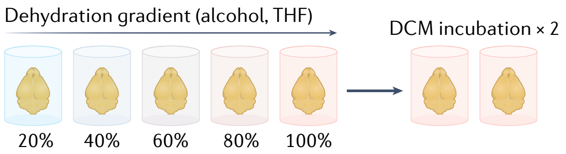 Dehydration gradient (alcohol, THF) DCM incubation × 2 20% 40% 60% 80% 100%
Detergent-based	Pre-treatment: hydrogel embedding (optional)	• SDS • Triton X-100 • CHAPS	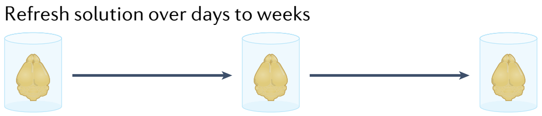 Refresh solution over days to weeks
Detergent + solvent	Co-treatment: dehydration (required)	• Triton X-100 • CHAPS • DCM	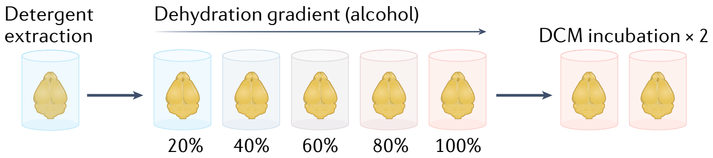 Detergent extraction Dehydration gradient (alcohol) DCM incubation × 2 20% 40% 60% 80% 100%
Electrical field	Pre-treatment: hydrogel embedding (required)	• SDS	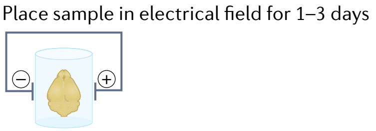 Place sample in electrical field for 1–3 days

Fig. 3 | **Protocols for delipidation.** A summary of methods for delipidating tissue using the most common detergents and solvents. The methodology example represents clearing of a murine brain. CHAPS, 3-((3-cholamidopropyl) dimethylammonio)-1-propanesulfonate; DCM, dichloromethane; SDS, sodium dodecyl sulfate; THF, tetrahydrofuran.

Delipidation can be performed using solvents, detergents or a combination of the two, and can be achieved passively or with the aid of an electrical field (FIG. 3). Delipidation of hydrogel-embedded samples is primarily performed with detergents in aqueous buffer to prevent dehydration of the gel.

Solvent-based delipidation. Solvent-based delipidation involves submersion of the tissue in a series of solutions (FIG. 3). First, an initial dehydration step serves to permeabilize cell membranes, initiate some lipid solvation and enhance tissue bleaching if the final dehydrating agent is combined with peroxides[46,47]. Dehydration is performed by moving the tissue through solutions with an increasing concentration of a water-miscible organic solvent. This process can cause tissue shrinkage, although increasing the number of steps in the gradient can minimize this effect and better preserve morphology[46]. Preservation of nominal sample size and morphology is often essential for registration to an anatomical atlas (see below).

Historically, tetrahydrofuran (THF), ethanol or methanol have been used for dehydration, although these reagents have notable disadvantages. Rapid dehydration using THF can cause unwanted morphological changes[46]. Furthermore, tissues with a high lipid content do not clear well when dehydrated with ethanol as it does not have the same delipidating effect as methanol or THF (see below)[48]. Similarly, dehydrating tissues with THF, ethanol or methanol will quench fluorescent proteins, as removing water molecules from the chromophore of fluorescent proteins causes a conformational change that eliminates fluorescence emission. Methanol and ethanol quench fluorescent proteins within hours[46–48]. Fluorescence can be maintained in THF for a few days if the pH remains above 9.0 (as in fDISCO[49]), dehydration and clearing is performed at 4 °C (fDISCO[49]) and/or by adding butylated hydroxytoluene (sDISCO[50]). Because of this quenching effect, THF, ethanol and methanol are rarely used to clear tissues expressing fluorescent proteins and these tissues are instead best dehydrated using 1-propanol or tert-butanol (FluoClearBABB[51]). If tert-butanol dehydration is performed step-wise (uDISCO[9]), in alkaline conditions (a-uDISCO[52]) or mixed with THEED and polyethylene glycol (PEGASOS[42]), GFP fluorescence can be preserved for longer than a month. Methanol, ethanol and THF are still used for dehydration of tissues that are stable in organic solvents. Methanol, ethanol and THF provide the strongest dehydration and delipidation effects, which is important for achieving large tissue transparency. Tissue dehydration can affect the interactions of antibodies with their epitopes, either enhancing or preventing binding, and this effect must be independently tested for each novel antibody used[47].

All the dehydrating agents described above perform some degree of delipidation. However, this is not sufficient to produce a well-cleared final sample. Therefore, an additional incubation in dichloromethane (DCM) — a water-immiscible solvent — is performed to complete lipid removal from the tissue[53,54]. DCM induces the creation of inverse lipid micelles, which diffuse out of the tissue (FIG. 4). Owing to the high immiscibility of water in DCM, care must be taken to ensure that all water has been removed from the sample before submerging it in this solvent.

Detergent-based delipidation for aqueous-based clearing. As fixation is performed in aqueous buffers supplemented with fixative, these samples can be directly delipidated using detergents (FIG. 3). The most commonly used detergents are SDS, Triton X-100 and CHAPS. Detergents act by disrupting lipid bilayers and forming micelles that can be transported out of the tissue (FIG. 4). Alkaline pH, higher temperature and longer incubations can all enhance the degree of detergent-based delipidation and result in more chemically and optically permeable tissue. Delipidation buffers generally contain 4%–10% detergent and are incubated at or above room temperature to prevent the solution from becoming supersaturated. Incubation can take from hours to months depending on the tissue type, size, method of micelle removal and the desired level of clearing[5,6,11,24,25,33,55,56].

Detergents other than SDS and Triton X-100 have been used for delipidation, including sodium lauryl sulfate

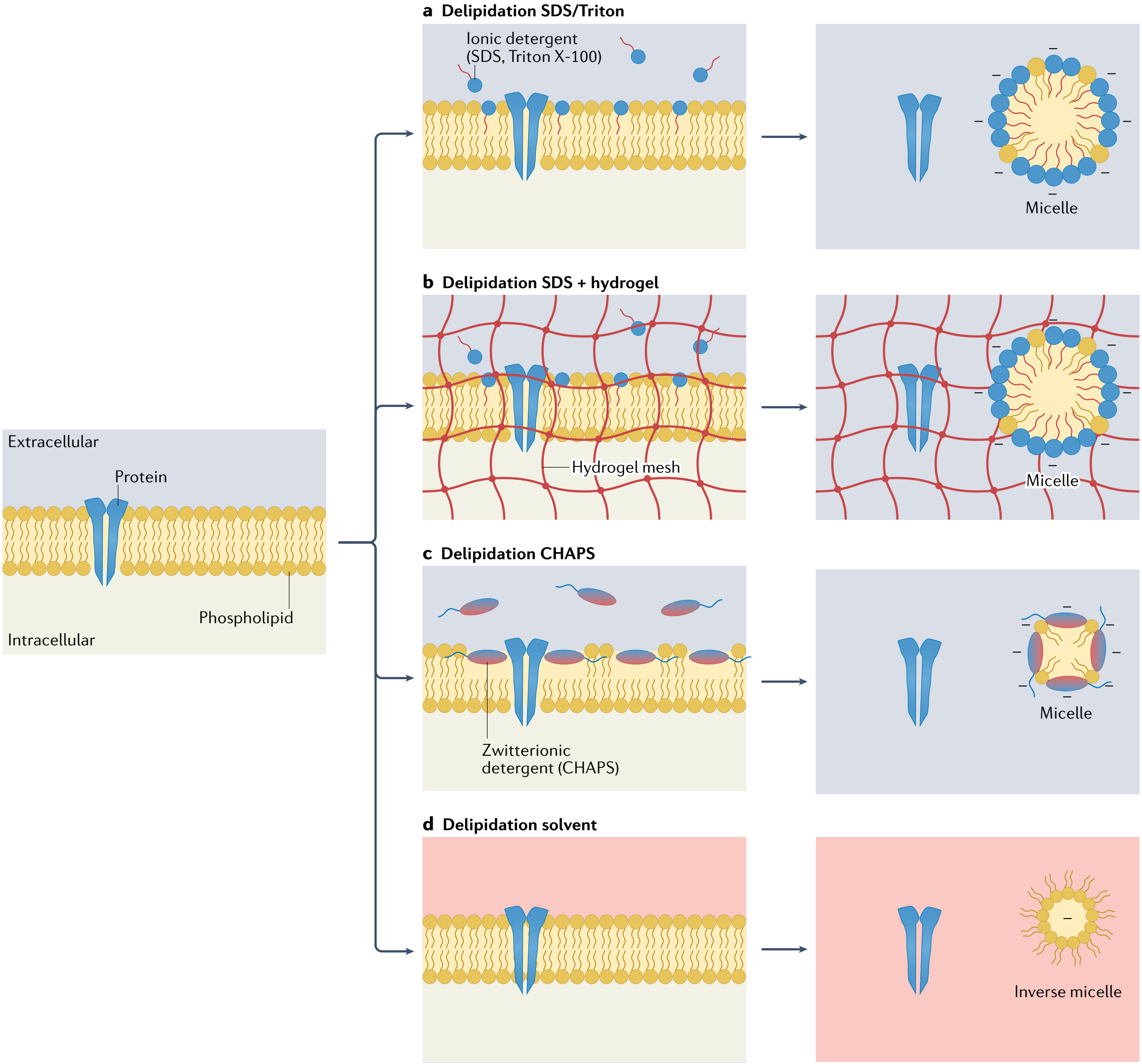

Fig. 4 | **Mechanisms of delipidation. a** | The long non-polar tails of ionic detergents such as sodium dodecyl sulfate (SDS) or Triton X-100 intercalate with membrane lipids. If the detergent concentration is high enough, large micelles will form consisting of detergent and membrane lipids. **b** | Intercalation of membrane lipids by ionic detergents can occur in the presence of a hydrogel mesh. **c** | The hydrophobic moiety of zwitterionic detergents such as 3-((3-cholamidopropyl)dimethylammonio)-1-propanesulfonate (CHAPS) embed into the top of the plasma membrane. If the detergent concentration is high enough, small micelles will form. **d** | When tissues are transitioned from an aqueous liquid (polar) to a solvent (non-polar), membrane lipids form reverse micelles in which their non-polar tails are oriented towards the surrounding solvent environment. In all situations, micelles migrate out of the tissue and are washed away.

(SLS) in the CLARITY[33] workflow, sodium dodecylbenzene sulfonate in CUBIC-HL[25], Tween-20 in FocusClear[1] and 1,2-hexandiol[25]. CHAPS (used in the SHANEL workflow[6]) has also shown utility in very large samples as it generates smaller micelles than other detergents, which can diffuse out of the tissue more quickly (FIG. 4).

Combined solvent and detergent delipidation. Physiological lipids have varying levels of polarity. Some lipids are better removed by detergents, others are better extracted through dehydration and delipidation by solvents. Lipid-rich tissues can therefore benefit from the use of both detergents and solvents for delipidation (FIG. 3). Adipose tissue, for example, can be delipified by first incubating with 0.1% (v/v) Triton X-100 followed by a methanol dehydration and further lipid extraction with DCM, as shown in the Adipo-Clear[57] workflow. Likewise, insufficient delipidation by ethanol and DCM can be compensated for through an initial incubation with CHAPS, a strategy used in the SHANEL[6] workflow.

Delipidation using electrical fields. The speed of delipidation in large, thick tissue samples is limited by the rate that SDS and lipid micelles diffuse in and out of the sample, respectively. This rate can be increased using electrical fields (FIG. 3). Unidirectional electrical fields were first used for this task[33] and are now implemented in many commercial electrophoretic tissue clearing (ETC) devices. ETC devices can speed delipidation dramatically, accomplishing in a day what can take weeks by passive diffusion; however, unidirectional electrical fields can produce unequal lipid extraction, as lipid micelles nearest the anode are forced to traverse through the entire sample. This differential delipidation, along with the electrical force exerted on the tissue, can cause malformation of the tissue during the ETC process. A more efficient way to delipidate a sample is to use a rotating electrical field or rotate the sample within a unidirectional field. This process, referred to as stochastic electrotransport, enhances the diffusion of highly electromobile species such as lipid micelles, while keeping species with low electromobility such as other tissue biomolecules relatively stationary[58]. Hydrogel embedding, and crosslinking of biomolecules of interest to the gel are requirements for ETC to maintain tissue stability and to retain electromobile molecules of interest. The original publications contain design suggestions for ETC[33] and stochastic electrotransport[58] hardware and both can now be purchased commercially.

Labelling

Extracting biologically meaningful information from transparent tissues requires specific and uniform fluorescent staining of target molecules such as nucleic acids or proteins. Small-molecule dyes such as the nuclear dyes DAPI (4′,6-diamidino-2-phenylindole), propidium iodide, RedDot2 and SYTO[3,24,33,42] and membrane-integrating dyes such as fixable DiI can diffuse or be perfused through biological tissue. Other fluorescent dyes can be targeted to molecules of interest using short peptide tags[59] or antibodies. Passive diffusion of small molecules and antibodies is slow and the diffusion timescale correlates quadratically with the tissue thickness; when staining tissue at the organ scale, it can take days for the label to completely permeate to the core of the tissue[60].

There are many well-documented variables that need to be optimized for any immunostaining protocol, including fixation conditions, antibody concentrations, temperature and time[61]. These optimizations are best carried out on thin (~200 μm) tissue sections and imaged on a confocal microscope to ensure complete penetration through to the middle of the section. Canonical labelling with antibodies requires the use of two large molecules: a primary antibody that recognizes the molecular target and a secondary antibody that carries the fluorophore[24,45,47]. Labelling with multiple primary antibodies creates further complication, as the optimal conditions for each antibody may be different. Once uniform staining of a thin section has been established, the antibody concentrations can likely stay the same for thicker tissue, and the volume of antibody solution is increased. Each antibody also has a unique rate of denaturation that increases with temperature. Highly unstable antibodies must be incubated at lower temperatures and replenished if staining protocols last multiple days.

The largest barrier to scaling up an immunolabelling protocol is that the combination of the slow movement and high affinity of the antibody label results in the aggregation of the antibody at the surface of the sample[5]. Below, we outline several methods to prevent surface aggregation by reducing the distance the label must travel or temporarily manipulating its affinity for its target. Together, these methods permit more rapid and homogeneous labelling of large, cleared tissues.

Reduce sample size. The simplest method to improve labelling speed is to reduce the size of the sample. Before initiating a clearing experiment, the tissue should be trimmed as small as possible. Dehydration can decrease sample volume by up to 60% if used, with the rate that the tissue is dehydrated influencing the level of shrinking. Some researchers have embraced this shrinking effect to allow more rapid labelling and imaging[9]. It should be noted that shrinking the sample will also decrease the achievable resolution when imaging as some components of the tissue will have moved closer than the diffraction limit of a light microscope[62]. Reversible shrinkage can be exploited to speed up the labelling process; if a tissue is infiltrated with a tough and elastic hydrogel, the sample can be reversibly compressed to one-sixth of its original size[31]. Labelling can be performed in the compressed state, decreasing the distance that molecular labels must diffuse to their targets. Similarly, high-ionic-strength solutions can be used to temporarily shrink non-elastic tissue during the staining process[5]. If reversible shrinkage is used for labelling, the sample is returned to its original size before imaging to avoid compromising the final image resolution.

Reduce label size. Smaller labels can diffuse more quickly through a tissue and the use of small-molecule fluorescent dyes with affinity for specific molecular targets is advantageous over antibodies when possible.

Nanobodies (~15 kDa) are one-tenth the size of a conventional antibody (~150 kDa) and show high tissue penetration and high thermal and/or chemical stability; these labelled single-variable-domain antibodies from Camelidae or shark species[63] have been shown to rapidly diffuse through fixed and cleared tissue, decreasing labelling time up to fivefold[45,60] over antibodies. Although labelling with nanobodies is fast, it should be noted it can also result in a relatively dim fluorescent signal. Standard immunolabelling protocols use polyclonal secondary antibodies, which can bind at multiple regions of a single primary antibody, thereby amplifying the fluorescence signal. Nanobody labelling is a single step process in which only one nanobody binds to each biomolecule of interest; therefore, no signal amplification occurs. Additionally, commercially available nanobodies are still limited to a small range of targets, although this range is rapidly increasing.

Increase porosity. Lipid membranes in biological tissue prevent the diffusion of imaging agents, and immunolabelling is therefore often performed after delipidation. However, certain pre-treatment or delipidation steps may deplete or alter the target of interest, requiring immunolabelling to be performed first. In addition to delipidation by detergents[6,23,33,34,64] or solvents[6], weak fixation[65], partial protein digestion[5,65–67] or increasing the pore size of hydrogels can improve label diffusion[34]. Furthermore, it is possible to harness the natural porosity of tissue for label delivery; for example, transcardial perfusion of fluorescent labels during pre-treatment is an excellent method for labelling whole animals[11,34,45]. Unfortunately, this perfusion technique is technically demanding and requires large amounts of label.

Manipulate label affinity. The binding affinity of fluorescent labels can be manipulated to allow them to diffuse freely throughout the tissue before their binding properties are reactivated in a way analogous to the SWITCH method described above. For ionic bonding stains such as nuclear stains, high salt concentrations can be used to inhibit binding until homogeneous tissue distribution is achieved[5,23]. Alternatively, antibody binding can be temporarily inhibited ('turned off') by introducing urea, THEED or SDS to a physiological buffer solution, or increasing the temperature or pH[5,20,23,55]. Once the antibody has distributed itself throughout the tissue, the tissue is returned to the standard buffer solution and binding will be activated ('turned on'). Careful optimization of solute concentration, temperature and pH is required if using this technique, as antibodies can undergo irreversible denaturation and lose their binding capability when exposed to the above conditions. Changes in temperature and antibody concentration and/or the addition of THEED or urea appear to affect antibody penetration. Conversely, changes to salt and detergent concentrations tend to influence binding efficiency[5,23,55]. Finally, use of primary and secondary antibody complexes — pre-formed by co-incubating these antibodies before applying them to the sample — requires only a single diffusion event and results in a twofold decrease in labelling time.

Apply an outside force. Certain fluorescent dyes and antibodies are electromobile, and stochastic electrotransport can be used to increase the speed at which these labels move through a cleared tissue sample[20,58]. When a SWITCH method is combined with stochastic electrotransport, multiple, rapid rounds of labelling can be performed. This methodology (eFLASH[20]) enables a highly multiplexed approach to investigating cleared tissues, whereby tens of target molecules can be investigated in a single sample instead of the standard three or four. A custom (now commercially available) active immunolabelling device is needed to speed labelling; the device consists of a sample chamber across which an electrical field can be applied and the sample or the electrical field rotated. Active cooling is required to prevent heat damage to the sample. Another option to further increase the labelling speed is to focus the electrical field by adding magnets to the sides of the sample chamber. This technique, referred to as electromagnetic focused immunohistochemistry (EFIC) or magnetohydrodynamic force (MDH), drives the labels into the tissue and prevents them from flowing around the outside of the tissue[68,69].

Refractive index matching

The last step of any clearing protocol involves immersing the sample in a final clearing solution. This solution must match the RI of the remaining biological components — primarily protein — and be miscible with the solutions used before it. The optimal RI for final clearing should be 1.50–1.60 to best match the remaining protein in the sample after delipidation (with an exception for expanded samples, see below). Care must be taken to ensure that fluorescent labels are compatible with the chosen solution. Post-fixation in 4% PFA may be required to better retain antibody labels, although this will prevent de-staining and is therefore incompatible with multi-round labelling. A wide variety of solutions have been used and are categorized as aqueous based or solvent based; formerly, aqueous solutions better preserved fluorescent protein emissions, whereas solvents better cleared tissue owing to their higher RI. These differences are much less pronounced owing to recent advances.

Aqueous-based solutions. Many hydrophilic tissue clearing reagents have been reported, from simple sugars such as sucrose and fructose to advanced chemistries such as the medical grade gastrointestinal imaging reagent iohexol[2,3,10,22]. RI-matching solutions must achieve an RI of 1.50–1.60 in non-expanded samples; however, owing to solubility limitations in water, many aqueous solutions of these reagents can only reach an RI of ~1.45. A new generation of aqueous solutions are now available that can match the clearing potential of solvents; these use high-RI chemicals that have high solubility in water, including antipyrine–nicotinamide (CUBIC-R[70], RI 1.52–1.54), *N*-methylacetamide–histodenz (Ce3D[71], RI 1.50) and 2,2-thiodiethanol (TDE)–dimethyl sulfoxide (DMSO)–iohexol (dPROTOS[31], RI 1.52).

It should be noted that the expansion or contraction of a sample will affect its RI. Aqueously cleared samples do not contract and therefore do not require as high an RI for their final clearing solution (RI ~1.52) as dehydrated

Dipping objectives
Objective lenses that are designed to be submerged into a liquid. Dipping objectives are found on upright microscopes, and samples are mounted without a coverslip.

solvent cleared samples (RI ~1.56). In the most extreme examples, in which hydrogel-embedded tissues are expanded 4–20 times, the sample is primarily composed of water and has an RI near 1.33; no specialized clearing solution is needed for these types of expansion method.

Solvent-based solutions. If samples have been dehydrated and delipidated in solvents, the remaining tissue can be rendered optically transparent by impregnating it with an additional high-RI solvent. Formerly, this has included benzyl alcohol–benzyl benzoate (BABB) or dibenzyl ether (DBE)[53,54]. Like the dehydrating solutions described above, BABB and DBE can quench fluorophores contained in the sample. Several approaches can improve fluorescent protein preservation during BABB or DBE incubation, including maintaining a basic pH by supplementing the final clearing solution with triethylamine[51] or THEED[42] and preventing peroxide formation by adding DL-α-tocopherol[9] or propyl gallate[50]. Additional fluorescent protein preservation has been achieved through the incorporation of diphenyl ether (DPE[9]) or poly(ethylene glycol) methyl ether methacrylate (PEGMMA[42]). Supplementing BABB and DBE with the fluorescent protein protectants described above can preserve fluorescence emission for weeks to months in the cleared tissue[8,42,50,51].

The toxicity of solvents, particularly BABB, remains a concern for some researchers and multi-user core facilities where cleared samples are often imaged. Ethyl cinnamate and TDE are less toxic alternatives that can be used to clear tissue. Ethyl cinnamate has shown equivalent clearing effects and prolonged fluorescent protein emission relative to BABB and DBE when clearing mouse organs[72]. A 97% TDE water solution results in a RI similar to those of BABB and DBE; however, many fluorescent dyes become unstable in TDE at this concentration[73–75]. Therefore, TDE is better suited to increase the RI of aqueous clearing solutions when used at concentrations below 70% (v/v) as described above.

Imaging

Cleared tissue samples require imaging techniques capable of optical sectioning over scales of millimetres to centimetres. Some technologies, such as confocal microscopy and two-photon microscopy, are widely accessible in individual labs and institutional core facilities whereas others, such as light-sheet microscopy and optical projection tomography, are more limited. Additional components such as special objectives or sample holders may also be required.

TABLE 2 displays a comparison of several microscope modalities commonly used for imaging cleared tissue samples.

Point-scanning and spinning disc confocal microscopes are the most widely available optical sectioning microscopes. Upright point-scanning confocal microscopes equipped with high numerical aperture, long working distance dipping objectives produce the highest quality images of cleared tissue. Inverted point-scanning confocal microscopes are limited in imaging depth and resolution (TABLE 2) owing to the need to use long working distance air objectives that cause sample-induced spherical aberrations when imaging thick, cleared tissues[76]. Spinning disc microscopes allow fast acquisition of 3D volumes, but quickly experience a loss of confocality as they image deeper into tissue and are often optimized for use with high-numerical aperture objectives with working distances of less than 200 µm. Two-photon excitation is advantageous for imaging cleared tissue as it can extend the imaging depth over standard confocal microscopy for less optimally cleared samples and eliminates out-of-plane photobleaching when imaging large axial volumes. Unfortunately, both point-scanning confocal and two-photon microscopes are slow and can require tens of seconds to image a single field of view, and imaging samples greater than 1–3 mm^3 in size requires a faster approach.

Light-sheet microscopes have quickly become the preferred system for imaging cleared tissue. This

Table 2 | **Microscopy options for imaging cleared tissue**

Microscopy technique	Best for	Not for use with	Speed	Numerical aperture range[a]	Approximate resolution (lateral, axial)[b]	Availability
Spinning disc confocal	Samples <100 µm thick Fast imaging	Samples >200 µm (when disc optimized for high numerical aperture)	Fast	Up to 1.4 (for <200 µm working distance oil immersion objectives)	250 nm, 400 nm	High
Point-scanning confocal (inverted)	Samples <2 mm thick Subcellular resolution	Samples prone to bleaching	Slow	Up to 0.5 (for long-distance air objectives)	700 nm, 4 µm	High
Point-scanning confocal (upright)	Samples <6 mm thick Subcellular resolution	Samples prone to bleaching	Slow	Up to 1.1 with dipping objectives	300 nm, 750 nm	High
Two-photon (upright)	Samples <6 mm thick Subcellular resolution	Multicolour (>2) imaging	Slowest	Up to 1.1 with dipping objectives	300 nm, 750 nm	High
Light sheet	Samples <6 cm thick Cellular resolution	High resolution/ subcellular imaging	Fastest	Below 0.5 (for low magnification air objectives)	700 nm, 5 µm	Lower
Optical projection tomography	Samples <5 mm thick Isotropic imaging	High resolution/ subcellular imaging	Fast	Below 0.1 (for low magnification air objectives)	3 µm, 3 µm	Lowest

[a] Higher numerical aperture values achieve better resolution. [b] Assumes emission light at a wavelength of 550 nm; calculated at highest numerical aperture for each modality.

is primarily owing to their speed, which arises from the perpendicular orientation of the excitation and detection objectives. Cleared tissues are well suited to light-sheet microscopy as the lack of scattering inside the tissue allows light sheets to be stably projected through the tissue, and the emitted fluorescence can traverse large spans of tissue to the detection objective without scattering. Light-sheet systems can be optimized for high-resolution imaging using short, thin excitation sheets or lattice light sheets, although these configurations have steric hindrances that prevent the imaging of cleared tissue greater than 100–200 µm in size. Systems can be optimized for larger samples using long, thick excitation sheets and low-resolution (numerical aperture <0.5), large-field-of-view detection objectives (for example, the ultramicroscope[48]), where the light sheet (5–10 µm) determines the thickness of the optical section. Whenever we refer to light-sheet microscopy in this Primer, we refer specifically to these high-capacity systems, which can image a cm^3 volume in minutes to hours depending on the desired resolution and sample properties.

Optical projection tomography (OPT) can also be used for imaging cleared samples. By rotating the sample during imaging, OPT can achieve isotropic spatial resolution. OPT achieves a lower lateral and higher axial resolution than light-sheet or confocal microscopes using similar optics. Imaging can be accomplished in minutes to hours if the sample fits in a single field of view. A limitation of OPT is that the sample cannot be larger than a few millimetres in each dimension. OPT has primarily been used for imaging small vertebrate embryos and intact rodent organs that fit these dimensions and only require low-resolution imaging (cellular resolution at best)[77,78].

Objectives. Two categories of detection objectives are used for imaging cleared tissue: clearing-specific, high-numerical aperture dipping objectives and low-numerical aperture air objectives. The decision of which objective to select is sample independent and solely based on the imaging system used and the level of resolution required. Dipping objectives are primarily used on upright point-scanning confocal or multi-photon microscopes and are also to be found in certain light-sheet designs. Dipping objectives for cleared tissue imaging optimally have a high numerical aperture (>0.9), long working distance (>5 mm), low magnification (<25×) and correction collars to allow imaging in solutions of varying RI. These objectives enable subcellular resolution imaging. Low-numerical aperture air objectives are more commonly used on light-sheet systems and are not recommended for use with confocal or multi-photon microscopes as they have poor axial resolution and suffer from sample-induced spherical aberration. Preventing sample-induced spherical aberration requires methods that ensure the path length that light travels through air is constant at all axial positions, for example, by fixing objectives in place and translating the sample or placing a dipping cap over the objective[76].

Data handling

Tissue clearing experiments, especially when performed at scale, produce large amounts of data. For simple experiments such as imaging single fields of view in tissues <500 µm thick, the microscope's acquisition computer or a standard desktop will suffice. However, imaging intact organs or animals is data intensive and can require extensive IT investment. Whereas confocal and multi-photon microscopes produce 5–10 GB of data per hour per colour channel, light-sheet microscopes can produce hundreds of gigabytes of data per hour; indeed, a single sample labelled with two or three fluorophores and imaged using light-sheet microscopy can produce more than a terabyte of data. Researchers aiming to perform large-scale or high-throughput imaging of cleared tissue must carefully consider their IT infrastructure to account for these high rates of data production, and it should be noted that the investment in IT infrastructure could equal or exceed the costs associated with purchasing the imaging system itself. The first consideration is whether to procure local or cloud storage. If a local data centre exists, expanding its storage capacity may be more cost effective than renting cloud space. Network upgrades may also be needed as the transfer of datasets hundreds of gigabytes to terabytes in size is prohibitively slow over a standard 1 Gbit s^{-1} network; 10 Gbit s^{-1} or higher speeds are preferred. Installing microscopes, data storage and workstations in close physical proximity — preferably on the same network switch — will increase transfer speeds and aid in network stability. If renting cloud storage, researchers may need to purchase dedicated bandwidth between their location and the cloud storage server to ensure uploads occur at practical speeds. It is essential to consider the data output of tissue clearing experiments from the early planning stages and ensure that adequate IT infrastructure exists.

Results

At the completion of a tissue clearing experiment, a researcher can expect to obtain a sample through which a fluorescence microscope can image beyond the standard limit of 50–100 µm imposed by light scatter. How much deeper will be a function of the tissue composition and the clearing protocol. It is common for large cleared tissues to retain a yellow tint owing to the continued absorption of blue and near-UV light by the remaining protein in the sample (FIG. 5) and a lack of this yellow colour in large samples may even indicate a loss of protein during the clearing process. The most common qualitative method for determining the effectiveness of clearing is to place the tissue over printed text and attempt to read the words below. A transilluminator with text or a grid printed on a transparent film can allow for better viewing. A more quantitative approach is to remove a >1 mm section of cleared tissue and view it under a dark-field microscope; when compared with uncleared tissue, the cleared tissue should not be visible under dark-field illumination owing to lack of light scatter. The most quantitative method is to analyse proton concentration across a sample using MRI; again, the less contrast that is visible, the better cleared the tissue is[79].

The integration of tissue clearing and high-resolution light-sheet microscopy has enabled the volumetric

Lattice light sheets
Light sheets that are formed using a specialized interference pattern that results in the projection of thin beams of excitation light into a sample, which are rapidly dithered to form the light sheet.

Steric hindrances
Refers to the inability to mount a sample on a microscope when the working distance of the objective is shorter than the thinnest dimension of the sample.

Optical section
An image of a 2D plane within a 3D object that is derived by optical, rather than mechanical, means.

Isotropic spatial resolution
Refers to specialized light microscopy techniques that produce an identical lateral and axial resolution.

Network switch
A computer network hardware device that allows multiple computers to communicate.

visualization of large biological specimens while simultaneously creating challenges for the subsequent assessment of cellular content. Analysis of cleared tissue imaging data can be intensive and time consuming by eye and requires image analysis routines, algorithms and software. Many open source and commercial tools now exist in this space. Some general software tools capable of handling large data files include the BigDataBrowser for Fiji/ImageJ[80], Napari, Arivis Vision4D, Imaris and Aivia. Data analysis routines for cleared tissue follow five basic steps: correction of imaging-induced artefacts; filtering to improve contrast; segmentation of objects and assessment of segmentation accuracy; registration to anatomical atlases (optional); and quantitative measurements of segmented objects. Quantitative measurements can take several forms, including object counting, volume measurements, distance measurements, determination of colocalization and tracing of filamentous objects such as neurons and blood vessels. We discuss these steps in more detail below, along with details of specialized software tools for each.

Image stitching

Cleared samples will exceed the field of view of most imaging systems. Therefore, imaging of the entire tissue requires the acquisition of multiple Z-stack 'tiles' that must be fused together by image stitching. During stitching, neighbouring tiles are translated horizontally and vertically until a best fit is found within overlapping regions of the tiles; it is therefore important to acquire each tile with an overlap of 5–10% with all neighbouring views. This approach serves to correct two common artefacts: the misalignment of objects that cross tile boundaries (caused by sample movement or non-perfect stage translation) and the inhomogeneity of signal intensity across the field of view[81,82]. Several software tools are available for stitching including the BigStitcher for Fiji/ImageJ[83], Arivis Vision4D and Imaris.

Correction of sample-induced artefacts

The two most common imaging artefacts associated with imaging cleared tissue are spherical and chromatic aberration. Spherical aberration occurs when light rays

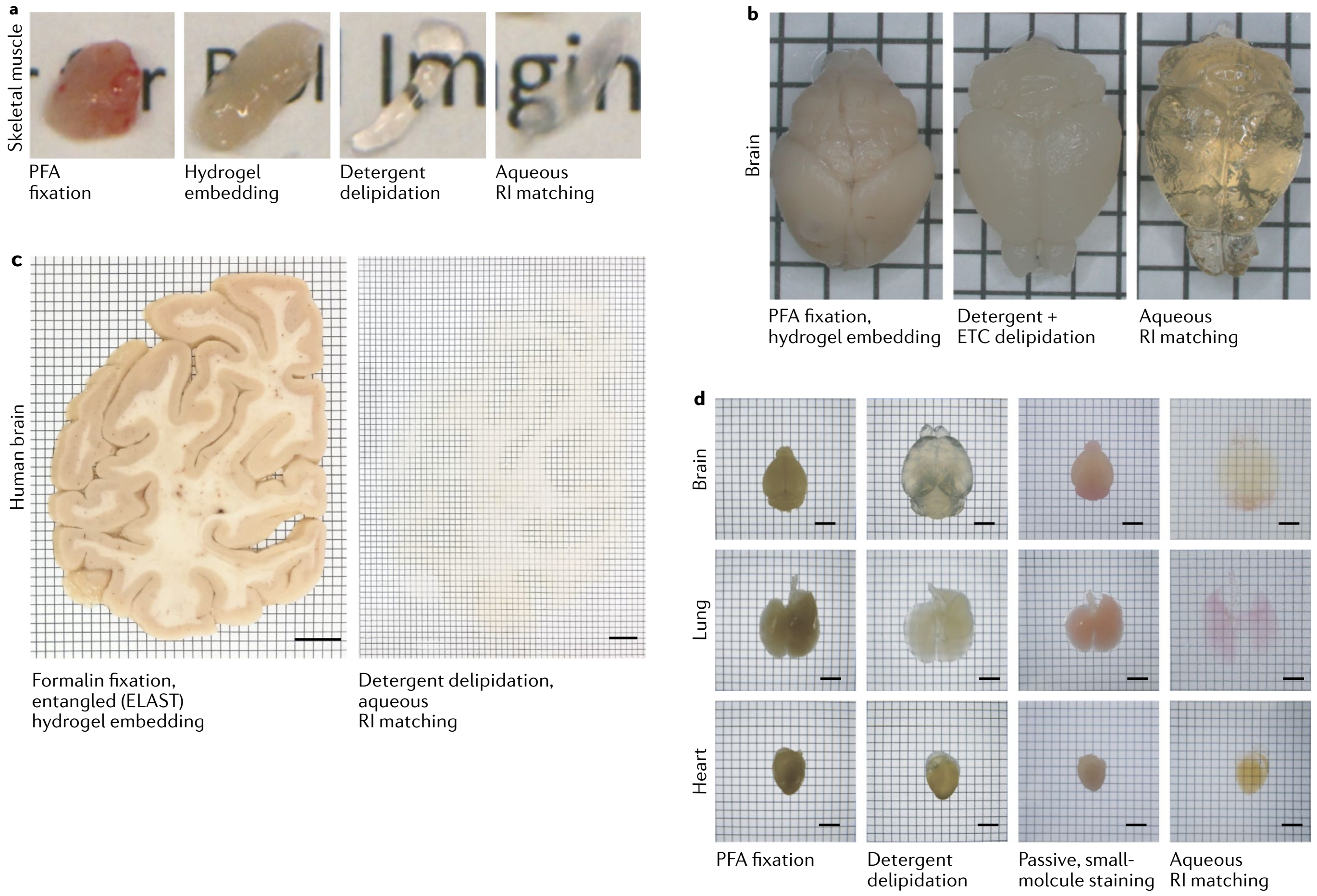

Fig. 5 | **Examples of the clearing process. a** | Four pieces of mouse skeletal muscle at various stages of the clearing process. From left to right: muscle extracted from the mouse and fixed in paraformaldehyde (PFA); muscle tissue extracted from a mouse that was transcardially perfused with phosphate-buffered saline (PBS) and hydrogel embedded; muscle tissue passively delipidated for 4 days in sodium dodecyl sulfate (SDS)–boric acid; muscle tissue that has been refractive index (RI) matched in an aqueous solution of RI 1.47. **b** | Mouse brains cleared using the CLARITY process. Left: hydrogel-embedded sample. Centre: sample that has been delipidated using active electrophoretic tissue clearing (ETC) for 24 h. Right: sample after RI matching in a 1.47 RI solution for 48 h. **c** | 2 mm-thick coronal human brain hemisphere slabs after formalin banking. Left: slab before clearing. Right: the same sample after ELAST tissue transformation and RI matching. Scale bars, 1 cm. **d** | Mouse whole-organ clearing using the CUBIC process and nuclear staining with propidium iodide. RI matching was performed using the CUBIC-R+ (N) protocol (RI 1.522). Scale bars, 5 mm.

Dispersion
A measure of the change in refractive index relative to the wavelength of light passing through a substance. If a substance has high dispersion, it means blue light and red light will refract differently when passing through it.

striking the outer portion of a spherical lens do not focus to the same point on the optical axis as the rays that enter at the centre of the lens. Spherical aberration in fluorescence microscopes manifests as a dim, blurry and axially compressed image. Chromatic aberration occurs if different wavelengths of light fail to focus at the same point of the optical axis. This is the result of light passing through a material with high dispersion and in a fluorescent image manifests as a shift of each colour channel — most obvious axially — relative to one another. Microscope objectives contain several lens elements that together reduce spherical and chromatic aberration; however, these lens elements are selected assuming that only immersion and mounting media with specified RI and dispersion values will be used (usually those of water, 80% glycerol or oil). If a clearing solution does not exactly match the RI and dispersion values specified in the objective's design, sample-induced spherical and chromatic aberrations are produced[76]. Spherical aberration can be avoided by using an objective specifically calibrated to the RI and dispersion of the clearing solution (see Objectives, above), fixing the objectives in place and translating the sample through the clearing solution, installing a dipping cap over the front lens of the detection objective or using software (available from certain microscope manufacturers or a recent tutorial for correcting spherical abberation[76]) to correct the axial distortion after acquisition. Chromatic aberration in the axial dimension can be corrected by identifying a fiducial marker (such as a broadband autofluorescent structure or a position where all fluorophores colocalize) and obtaining a short Z-stack from which the axial shift of this singular object can be calculated for each colour channel. Z-stacks for each colour channel can then be offset (confocal) or the beam of a light-sheet microscope can be shifted axially for each colour channel according to this calculation. Alternatively, channel registration software can be used to correct chromatic aberration after acquisition using a similar approach. If several fiducial markers can be identified, the program can automatically calculate the required axial shift and realign the dataset. Post-processing has the advantage of correcting for lateral chromatic aberrations as well. If the dataset does not contain easily identifiable objects, a tissue phantom comprised of agarose and a sparse concentration (1–30 per field of view) of 200 nm broadband fluorescent or gold beads submerged in the final RI-matching medium of choice can be used. The required channel offset is identified by imaging the phantom and then applied to the dataset set through the hardware or software methods described above. Fluorescent beads (such as TetraSpeck from ThermoFisher) are preferred; however, they are unstable in most solvents, necessitating the use of gold beads.

Filtering to improve contrast

Microscopy data are inherently noisy and this noise determines how successfully objects of interest can be segmented and analysed in automated routines. Therefore, some degree of filtering is often required before segmentation. Because cleared tissue datasets are large, it is important to select filtering techniques with the least computational burden. A simple median filter with a diameter (in pixels) set to the same size as the objects of interest in the dataset is often sufficient. Where a median filter is insufficient or the data were acquired with low-numerical aperture objectives via confocal microscopy or thick light sheets, deconvolution may be required to eliminate out-of-focus light and improve optical sectioning. Nearly all open source and commercial image analysis software packages offer these methods.

Segmentation of objects

Segmentation refers to the grouping of pixels or voxels from a dataset into objects. Once defined, these objects can be 3D rendered free of background noise or measured in numerous ways to obtain quantitative data. The simplest method for segmentation is to choose a single intensity threshold and count all pixels above that value as being part of one or more objects. Any pixels below this threshold are considered background. When applied to an entire image, this method is referred to as global thresholding and can be performed using the open source[9,46] and commercial software[45,84] packages described above to segment objects in cleared tissue volumes. The most common object segmented in cleared tissue is nuclei. In most tissues, nuclei are spaced far enough apart to permit highly accurate segmentation even when general nuclear stains that label all cells are used[7,22]. FIGURE 6 displays an example of single-cell counting in several different mouse organs, which were cleared with the CUBIC-R+ protocol and imaged by light-sheet microscopy; here, more than 75 million cells are identified in each organ by using a 3D Hessian-based difference of Gaussian algorithm[24]. The accuracy of nuclear segmentation can be further improved by labelling only a subset of cells, which can also produce biologically relevant insights when linked to a physiological read-out such as identification of active neurons (via Fos staining) after providing a stimulus to an animal[46]. Segmentation of individual cell bodies labelled with cytoplasm- or membrane-expressed fluorescent proteins is also possible if the fluorophore is sparsely expressed[17].

Global thresholding is difficult to perform in large cleared tissue as the SNR can vary dramatically from region to region within the sample, making selection of a single intensity volume that can accurately separate signal from noise impossible. In recent years, the application of machine learning-based algorithms to segment objects of interest in microscopy images has provided robust methodologies for cellular profiling[85]. At least two studies have shown that machine learning algorithms are superior to global thresholding when used to detect, segment and quantify cells in large cleared tissues[6,86].

Quality control for automated segmentation. It is impossible for a human to assess the accuracy of segmentation by eye throughout a whole dataset. However, it is possible to perform quality control on portions of a dataset to infer the overall accuracy. For example, a researcher could count sparse objects by eye within multiple, small, representative regions throughout the sample. The automated segmentation algorithm can then be run on

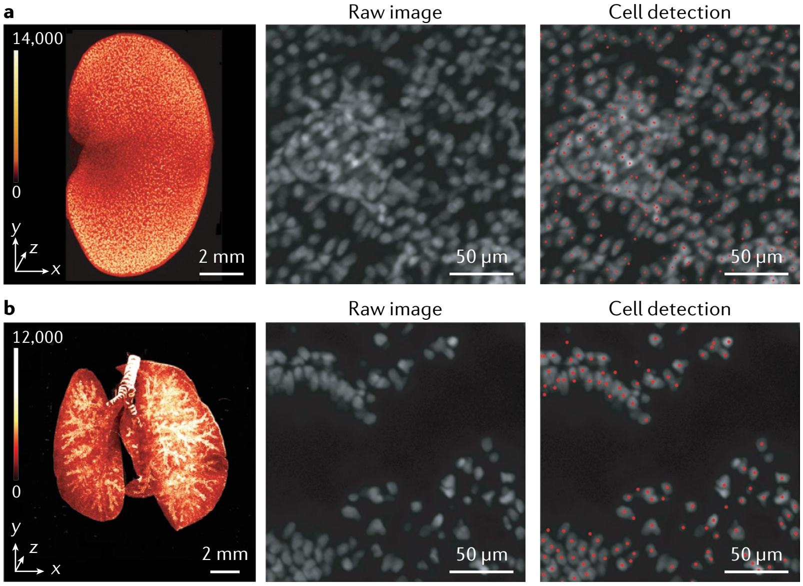

Fig. 6 | **Whole-organ cell profiling using the latest CUBIC-L/R+ protocol.** Volume-rendered and single-plane images of mouse organs of 8-week-old C57BL/6N male mice that were cleared using CUBIC-L/R+. The organs were stained with propidium iodide (PI) and individual cells were detected using a custom machine learning, GPU-based cell detection algorithm with >90% accuracy (see REF.[24]). **a** | Imaging of the mouse kidney identified 79–83 million cells. **b** | Imaging of the mouse lung identified 99.3 million cells.

the same regions and the results compared. Counting by eye quickly becomes impossible as objects become denser and ‘by hand’ segmentation can be used, where a researcher makes annotations on each object on sequential 2D planes by circling or painting with a mouse or pen that are then combined into 3D objects. Again, a series of smaller regions are annotated by hand, counted, and the results are compared with those obtained by automated segmentation. All open source and commercial software programs identified above have annotation functionality. Automated segmentation should be >90% accurate and preferably >95% accurate when compared with by-eye or by-hand methods.

When approaching machine learning for the first time, a researcher should determine whether pre-trained algorithms already exist for their structure of interest (for example, StarDist[87] for detecting nuclei). Owing to the unique labelling patterns of individual experiments, it is likely that such resources will not be available and in these cases, multiple user-friendly options exist for training machine learning algorithms using the annotate-by-hand approach described above, including Trainable Weka Segmentation (ImageJ/Fiji), ilastik, Intellisis (Zeiss), Vision4D (Arivis) and Aivia. When using these types of painting approach for training, it is important to paint the edges of objects so that the algorithm is trained using pixels at object boundaries. At least two objects, or classes, must be trained: ‘Object1’ and background. It should be noted that many of these software packages are not compatible with the large datasets obtained by imaging cleared tissue, and custom coding is often required. First, training data must be established by manual annotation, as described above,[86] or by creating synthetic training data that mimic the structural features to be imaged[88]. Enough training data must be produced so that a portion can be reserved to test the ability of the algorithm to achieve satisfactory results with data it has not seen previously. Secondly, a machine learning approach must be chosen. Random forests are the simplest approach and require the least computing power, although they are less flexible than complicated neural networks[89]. In this approach, the only parameter to set is the number of decision trees, with more decision trees improving the performance of the model but requiring additional computing power and processing time. Neural networks require in-depth understanding to correctly design their architecture including the number of layers, number of neurons in each layer, activation functions and initialization rates; therefore, an equal or greater number of hyperparameters must also be set for the training algorithm[85,90]. Therefore, customized neural networks should only be attempted by those with expertise in deep learning, and proper testing is essential. A good algorithm can correctly identify objects chosen at random from the training data with few false positives and few false negatives; that is, its precision (correct annotation rate among all the annotations it made) and its recall (correct annotation rate among all the elements in the dataset that should have been discovered) are high. Although the manual annotation step can be time consuming, it is a worthwhile investment. A well-established algorithm facilitates the 3D analysis of large specimens, leading to a better understanding of various biological and biomedical questions[86,88].

Quantitative measurements of segmented objects. Quantitative measurements performed in cleared tissue are similar to those performed in volumetric images of non-cleared tissue, although all measurements must be performed in three dimensions and the size of the dataset can cause an analysis routine to exceed the maximum capacity of many current image analysis software programs.

The least computationally complex and most-performed quantitation of 3D imaging data from cleared tissue is object counting. Once objects have been segmented (although this is not a requirement), they can easily be counted by scanning the dataset for areas of intensity maxima. Objects that are easily counted include nuclei[23,46] and sparsely labelled cell bodies[17]. Volume measurements are easily calculated if the x, y and z dimensions of a voxel are known, and this information is often contained in the metadata of the image file and automatically read by most image analysis software; the volume of an object can be calculated as the number of voxels in the object multiplied by the volume of the voxel. Several distance measurements can also be performed; for example, the centre of mass for each object can be identified and a region-growing technique — in which a virtual sphere is extended pixel by pixel until the sphere contacts the next nearest centre of mass — can be used to measure the distance between objects in a sample[91]. If two or more fluorescent labels are used, the region-growing technique can be specified to detect only objects in another channel, providing a read-out of the distance between different molecules of interest. In cleared tissue, colocalization measurements usually

Random forests
Machine learning algorithms that comprise many ‘estimators’ that each make a prediction as to which segmentation group a pixel should belong. When many estimators are combined into a ‘forest’, the final prediction is highly accurate.

Tortuosity
Describes the degree of curvature and/or twist in a blood vessel.

require segmentation of objects of interest in two or more channels, locating their centres of mass and setting a colocalization limit — the maximum distance that two centres of mass can be from one another and still be considered colocalized. This is usually set to 0.5–1× the diameter of the object[92]. Finally, filament tracing of blood vessels and neurons is a popular quantitative measure. Filament tracing often remains semi-automated and requires substantial user input to direct the propagation of these structures through poorly labelled or noisy regions of the image[93]. Once filaments have been segmented, several measurements can be performed, including length, volume, orientation, tortuosity and number of branch points. See the Applications section below for more detailed descriptions of common applications for each of these quantitative measurements.

Registration to tissue atlases

Atlases are 3D maps that are used to delineate different anatomical or functional regions of an organ. In complex organs, the boundaries between these regions require hundreds of labels to be visualized[94]. As incorporating these labels into an experiment is currently not achievable, determining the exact region of an organ in which a fluorescent signal resides requires the 3D dataset to be registered to an existing atlas[24,38,95–104]. Atlases are used extensively in the analysis of cleared tissue 3D datasets; for example, several studies have mapped data from multiple cleared brains onto the Franklin and Paxinos Atlas[17], the Waxholm Space Atlas[23,100] or the Allen Brain Atlas[46]. Open source software for performing these types of registration are available including ClearMap[46] and large deformation diffeomorphic metric mapping (LDDMM)[105–107]. When mapping data to an atlas there are two key considerations. First, the dataset must contain a fluorescence channel with a similar fluorescence intensity across the entire organ, most often a channel containing tissue autofluorescence or a general nuclear dye. Second, the resolution of the sample image must be similar to the resolution of the images in the atlas. A limitation of many established atlases is that their regional-level resolution, often developed using MRI or CT[108,109], is not sufficient for registering the cellular resolution of microscopy data. To address this, a single-cell resolution atlas was developed for the mouse brain (CUBIC-Atlas) along with a cloud-based framework to perform 3D analysis at single-cell resolution (CUBIC-Cloud)[104]. High-resolution reference atlases of entire organisms are needed to assist whole-body clearing methods. Currently, manual annotation[86] of individual organs is being replaced with deep learning-based organ segmentation[110]; this approach has potential to transform the analysis of whole-body scans, eventually leading to the generation of more accurate mouse body atlases.

Required computing specifications

High-end workstations are needed to perform the above analyses. For optimal performance, data must be rapidly accessible, ideally in a solid state drive (SSD); if SSDs are cost prohibitive, multiple hard disk drives (HDDs) in a RAID array can suffice. Large amounts of RAM (>200 GB) can reduce the need for disk access, which is usually an image analysis bottleneck. Finally, the amount of GPU memory and number of GPU processing cores are also important. For image analysis routines that can be GPU accelerated such as CLIJ[111], DeepMACT[86], TubeMap[112] and others, these specifications will determine how rapidly the processing can be completed. Additionally, GPU memory will determine the resolution limits when displaying 3D data. For example, when running a deep learning-based algorithm such as DeepMACT, a workstation with 64 GB RAM and a 12 GB Nvidia Titan XP GPU is capable of processing a series of whole-mouse images in 45 min (REF.[86]). Workstations equipped with 512 GB RAM and a 24 GB Nvidia Quadro P6000 GPU have been used to process the TubeMap algorithm[112].

Applications

Tissue clearing now provides a viable alternative to serial sectioning of large biological samples. In comparison with sectioning, tissue clearing is often a lengthier process owing to the requirement for incubation in various solutions and the additional time required for diffusion of labels; however, these incubations require very little hands-on time and no specialized skills. Clearing protocols that do not require specialized equipment allow a high degree of parallelization that cannot be achieved with a single vibratome or cryostat. Furthermore, tissue clearing avoids mechanical damage that can occur within the tissue during sectioning and the heavy computational burden of aligning, de-warping and assembling hundreds or even thousands of 2D images into a 3D rendering. Analysis of intact, cleared samples shows improved accuracy compared with quantitative stereology[113] and traditional 2D histopathology[114]. Finally, clearing allows for studies across entire organs (such as long-distance nerve tracing[17]) or entire organisms (such as identification of cancer metastasis[7,86]) that cannot be accomplished through serial sectioning.

Biologically, the applications of tissue clearing methods are wide-ranging. Tissue clearing has primarily shown use in the fields of neuroscience, oncology and cardiology, although nearly every organ and organ system in rodents has now been cleared, including the brain, intestine, spleen, lymph node, heart, kidney, lung, eye and bone[7,10,11,27,34,43–45,70,71,110]. Other model and non-model systems such as fish and salamanders have also been used[15,115,116]. The ever-increasing size of in vitro models such as spheroids and organoids — now many millimetres in size[117]— necessitates the use of tissue clearing to image them in their entirety. Finally, methods to clear living samples and enhance imaging depth for in vivo studies now show promise.

Applications in neuroscience

In many organisms, including mice and humans, neurons are the largest cells in the body with processes up to several centimetres long. Their large size requires that they be investigated in complete volumes spanning a whole organ or even organism, and for most animals tissue clearing or whole animal sectioning[118] is required (aside from in the most translucent aquatic creatures, as demonstrated in a recent preprint article[119]). Nervous system tissues are abundant in lipids and relatively

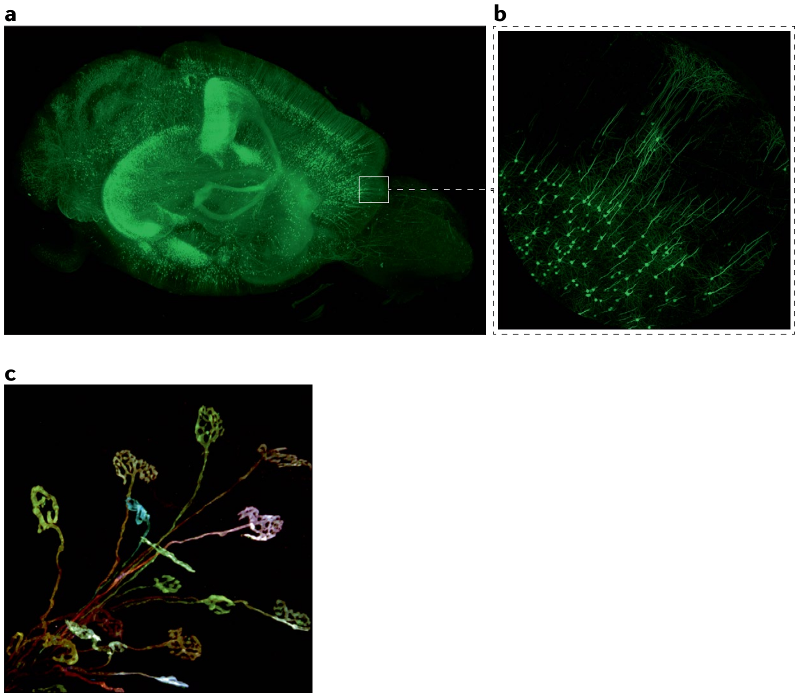

Fig. 7 | **Example of neuronal staining in the mouse brain. a** | 3D rendering of an entire mouse brain expressing GFP downstream of the *Thy1* promoter[122] in a subset of cells. The brain was cleared using a CLARITY protocol. Major fibre tracks are clearly visible. **b** | Zoomed cortical region of the brain shown in panel **a**. Individual neuronal processes can be visualized. **c** | Brainbow-expressing neuromuscular junctions in mouse skeletal muscle. Muscle was cleared using a passive hydrogel embedding method. Each neuron expresses a unique ratio of blue, green and red fluorophore, enabling the observation of individual neurons.

lacking in pigment and extracellular matrix proteins such as collagen and elastin, making them ideally suited to clearing, as once the lipid is removed, only a sparse protein matrix is left behind. Solvent-based and aqueous-based techniques have both[6,57] proved successful in clearing tissues of the nervous system; however, techniques that combine the two techniques may be best suited for regions of high lipid density such as the spinal cord and myelinated axon bundles in the brain.

A major goal in neuroscience is to dissect the complete wiring diagram of the brain, a field known as connectomics. Even after tissue clearing, the density of neurons remains beyond the resolution limit of fluorescence microscopes[120] and current practice is to create maps of inter-areal projections by sparsely labelling collections of neurons[121,122] (Fig. 7). Several techniques exist to sparsely label subsets of neurons throughout the brain, including genetically encoded fluorescent proteins under the control of a cell-type-specific promoter and immunolabelling with known markers of specific cell types. Expression of fluorescent proteins may involve a single fluorescent protein per cell type or use combinatorial expression of multiple fluorescent proteins to enable the identification of hundreds of individual cells (for example Brainbow[123,124] and other similar approaches). Transgenic animals can be produced that express fluorescent proteins or they can be expressed by infecting cells with a virus carrying DNA encoding a fluorescent protein. Rabies virus and adeno-associated virus (AAV) are commonly used for transducing cells of the nervous system; for example, a combination of AAV vectors were directly injected into the brains of mice to determine patterns of dopamine neuron innervation in the midbrain[17]. A less invasive approach is to use AAV vectors that can be injected into the bloodstream and infect specific cell types of the brain[18]. To aid in the analysis of sparsely labelled neurons in cleared tissue, volumetric neuronal tracing algorithms have been developed that can perform manual or semi-automated segmentation[93]. Most promising are new, fully automated algorithms such as NeuroGPS-Tree, which has traced more than 1,000 neurons in thick, cleared tissue sections[125], and a software package called BIRDS that uses deep learning to perform long-distance neuronal projection tracing and parallel counting of cell populations in different brain regions[126].

Tissue clearing has also been used to map areas of brain activity after an organism performs a behaviour or is administered a stimulus. Brain activity can be inferred by immunostaining for the protein products of immediate-early genes such as *fos*. If Fos is present in a neuron, this indicates that it was recently activated. Using this method, brain region activity mapping was accomplished in cleared mouse brain, harvested after sensory whisker stimulation or observed parenting behaviours in mice[46].

Finally, tissue clearing shows potential to aid in the investigation of neuronal pathologies. The SWITCH clearing and immunolabelling protocol was recently used to show that amyloid-β (Aβ) peptides that contribute to the onset and progression of Alzheimer dementia can be labelled and imaged in a brain-wide manner[127]. This methodology allowed microscopic mapping of Aβ plaques and identified several novel subcortical hubs where Aβ accumulates.

To date, tissue clearing of brains has primarily focused on rodent tissue as human tissue presents several barriers to tissue clearing, including enhanced autofluoresence, over-fixation from long-term preservation and large physical size. Recently, the SHANEL and ELAST tissue clearing protocols have been adapted to overcome many of these barriers and permit investigation of large brain slabs or even whole brain[6,31]. Numerous exciting applications exist in this domain and we refer readers to a recent review for further applications[3]. An example of whole-animal clearing and neuronal imaging is shown in Fig. 8.

Applications in oncology

Whole animal clearing using aqueous-based (CUBIC) or solvent-based (vDISCO) techniques has enabled the visualization of micrometastases throughout an entire rodent at single-cell resolution[7,86]. Additionally, by fluorescently labelling a therapeutic antibody, it is possible to detect the percentage of metastatic sites receiving treatment across the entire animal[86] (Fig. 8).

In the field of cancer pathology, there is interest in determining whether 3D samples can provide a more accurate diagnosis or prognosis than traditional 2D surgical sampling techniques. A form of expansion microscopy, termed ExPATH, suggested that imaging of cleared biopsy samples from patients with breast cancer was able to discriminate between early breast neoplastic lesions better than surgical sampling[114]. Large (30 × 20 × 5 mm) surgically resected breast tumours were cleared in less than 48h using the PathoDISCO solvent-based clearing technique[128]; in PathoDISCO the key step is using 2,2-dimethoxypropane to react with water to create acetone and methanol, which rapidly dehydrate the tissue.

The microenvironment that surrounds a tissue is highly heterogeneous and influences its growth and development[129]. Hydrogel embedding protocols have been shown to preserve important elements of the microenvironment that surrounds developing breast tissue and allow for its investigation in 3D[130]. In this manner, the CUBIC tissue clearing method revealed the role of TGFβ in the tumour microenvironment by profiling multicellular interactions in a mouse model of experimental lung metastasis.

Interestingly, studies investigating the administration of novel, non-lipid-based nanoparticles, which are being investigated as potential delivery vehicles for therapeutics, showed that both solvent-based[131] and aqueous-based[132,133] techniques allow for the retention of these nanoparticles in the tissue. These studies demonstrated that tissue clearing can be used for measuring the biodistribution of novel cancer therapeutics.

Applications in cardiovascular research

Blood vessels are easily labelled before clearing through the perfusion of labelling reagents. Multiple labels have been used, including antibodies that target molecules that line the vasculature[134], wheatgerm agglutinin and Evans blue[88], or lipophilic dyes[135]. It is important that any label contains a moiety that can react with fixatives such as PFA or else it will be washed away during subsequent clearing steps. FIGURE 9 displays several cleared tissues in which blood vessels have been stained. Tissue clearing allows for the study of vessel repair and remodelling during development or after injury in any organ throughout the body; of particular interest are studies of blood vessel rupture in the brain in the case of aneurysm and stroke, and infarctions of the heart[136]. Cardiovascular studies investigating blood vessel structure and function are now aided by several semi-automated vasculature segmentation techniques that have been developed in commercial[137] and custom[138] software to analyse regions of interest (ROIs) in cleared mouse brains. These methods are not sufficient to reliably detect capillaries with variable SNR in different brain regions or to systematically analyse the vascular alterations at the whole brain or organ level[88,112]. Machine learning-based strategies have overcome these hurdles and currently two machine learning-based methods (VesSAP[88] and TubeMap[112]) are available to reliably detect, segment and register images of whole brain vasculature to the Allen brain atlas. Recently, tissue clearing has been used to map the parasympathetic and sympathetic circuits that control heart rate in mice[139], produce a single-neuron-scale map of the intrinsic cardiac nervous system of the rat[140] and quantify sympathetic hyperinnervation of murine hearts after infarction[141].

Non-murine applications

Aquatic organisms. Genome modification technologies such as CRISPR have enabled biological investigation in species beyond traditional model systems. Clearing protocols must be adapted to each species as many express

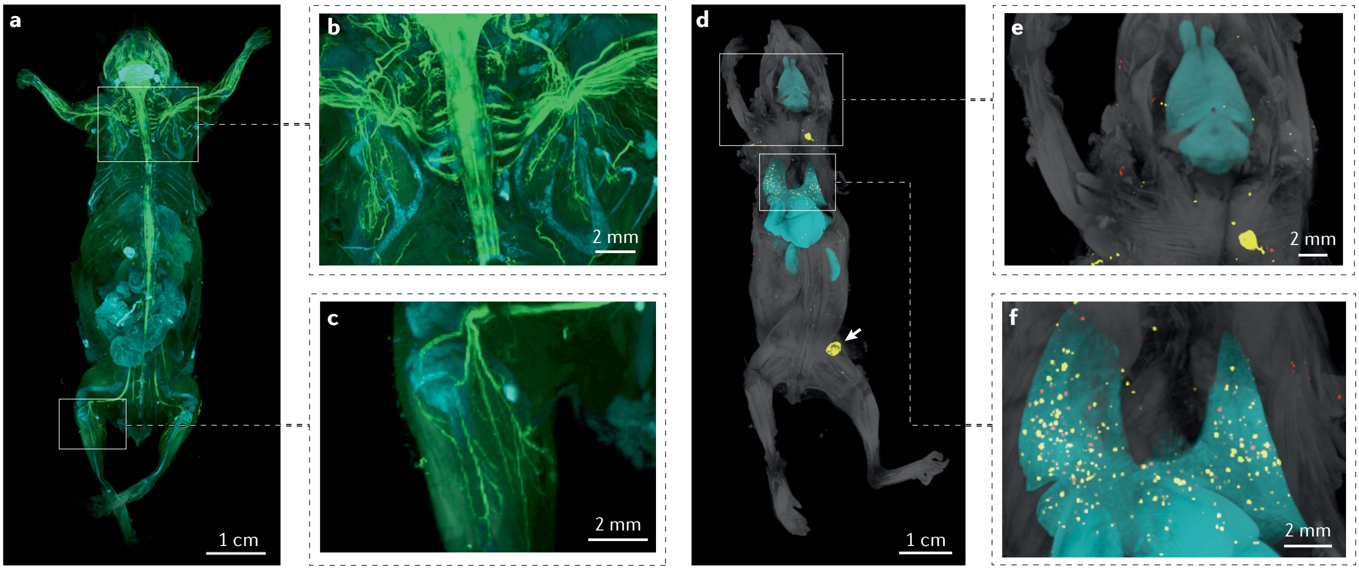

Fig. 8 | **Representative results of vDISCO panoptic imaging. a** | 3D rendering of a *Thy1*-GFP line M mouse after vDISCO whole-body immunolabelling/clearing and imaging by light-sheet microscopy. Neuronal fibres expressing GFP are enhanced by anti-GFP nanobodies conjugated with Atto647 dye and shown in green, bones and internal organs highlighted by propidium iodide are in cyan and the background signal — mainly from autofluorescence of the muscle tissue — is in white. **b**,**c** | Zoomed-in images of the boxed regions in panel **a**, showing detailed neuronal structures with subcellular level resolution. **d** | 3D reconstruction of a vDISCO-processed NSG mouse implanted with MDA-231 human breast cancer cells in the mammary fat pad for approximately 2 months, followed by intravenous injection of an anti-human CA12 therapeutic antibody named 6A10, which is conjugated with Alexa-568 dye. The cancer cells were previously transduced by mCherry viral vectors and further enhanced by anti-mCherry nanobodies conjugated with Atto647 dye. The 6A10-targeted primary tumour (indicated by the white arrow) and metastases are shown in yellow, untargeted metastases are in red and selected organs including the brain, lungs, liver and kidneys are manually segmented and shown in cyan. **e**,**f** | Enlarged view of the boxed regions in panel **d** showing greater detail of the distribution of micrometastases and targeting efficacy of the 6A10 therapeutic antibody.

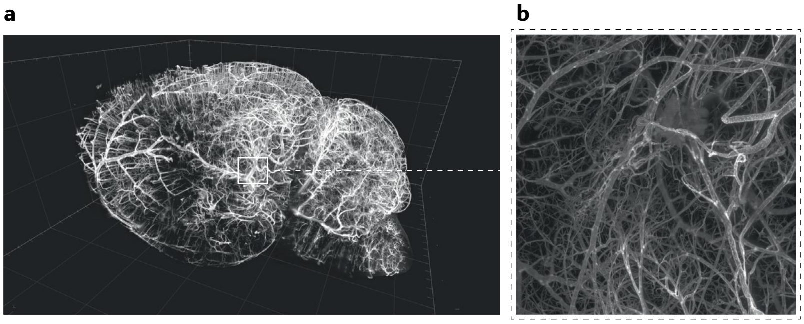

Fig. 9 | **Example of vascular staining in the mouse brain. a** | 3D render of an entire mouse brain that was perfused with CM-Dil lipophilic dye before fixation. After fixation, the brain was cleared using a modified iDISCO protocol and imaged via light-sheet microscopy. **b** | Zoomed region of brain from panel **a** showing the level of detail in vasculature staining.

unique pigments throughout their tissues that aid in protecting them from dangerous UV radiation (such as protection of the haematopoietic niche by melanin in fish)[142]. Many pigments such as melanin, ommochromes and pterins are resistant to hydrogen peroxide bleaching and do not elute with haem in amino alcohols. The DEEP-Clear method has shown that combining hydrogen peroxide, THEED and acetone can bleach or remove most of the pigments from annelids, molluscs, bony fish and tetrapods[15]. Others have shown that the addition of decalcification and bleaching steps renders crustaceans clear and may enable the creation of developmental atlases with single-cell resolution[116]. Finally, an enzymatic treatment with collagenase was added to a customized tissue clearing protocol for flatfish to show that thyroid hormone is involved in their eye migration during metamorphosis[115].

Plants. The plant wall imposes an additional RI mismatch that is not present in mammalian tissue and must be addressed. Additionally, chloroplasts act as a pigment, absorbing blue and red light, and generate fluorescence during imaging, which may or may not be desired depending on the experiment. Plant tissue has historically been cleared using a single solution of sodium hydroxide and chloral hydrate that breaks down cell walls and equilibrates the RI throughout the sample[143]. Urea[144], xylitol powder and sodium deoxycholate[145] and NaClO[146] have been used as less toxic alternatives to chloral hydrate. Interestingly, the general principle of RI matching has even been used to create transparent wood with the potential to replace glass as a building material[147].

Humans. 3D imaging of clinical samples could have additional diagnostic potential over 2D histopathology investigations[148]; however, imaging these samples is difficult owing to over-fixation, high levels of autofluorescence, the need for exogenous fluorescent labels and the overall high density of tissue from older patients. For very dense tissue, images of routine, thin, pathology tissue sections can be improved via expansion microscopy[114]. For larger samples — including intact human organs — the use of relatively small detergent (CHAPS) and solvent molecules for delipidation are needed to overcome the density of human tissue[6]. Elasticizing human tissue has been shown to improve probe delivery when the tissue is stretched, while simultaneously providing better preservation over time to allow for multiple rounds of labelling[31]. Conversely, human embryonic and fetal tissue is less dense and far easier to clear. Solvent-based clearing methods have been used to clear human embryos and fetuses from gestational weeks 6–14 (REF.[149]).

In vitro applications

Tissue clearing protocols have become essential for imaging spheroids and organoids in their entirety, as traditional light microscopy approaches cannot image more than 100–200 µm beyond their surface. Even the smallest organoids (on the scale of 50–100 µm) can benefit from simple RI matching. Human airway, colon, kidney, liver and breast tumour, and mouse mammary gland organoids of this size have been cleared with simple RI matching in high-concentration sugar solutions[150]. More complex tissue clearing methods are needed for larger and denser organoids such as 3D neuronal spheres (200–300 µm diameter)[151] and retinal organoids[152]. Finally, for organoids many millimetres in diameter, the SCOUT protocol has been used to clear, label, image and correlate hundreds of phenotypes between control and experimentally treated organoids[117]. SCOUT was able to identify several effects of Zika virus infection on cerebral organoids approximately 2 mm in diameter at the single-cell level[117].

In vivo and label-free applications

The modular tissue clearing methodologies described in this Primer are targeted towards fixed, non-living tissues stained with fluorescent labels. Although not the focus of this article, researchers have demonstrated clearing strategies that increase the imaging depth for several optical technologies in in vivo samples, including single-photon and multi-photon fluorescence, second harmonic generation (SHG) and optical coherence tomography (OCT) (reviewed in REF.[153]). To date, in vivo methods have primarily focused on the topical application of biocompatible high-RI solutions to the skin[154–158], skull[159] and superficial tumours[160,161] to provide increased imaging depth in both animal and human systems. As fluorescent labelling of live human tissue can be difficult owing to the inability to use genetic modification, human samples are often imaged by label-free techniques such as SHG and OCT. The ability to perform deep, label-free imaging in vivo is intriguing as it may hold clinical potential for the diagnosis and understanding of certain pathologies such as tumour biology.

Applications for systems biology

Systems biology generally entails analysis of hundreds to thousands of targets within a tissue. Often, labelling is the limiting step as it requires substantial time and, although studies exist in which tens of organs[17] have been imaged, it is more practical to perform systems-level investigations on smaller samples. Tissue clearing can be used on this smaller scale; for example, spatial transcriptomic techniques such as MER-FISH and seqFISH use imaging to detect thousands of mRNA species in a sample[162,163], and tissue clearing has been adopted with these techniques to enable 3D spatial transcriptomics. Incorporation of tissue clearing with the MER-FISH technique allowed a read-out of the positions of thousands of mRNA molecules in each cell of a tissue sample in 3D[164].

Reproducibility and data deposition

The reliability and reproducibility of tissue clearing protocols have dramatically improved in recent years. Solvent-based clearing methods now generally use chemical components that are affordable and effective. Aqueous-based techniques have been aided by commercially available equipment for hydrogel polymerization and ETC. Furthermore, the availability of commercial preformulated clearing solutions has allowed standardization of clearing protocols between research groups.

Fluorescent labelling in tissue clearing experiments still primarily relies on antibodies. Commercially available antibodies are prone to reproducibility issues caused by batch-to-batch variation, which are more apparent (specifically background caused by off-target binding) when labelling large tissues. Antibodies should be carefully selected on the basis of past results and validated on thin, uncleared tissue sections. An online repository for tissue clearing-validated antibodies can also be used.

Many journals and funding bodies encourage the deposition of raw data in publicly accessible searchable databases. Recently, imaging data repositories such as the Image Data Resource and the Cell Image Library have been made available[165] and authors are encouraged to deposit their raw data in a publicly accessible database if possible. In addition to raw images, essential metadata should be reported to ensure reproducibility and set expectations for a researcher who would like to replicate a tissue clearing experiment (BOX 1).

Studies that involve clearing tens or hundreds of samples may produce hundreds of terabytes or even petabytes of data, and public image repositories are limited in the amount of data they can store. Additionally, available bandwidth and a researcher's proximity to the repository's server can prevent uploads from occurring in a reasonable amount of time. Powerful lossy and non-lossy compression algorithms such as JPEG XS, AVIF and WebP can reduce data size with little reduction in image quality; these provide better quality and compression than using .jpeg or .png files.

Box 1 | **Suggested metadata to report when preparing and imaging cleared tissue**

- Approximate dimensions of the sample being cleared
- Composition of all clearing solutions used, duration of incubation in each solution and the purpose and function of each solution
- Degree of expansion or contraction of the sample
- Antibody manufacturer, lot number, concentration, incubation temperature and incubation duration
- Imaging modality used
- Numerical aperture of imaging objective
- Light-sheet thickness (if used)
- Voxel size of raw images
- Total raw data size
- A summary of all data processing steps (spherical aberration correction, chromatic aberration correction, filtering)
- Description of data quantitation methods
- Deposition of any custom software in an open source depository
- A subset of manually annotated ground-truth data to assess accuracy of automated data quantitation

Limitations and optimizations

There are some outstanding limitations of clearing techniques. First, the methods described in this Primer are most often applied to fixed tissue, as in vivo applications of tissue clearing are still limited[153]. Second, several factors restrict the throughput of tissue clearing experiments such as the limited sample capacity in tissue clearing equipment, high cost of antibodies and clearing solutions, the long time required for immunolabelling, lack of common conditions for antibody binding, sample capacity limitations in imaging devices and limitations in the IT infrastructure for data storage and analysis. Although one could imagine developing an automated pipeline for clearing, labelling and imaging, this would require an extensive investment in parallel equipment for sample preparation and imaging. Third, imaging of large samples requires microscope objectives with equally large working distances. Most imaging systems designed for cleared samples use moderate-numerical aperture, low magnification, long working distance objectives from zoom microscopes. In general, increasing the working distance of an objective decreases its numerical aperture and therefore its achievable resolution[81]. The goal of tissue clearing experiments is primarily to survey a large tissue or organ; however, if subcellular resolution is also required, secondary imaging of select areas may be better suited to a second, higher resolution imaging device. Finally, the maximum size of samples that can be cleared now exceeds the maximum sample size able to fit under a microscope[6,113]. Before investigation of human organs can be fully realized, imaging devices able to accommodate samples of this size must be developed. It is important to note that every tissue is different and researchers should not automatically follow a previously published method; for example, protocols that clear tissue with high lipid content such as brain are not optimal for pigmented, protein-rich kidney tissue. By viewing tissue clearing protocols as modular, a researcher can select and assemble an optimal pipeline for clearing their tissue of interest.

Outlook

The past decade has seen dramatic innovations in tissue clearing methods. Clearing solutions are no longer discovered serendipitously; researchers with extensive knowledge of optical physics, chemistry and tissue engineering are designing tailored solutions that improve on past methods. A decade ago, tissue clearing techniques were complex, unreliable and each had obvious limitations. Now, through incremental improvements, both aqueous and solvent-based techniques are able to preserve emission from fluorescent proteins and dyes and their final clearing solutions have coalesced around an ideal RI of 1.52–1.56. Commercially manufactured systems for steps such as hydrogel polymerization and electrophoretic tissue clearing and labelling are now available from multiple manufacturers, as are microscopes and objectives that have been designed specifically for cleared tissue.

Barriers do remain despite the positive outlook. The use of genetically encoded fluorescent proteins is not always possible, and immunolabelling techniques must still be used in many systems. No matter how quickly antibodies are delivered to their target, if the antibody is not specific or stable, the result will be a failed experiment. Furthermore, the current variability in ideal labelling conditions between individual antibodies makes it unlikely that a researcher's unique panel of probes will all function under identical conditions. We hope that nanobodies will be able to solve the many variability and stability issues of antibodies, although they are not without limitations. First, the random attachment of a fluorophore to a nanobody can block its binding site, necessitating directed attachment of the fluorophore with genetically encoded click chemistry[166,167]. Second, fewer fluorophores can be attached to a nanobody than to an antibody owing to its small size, providing a weaker signal. Third, nanobodies are primarily monoclonal and can be directly conjugated to a fluorescent dye. Therefore, polyclonal secondary antibodies that normally produce substantial fluorescent signal amplification are not used. Amplification strategies that are widely used in the single-molecule-RNA FISH field such as SABER[168] and HCR[169] could be adopted for nanobodies (as they have been for antibodies[170]) to alleviate the above limitations. Single-chain variable fragments (scFvs) — small immunolabels known to penetrate more quickly through biological tissue than nanobodies — have seen little application in tissue clearing to date but may be a promising technology for labelling large samples[171].

As tissue clearing experiments become commonplace, deep biological insight will follow. It is difficult to imagine a field of biology that will not benefit from the ability to investigate the 3D relationships between all components of a tissue. The recent clearing of entire rhesus monkey[172] and human[6] brains has shown that clearing methods are outpacing imaging technology. Laboratories looking to image on this scale will need to partner with industry to design and build objectives and optical systems with working distances of tens of centimetres that can still achieve reasonable lateral and axial resolution. There can be no doubt that the democratization of tissue clearing has begun, and exciting biological insights are sure to follow.

1. Richardson, D. S. & Lichtman, J. W. Clarifying tissue clearing. *Cell* **162**, 246–257 (2015).
2. Tainaka, K., Kuno, A., Kubota, S. I., Murakami, T. & Ueda, H. R. Chemical principles in tissue clearing and staining protocols for whole-body cell profiling. *Annu. Rev. Cell Dev. Biol.* **32**, 713–741 (2016).
3. Ueda, H. R. et al. Tissue clearing and its applications in neuroscience. *Nat. Rev. Neurosci.* **21**, 61–79 (2020).
4. Park, Y.-G. et al. Protection of tissue physicochemical properties using polyfunctional crosslinkers. *Nat. Biotechnol*. https://doi.org/10.1038/nbt.4281 (2018).
5. Susaki, E. A. et al. Versatile whole-organ/body staining and imaging based on electrolyte-gel properties of biological tissues. *Nat. Commun.* **11**, 1982 (2020).
6. Zhao, S. et al. Cellular and molecular probing of intact human organs. *Cell* **180**, 796–812.e719 (2020).
7. Kubota, S. I. et al. Whole-body profiling of cancer metastasis with single-cell resolution. *Cell Rep.* **20**, 236–250 (2017).
8. Lee, E. et al. ACT-PRESTO: rapid and consistent tissue clearing and labeling method for 3-dimensional (3D) imaging. *Sci. Rep.* **6**, 18631 (2016).
9. Pan, C. et al. Shrinkage-mediated imaging of entire organs and organisms using uDISCO. *Nat. Methods* **13**, 859–867 (2016).
10. Susaki, E. A. & Ueda, H. R. Whole-body and whole-organ clearing and imaging techniques with single-cell resolution: toward organism-level systems biology in mammals. *Cell Chem. Biol.* **23**, 137–157 (2016).
11. Tainaka, K. et al. Whole-body imaging with single-cell resolution by tissue decolorization. *Cell* **159**, 911–924 (2014).
12. Messal, H. A. et al. Antigen retrieval and clearing for whole-organ immunofluorescence by FLASH. *Nat. Protoc.* **16**, 239–262 (2021).
13. Pende, M. et al. High-resolution ultramicroscopy of the developing and adult nervous system in optically cleared Drosophila melanogaster. *Nat. Commun.* **9**, 4731 (2018).
14. Lindsey, B. W., Douek, A. M., Loosli, F. & Kaslin, J. A whole brain staining, embedding, and clearing pipeline for adult zebrafish to visualize cell proliferation and morphology in 3-dimensions. *Front. Neurosci.* **11**, 750 (2017).
15. Pende, M. et al. A versatile depigmentation, clearing, and labeling method for exploring nervous system diversity. *Sci. Adv.* **6**, eaba0365 (2020).
16. Deverman, B. E. et al. Cre-dependent selection yields AAV variants for widespread gene transfer to the adult brain. *Nat. Biotechnol.* **34**, 204–209 (2016).
17. Menegas, W. et al. Dopamine neurons projecting to the posterior striatum form an anatomically distinct subclass. *eLife* **4**, e10032 (2015).
18. Ravindra Kumar, S. et al. Multiplexed Cre-dependent selection yields systemic AAVs for targeting distinct brain cell types. *Nat. Methods* **17**, 541–550 (2020).
19. Hopwood, D. The reactions between formaldehyde, glutaraldehyde and osmium tetroxide, and their fixation effects o bovine serum albumin and on tissue blocks. *Histochemie* **24**, 50–64 (1970).
20. Murray, E. et al. Simple, scalable proteomic imaging for high-dimensional profiling of intact systems. *Cell* **163**, 1500–1514 (2015).
21. Collins, J. S. & Goldsmith, T. H. Spectral properties of fluorescence induced by glutaraldehyde fixation. *J. Histochem. Cytochem.* **29**, 411–414 (1981).
22. Ueda, H. R. et al. Whole-brain profiling of cells and circuits in mammals by tissue clearing and light-sheet microscopy. *Neuron* **106**, 369–387 (2020).
23. Susaki, E. A. et al. Whole-brain imaging with single-cell resolution using chemical cocktails and computational analysis. *Cell* **157**, 726–739 (2014).
24. Matsumoto, K. et al. Advanced CUBIC tissue clearing for whole-organ cell profiling. *Nat. Protoc.* **14**, 3506–3537 (2019).
25. Tainaka, K. et al. Chemical landscape for tissue clearing based on hydrophilic reagents. *Cell Rep.* **24**, 2196–2210 (2018).
26. Kim, S.-Y. & Assawachananont, J. A new method to visualize the intact subretina from retinal pigment epithelium to retinal tissue in whole mount of pigmented mouse eyes. *Transl. Vis. Sci. Technol.* **5**, 6 (2016).
27. Futami, K., Furukawa, O., Maita, M. & Katagiri, T. Application of hydrogen peroxide-melanin bleaching and fluorescent nuclear staining for whole-body clearing and imaging in fish. *Fish. Pathol.* **54**, 101–103 (2020).
28. Kuroda, M. & Kuroda, S. Whole-body clearing of beetles by successive treatment with hydrogen peroxide and CUBIC reagents. *Entomol. Sci.* **23**, 311–315 (2020).
29. Henning, Y., Osadnik, C. & Malkemper, E. P. EyeCi: optical clearing and imaging of immunolabeled mouse eyes using light-sheet fluorescence microscopy. *Exp. Eye Res.* **180**, 137–145 (2019).
30. Duong, H. & Han, M. A multispectral LED array for the reduction of background autofluorescence in brain tissue. *J. Neurosci. Methods* **220**, 46–54 (2013).
31. Ku, T. et al. Elasticizing tissues for reversible shape transformation and accelerated molecular labeling. *Nat. Methods* **17**, 609–613 (2020).
32. Choi, S. W., Guan, W. & Chung, K. Basic principles of hydrogel-based tissue transformation technologies and their applications. *Cell* **184**, 4115–4136 (2021).
33. Chung, K. et al. Structural and molecular interrogation of intact biological systems. *Nature* **497**, 332–337 (2013).
34. Yang, B. et al. Single-cell phenotyping within transparent intact tissue through whole-body clearing. *Cell* **158**, 945–958 (2014).
35. Chen, F., Tillberg, P. W. & Boyden, E. S. Optical imaging. expansion microscopy. *Science* **347**, 543–548 (2015).
36. Tillberg, P. W. et al. Protein-retention expansion microscopy of cells and tissues labeled using standard fluorescent proteins and antibodies. *Nat. Biotechnol.* **34**, 987–992 (2016).
37. Ku, T. et al. Multiplexed and scalable super-resolution imaging of three-dimensional protein localization in size-adjustable tissues. *Nat. Biotechnol.* **34**, 973–981 (2016).
38. Murakami, T. C. et al. A three-dimensional single-cell-resolution whole-brain atlas using CUBIC-X expansion microscopy and tissue clearing. *Nat. Neurosci.* **21**, 625–637 (2018).
39. Chang, J. B. et al. Iterative expansion microscopy. *Nat. Methods* **14**, 593–599 (2017).
40. Park, H. E. et al. Scalable and isotropic expansion of tissues with simply tunable expansion ratio. *Adv. Sci.* **6**, 1901673 (2019).
41. Kiviranta, I., Tammi, M., Lappalainen, R., Kuusela, T. & Helminen, H. J. The rate of calcium extraction during EDTA decalcification from thin bone slices as assessed with atomic absorption spectrophotometry. *Histochemistry* **68**, 119–127 (1980).
42. Jing, D. et al. Tissue clearing of both hard and soft tissue organs with the PEGASOS method. *Cell Res.* **28**, 803–818 (2018).
43. Treweek, J. B. et al. Whole-body tissue stabilization and selective extractions via tissue-hydrogel hybrids for high-resolution intact circuit mapping and phenotyping. *Nat. Protoc.* **10**, 1860–1896 (2015).
44. Greenbaum, A. et al. Bone CLARITY: clearing, imaging, and computational analysis of osteoprogenitors within intact bone marrow. *Sci. Transl. Med.* **9**, eaah6518 (2017).

45. Cai, R. et al. Panoptic imaging of transparent mice reveals whole-body neuronal projections and skull–meninges connections. *Nat. Neurosci.* **22**, 317–327 (2019).
46. Renier, N. et al. Mapping of brain activity by automated volume analysis of immediate early genes. *Cell* **165**, 1789–1802 (2016).
47. Renier, N. et al. iDISCO: a simple, rapid method to immunolabel large tissue samples for volume imaging. *Cell* **159**, 896–910 (2014).
48. Dodt, H. U. et al. Ultramicroscopy: three-dimensional visualization of neuronal networks in the whole mouse brain. *Nat. Methods* **4**, 331–336 (2007).
49. Qi, Y. et al. FDISCO: advanced solvent-based clearing method for imaging whole organs. *Sci. Adv.* **5**, eaau8355 (2019).
50. Hahn, C. et al. High-resolution imaging of fluorescent whole mouse brains using stabilised organic media (sDISCO). *J. Biophotonics* **12**, e201800368 (2019).
51. Schwarz, M. K. et al. Fluorescent-protein stabilization and high-resolution imaging of cleared, intact mouse brains. *PLoS ONE* **10**, e0124650 (2015).
52. Li, Y., Xu, J., Wan, P., Yu, T. & Zhu, D. Optimization of GFP fluorescence preservation by a modified uDISCO clearing protocol. *Front. Neuroanat.* **12**, 67 (2018).
53. Becker, K., Jahrling, N., Saghafi, S., Weiler, R. & Dodt, H. U. Chemical clearing and dehydration of GFP expressing mouse brains. *PLoS ONE* **7**, e33916 (2012).
54. Erturk, A. et al. Three-dimensional imaging of solvent-cleared organs using 3DISCO. *Nat. Protoc.* **7**, 1983–1995 (2012).
55. Hama, H. et al. ScaleS: an optical clearing palette for biological imaging. *Nat. Neurosci.* **18**, 1518–1529 (2015).
56. Chen, L. et al. UbasM: An effective balanced optical clearing method for intact biomedical imaging. *Sci. Rep.* **7**, 12218 (2017).
57. Chi, J. et al. Three-dimensional adipose tissue imaging reveals regional variation in beige fat biogenesis and PRDM16-dependent sympathetic neurite density. *Cell Metab.* **27**, 226–236 (2018).
58. Kim, S. Y. et al. Stochastic electrotransport selectively enhances the transport of highly electromobile molecules. *Proc. Natl Acad. Sci. USA* **112**, E6274–E6283 (2015).
59. Hoelzel, C. A. & Zhang, X. Visualizing and manipulating biological processes by using halotag and SNAP-tag technologies. *ChemBioChem* **21**, 1935–1946 (2020).
60. Fang, T. et al. Nanobody immunostaining for correlated light and electron microscopy with preservation of ultrastructure. *Nat. Methods* **15**, 1029–1032 (2018).
61. Burry, R. W. *Immunocytochemistry: A Practical Guide for Biomedical Research* (Springer, 2010).
62. Sahl, S. J., Hell, S. W. & Jakobs, S. Fluorescence nanoscopy in cell biology. *Nat. Rev. Mol. Cell Biol.* **18**, 685–701 (2017).
63. Muyldermans, S. Nanobodies: natural single-domain antibodies. *Annu. Rev. Biochem.* **82**, 775–797 (2013).
64. Lai, H. M. et al. Next generation histology methods for three-dimensional imaging of fresh and archival human brain tissues. *Nat. Commun.* **9**, 1066 (2018).
65. Gleave, J. A., Lerch, J. P., Henkelman, R. M. & Nieman, B. J. A method for 3D immunostaining and optical imaging of the mouse brain demonstrated in neural progenitor cells. *PLoS ONE* **8**, e72039 (2013).
66. Kumar, V. et al. Global lymphoid tissue remodeling during a viral infection is orchestrated by a B cell–lymphotoxin-dependent pathway. *Blood* **115**, 4725–4733 (2010).
67. Sillitoe, R. V. & Hawkes, R. Whole-mount immunohistochemistry: a high-throughput screen for patterning defects in the mouse cerebellum. *J. Histochem. Cytochem.* **50**, 235–244 (2002).
68. Na, M., Kim, K., Lim, H. R., Ha, C. M. & Chang, S. Rapid immunostaining method for three-dimensional volume imaging of biological tissues by magnetic force-induced focusing of the electric field. *Brain Struct. Funct.* **226**, 297–309 (2021).
69. Dwyer, J., Ramirez, M. D., Katz, P. S., Karlstrom, R. O. & Bergan, J. Accelerated clearing and molecular labeling of biological tissues using magnetohydrodynamic force. *Sci. Rep.* **11**, 16462 (2021).
70. Takahashi, K., Kubota, S. I., Ehata, S., Ueda, H. R. & Miyazono, K. Protocol for imaging and analysis of mouse tumor models with CUBIC tissue clearing. *STAR. Protoc.* **1**, 100191 (2020).
71. Li, W., Germain, R. N. & Gerner, M. Y. Multiplex, quantitative cellular analysis in large tissue volumes with clearing-enhanced 3D microscopy (Ce3D). *Proc. Natl Acad. Sci. USA* **114**, E7321–E7330 (2017).
72. Klingberg, A. et al. Fully automated evaluation of total glomerular number and capillary tuft size in nephritic kidneys using lightsheet microscopy. *J. Am. Soc. Nephrol.* **28**, 452–459 (2017).
73. Aoyagi, Y., Kawakami, R., Osanai, H., Hibi, T. & Nemoto, T. A rapid optical clearing protocol using 2,2′-thiodiethanol for microscopic observation of fixed mouse brain. *PLoS ONE* **10**, e0116280 (2015).
74. Costantini, I. et al. A versatile clearing agent for multi-modal brain imaging. *Sci. Rep.* **5**, 9808 (2015).
75. Staudt, T., Lang, M. C., Medda, R., Engelhardt, J. & Hell, S. W. 2,2′-Thiodiethanol: a new water soluble mounting medium for high resolution optical microscopy. *Microscopy Res. Tech.* **70**, 1–9 (2007).
76. Diel, E. E., Lichtman, J. W. & Richardson, D. S. Tutorial: avoiding and correcting sample-induced spherical aberration artifacts in 3D fluorescence microscopy. *Nat. Protoc.* **15**, 2773–2784 (2020).
77. Vallejo Ramirez, P. P. et al. OptiJ: open-source optical projection tomography of large organ samples. *Sci. Rep.* **9**, 15693 (2019).
78. Mayer, J. et al. OPTiSPIM: integrating optical projection tomography in light sheet microscopy extends specimen characterization to nonfluorescent contrasts. *Opt. Lett.* **39**, 1053–1056 (2014).
79. Baek, K. et al. Quantitative assessment of regional variation in tissue clearing efficiency using optical coherence tomography (OCT) and magnetic resonance imaging (MRI): a feasibility study. *Sci. Rep.* **9**, 2923 (2019).
80. Pietzsch, T., Saalfeld, S., Preibisch, S. & Tomancak, P. BigDataViewer: visualization and processing for large image data sets. *Nat. Methods* **12**, 481–483 (2015).
81. Jonkman, J., Brown, C. M., Wright, G. D., Anderson, K. I. & North, A. J. Tutorial: guidance for quantitative confocal microscopy. *Nat. Protoc.* **15**, 1585–1611 (2020).
82. Jost, A. P. & Waters, J. C. Designing a rigorous microscopy experiment: validating methods and avoiding bias. *J. Cell Biol.* **218**, 1452–1466 (2019).
83. Horl, D. et al. BigStitcher: reconstructing high-resolution image datasets of cleared and expanded samples. *Nat. Methods* **16**, 870–874 (2019).
84. Prahst, C. et al. Mouse retinal cell behaviour in space and time using light sheet fluorescence microscopy. *eLife* **9**, e49779 (2020).
85. Moen, E. et al. Deep learning for cellular image analysis. *Nat. Methods* **16**, 1233–1246 (2019).
86. Pan, C. et al. Deep learning reveals cancer metastasis and therapeutic antibody targeting in the entire body. *Cell* **179**, 1661–1676 (2019).
87. Schmidt, U., Weigert, M., Broaddus, C. & Myers, G. in *Medical Image Computing and Computer Assisted Intervention – MICCAI 2018* (eds Frangi, A. F., Schnabel, J. A., Davatzikos, C., Alberola-López, C. & Fichtinger, G.) 265–273 (Springer, 2018).
88. Todorov, M. I. et al. Machine learning analysis of whole mouse brain vasculature. *Nat. Methods* **17**, 442–449 (2020).
89. Qi, Y. in *Ensemble Machine Learning: Methods and Applications* (eds Zhang, C. & Ma, Y.) 307–323 (Springer, 2012).
90. Dhillon, A. & Verma, G. K. Convolutional neural network: a review of models, methodologies and applications to object detection. *Prog. Artif. Intell.* **9**, 85–112 (2020).
91. Callara, A. L., Magliaro, C., Ahluwalia, A. & Vanello, N. A smart region-growing algorithm for single-neuron segmentation from confocal and 2-photon datasets. *Front. Neuroinform.* **14**, 9 (2020).
92. Richardson, D. S. et al. SRpHi ratiometric pH biosensors for super-resolution microscopy. *Nat. Commun.* **8**, 577 (2017).
93. Gao, R. et al. Cortical column and whole-brain imaging with molecular contrast and nanoscale resolution. *Science* **363**, eaau8302 (2019).
94. Randlett, O. et al. Whole-brain activity mapping onto a zebrafish brain atlas. *Nat. Methods* **12**, 1039–1046 (2015).
95. Hawrylycz, M. J. et al. An anatomically comprehensive atlas of the adult human brain transcriptome. *Nature* **489**, 391–399 (2012).
96. Mikula, S., Trotts, I., Stone, J. M. & Jones, E. G. Internet-enabled high-resolution brain mapping and virtual microscopy. *NeuroImage* **35**, 9–15 (2007).
97. Amunts, K. et al. BigBrain: an ultrahigh-resolution 3D human brain model. *Science* **340**, 1472–1475 (2013).
98. Calabrese, E. et al. A diffusion tensor MRI atlas of the postmortem rhesus macaque brain. *NeuroImage* **117**, 408–416 (2015).
99. Rohlfing, T. et al. The INIA19 template and neuromaps atlas for primate brain image parcellation and spatial normalization. *Front. Neuroinform.* **6**, 27 (2012).
100. Johnson, G. A. et al. Waxholm space: an image-based reference for coordinating mouse brain research. *NeuroImage* **53**, 365–372 (2010).
101. Papp, E. A., Leergaard, T. B., Calabrese, E., Johnson, G. A. & Bjaalie, J. G. Waxholm space atlas of the sprague dawley rat brain. *NeuroImage* **97**, 374–386 (2014).
102. Dong, H. W. *The Allen Reference Atlas: A Digital Color Brain Atlas of the C57Bl/6J Male Mouse* (John Wiley & Sons, Inc., 2008).
103. Kuan, L. et al. Neuroinformatics of the allen mouse brain connectivity atlas. *Methods* **73**, 4–17 (2015).
104. Mano, T. et al. CUBIC-Cloud provides an integrative computational framework toward community-driven whole-mouse-brain mapping. *Cell Rep. Methods* **1**, 100038 (2021).
105. Ye, L. et al. Wiring and molecular features of prefrontal ensembles representing distinct experiences. *Cell* **165**, 1776–1788 (2016).
106. Kutten, K. S. A. V. et al. in *Optics, Photonics and Digital Technologies for Imaging Applications IV* (SPIE, 2016).
107. Gradinaru, V., Treweek, J., Overton, K. & Deisseroth, K. Hydrogel-tissue chemistry: principles and applications. *Annu. Rev. Biophys.* **47**, 355–376 (2018).
108. Baiker, M. et al. Atlas-based whole-body segmentation of mice from low-contrast micro-CT data. *Med. Image Anal.* **14**, 723–737 (2010).
109. Dogdas, B., Stout, D., Chatziioannou, A. F. & Leahy, R. M. Digimouse: a 3D whole body mouse atlas from CT and cryosection data. *Phys. Med. Biol.* **52**, 577–587 (2007).
110. Schoppe, O. et al. Deep learning-enabled multi-organ segmentation in whole-body mouse scans. *Nat. Commun.* **11**, 5626 (2020).
111. Haase, R. et al. CLIJ: GPU-accelerated image processing for everyone. *Nat. Methods* **17**, 5–6 (2020).
112. Kirst, C. et al. Mapping the fine-scale organization and plasticity of the brain vasculature. *Cell* **180**, 780–795 (2020).
113. Hahn, M. et al. 3D imaging of human organs with micrometer resolution — applied to the endocrine pancreas. *Commun. Biol.* **4**, 1063 (2021).
114. Zhao, Y. et al. Nanoscale imaging of clinical specimens using pathology-optimized expansion microscopy. *Nat. Biotechnol.* **35**, 757–764 (2017).
115. Campinho, M. A. et al. A thyroid hormone regulated asymmetric responsive centre is correlated with eye migration during flatfish metamorphosis. *Sci. Rep.* **8**, 12267 (2018).
116. Konno, A. & Okazaki, S. Aqueous-based tissue clearing in crustaceans. *Zool. Lett.* **4**, 13 (2018).
117. Albanese, A. et al. Multiscale 3D phenotyping of human cerebral organoids. *Sci. Rep.* **10**, 21487 (2020).
118. Winnubst, J. et al. Reconstruction of 1,000 projection neurons reveals new cell types and organization of long-range connectivity in the mouse brain. *Cell* **179**, 268–281 (2019).
119. Weissbourd, B. et al. Functional modules within a distributed neural network control feeding in a model medusa. Preprint at *bioRxiv* https://doi.org/10.1101/2021.02.22.432372 (2021).
120. Morgan, J. L. & Lichtman, J. W. Digital tissue and what it may reveal about the brain. *BMC Biol.* **15**, 101 (2017).
121. Economo, M. N., Winnubst, J., Bas, E., Ferreira, T. A. & Chandrashekar, J. Single-neuron axonal reconstruction: the search for a wiring diagram of the brain. *J. Comp. Neurol.* **527**, 2190–2199 (2019).
122. Feng, G. et al. Imaging neuronal subsets in transgenic mice expressing multiple spectral variants of GFP. *Neuron* **28**, 41–51 (2000).
123. Cai, D., Cohen, K. B., Luo, T., Lichtman, J. W. & Sanes, J. R. Improved tools for the Brainbow toolbox. *Nat. Methods* **10**, 540–547 (2013).
124. Livet, J. et al. Transgenic strategies for combinatorial expression of fluorescent proteins in the nervous system. *Nature* **450**, 56–62 (2007).
125. Quan, T. et al. NeuroGPS-Tree: automatic reconstruction of large-scale neuronal populations with dense neurites. *Nat. Methods* **13**, 51–54 (2016).
126. Wang, X. et al. Bi-channel image registration and deep-learning segmentation (BIRDS) for efficient, versatile 3D mapping of mouse brain. *eLife* **10**, e63455 (2021).
127. Gail Canter, R. et al. 3D mapping reveals network-specific amyloid progression and subcortical susceptibility in mice. *Commun. Biol.* **2**, 360 (2019).

128. Sabdyusheva Litschauer, I. et al. 3D histopathology of human tumours by fast clearing and ultramicroscopy. *Sci. Rep.* **10**, 17619 (2020).
129. Ma, Y. et al. 3D spatiotemporal mechanical microenvironment: a hydrogel-based platform for guiding stem cell fate. *Adv. Mater.* **30**, 1705911 (2018).
130. Lloyd-Lewis, B. Multidimensional imaging of mammary gland development: a window into breast form and function. *Front. Cell Dev. Biol.* **8**, 203 (2020).
131. Yang, L. et al. Three-dimensional quantitative co-mapping of pulmonary morphology and nanoparticle distribution with cellular resolution in nondissected murine lungs. *ACS Nano* **13**, 1029–1041 (2019).
132. Cuccarese, M. F. et al. Heterogeneity of macrophage infiltration and therapeutic response in lung carcinoma revealed by 3D organ imaging. *Nat. Commun.* **8**, 14293 (2017).
133. Sindhwani, S., Syed, A. M., Wilhelm, S. & Chan, W. C. Exploring passive clearing for 3d optical imaging of nanoparticles in intact tissues. *Bioconjug Chem.* **28**, 253–259 (2017).
134. Schimmenti, L. A., Yan, H. C., Madri, J. A. & Albelda, S. M. Platelet endothelial cell adhesion molecule, PECAM-1, modulates cell migration. *J. Cell Physiol.* **153**, 417–428 (1992).
135. Konno, A., Matsumoto, N. & Okazaki, S. Improved vessel painting with carbocyanine dye-liposome solution for visualisation of vasculature. *Sci. Rep.* **7**, 10089 (2017).
136. Nehrhoff, I., Ripoll, J., Samaniego, R., Desco, M. & Gomez-Gaviro, M. V. Looking inside the heart: a see-through view of the vascular tree. *Biomed. Opt. Express* **8**, 3110–3118 (2017).
137. Lugo-Hernandez, E. et al. 3D visualization and quantification of microvessels in the whole ischemic mouse brain using solvent-based clearing and light sheet microscopy. *J. Cereb. Blood Flow. Metab.* **37**, 3355–3367 (2017).
138. Di Giovanna, A. P. et al. Whole-brain vasculature reconstruction at the single capillary level. *Sci. Rep.* **8**, 12573 (2018).
139. Rajendran, P. S. et al. Identification of peripheral neural circuits that regulate heart rate using optogenetic and viral vector strategies. *Nat. Commun.* **10**, 1944 (2019).
140. Achanta, S. et al. A comprehensive integrated anatomical and molecular atlas of rat intrinsic cardiac nervous system. *iScience* **23**, 101140 (2020).
141. Yokoyama, T. et al. Quantification of sympathetic hyperinnervation and denervation after myocardial infarction by three-dimensional assessment of the cardiac sympathetic network in cleared transparent murine hearts. *PLoS ONE* **12**, e0182072 (2017).
142. Kapp, F. G. et al. Protection from UV light is an evolutionarily conserved feature of the haematopoietic niche. *Nature* **558**, 445–448 (2018).
143. Lersten, N. R. Modified clearing method to show sieve tubes in minor veins of leaves. *Stain Technol.* **61**, 231–234 (1986).
144. Warner, C. A. et al. An optical clearing technique for plant tissues allowing deep imaging and compatible with fluorescence microscopy. *Plant. Physiol.* **166**, 1684–1687 (2014).
145. Kurihara, D., Mizuta, Y., Sato, Y. & Higashiyama, T. ClearSee: a rapid optical clearing reagent for whole-plant fluorescence imaging. *Development* **142**, 4168–4179 (2015).
146. Lu, L. et al. A rapid and effective optical-clearing technique for deep tissue fluorescence imaging in trees. *Trees Struct. Funct.* **34**, 783–790 (2020).
147. Xia, Q. et al. Solar-assisted fabrication of large-scale, patternable transparent wood. *Sci. Adv.* **7**, eabd7342 (2021).
148. Nojima, S. et al. CUBIC pathology: three-dimensional imaging for pathological diagnosis. *Sci. Rep.* **7**, 9269 (2017).
149. Belle, M. et al. Tridimensional visualization and analysis of early human development. *Cell* **169**, 161–173 (2017).
150. Dekkers, J. F. et al. High-resolution 3D imaging of fixed and cleared organoids. *Nat. Protoc.* **14**, 1756–1771 (2019).
151. Rigamonti, A. et al. Large-scale production of mature neurons from human pluripotent stem cells in a three-dimensional suspension culture system. *Stem Cell Rep.* **6**, 993–1008 (2016).
152. Cora, V. et al. A cleared view on retinal organoids. *Cells* **8**, 391 (2019).
153. Costantini, I., Cicchi, R., Silvestri, L., Vanzi, F. & Pavone, F. S. In-vivo and ex-vivo optical clearing methods for biological tissues: review. *Biomed. Opt. Express* **10**, 5251–5267 (2019).
154. Deng, Z. J. et al. Viscous optical clearing agent for in vivo optical imaging. *J. Biomed. Opt.* **19**, 76019 (2014).
155. Millon, S. R., Roldan-Perez, K. M., Riching, K. M., Palmer, G. M. & Ramanujam, N. Effect of optical clearing agents on the in vivo optical properties of squamous epithelial tissue. *Lasers Surg. Med.* **38**, 920–927 (2006).
156. Tuchin, V. V., Bashkatov, A. N., Genina, E. A., Sinichkin, Y. P. & Lakodina, N. A. In vivo investigation of the immersion-liquid-induced human skin clearing dynamics. *Tech. Phys. Lett.* **27**, 489–490 (2001).
157. Wen, X., Mao, Z. Z., Han, Z. Z., Tuchin, V. V. & Zhu, D. In vivo skin optical clearing by glycerol solutions: mechanism. *J. Biophotonics* **3**, 44–52 (2010).
158. Zhu, D., Wang, J., Zhi, Z. W., Wen, X. & Luo, Q. M. Imaging dermal blood flow through the intact rat skin with an optical clearing method. *J. Biomed. Opt.* **15**, 026008 (2010).
159. Zhao, Y. J. et al. Skull optical clearing window for *in vivo* imaging of the mouse cortex at synaptic resolution. *Light Sci. Appl.* **7**, 17153 (2018).
160. Pires, L. et al. Optical clearing of melanoma in vivo: characterization by diffuse reflectance spectroscopy and optical coherence tomography. *J. Biomed. Opt.* **21**, 081210 (2016).
161. Zhao, H. et al. A versatile strategy for improving phototherapeutic efficacy on deep-sited tumor by tissue optical clearing technique. *Nano Today* https://doi.org/10.1016/j.nantod.2020.101058 (2021).
162. Chen, K. H., Boettiger, A. N., Moffitt, J. R., Wang, S. & Zhuang, X. RNA imaging. Spatially resolved, highly multiplexed RNA profiling in single cells. *Science* **348**, aaa6090 (2015).
163. Eng, C. L. et al. Transcriptome-scale super-resolved imaging in tissues by RNA seqFISH. *Nature* **568**, 235–239 (2019).
164. Moffitt, J. R. et al. High-performance multiplexed fluorescence in situ hybridization in culture and tissue with matrix imprinting and clearing. *Proc. Natl Acad. Sci. USA* **113**, 14456–14461 (2016).
165. Dance, A. Find a home for every imaging data set. *Nature* **579**, 162–163 (2020).
166. Pleiner, T. et al. Nanobodies: site-specific labeling for super-resolution imaging, rapid epitope-mapping and native protein complex isolation. *eLife* **4**, e11349 (2015).
167. Schumacher, D., Helma, J., Schneider, A. F. L., Leonhardt, H. & Hackenberger, C. P. R. Nanobodies: chemical functionalization strategies and intracellular applications. *Angew. Chem. Int. Ed.* **57**, 2314–2333 (2018).
168. Kishi, J. Y. et al. SABER amplifies FISH: enhanced multiplexed imaging of RNA and DNA in cells and tissues. *Nat. Methods* **16**, 533–544 (2019).
169. Shah, S. et al. Single-molecule RNA detection at depth by hybridization chain reaction and tissue hydrogel embedding and clearing. *Development* **143**, 2862–2867 (2016).
170. Lin, R. et al. A hybridization-chain-reaction-based method for amplifying immunosignals. *Nat. Methods* **15**, 275–278 (2018).
171. Saritas, T., Puelles, V. G., Su, X.-T., Ellison, D. H. & Kramann, R. Optical clearing and imaging of immunolabeled kidney tissue. *J. Vis. Exp.* https://doi.org/10.3791/60002 (2019).
172. Xu, F. et al. High-throughput mapping of a whole rhesus monkey brain at micrometer resolution. *Nat. Biotechnol.* https://doi.org/10.1038/s41587-021-00986-5 (2021).
173. Hama, H. et al. Scale: a chemical approach for fluorescence imaging and reconstruction of transparent mouse brain. *Nat. Neurosci.* **14**, 1481–1488 (2011).
174. Wang, X. et al. Three-dimensional intact-tissue sequencing of single-cell transcriptional states. *Science* **361**, eaat5691 (2018).

Acknowledgements

The authors thank K. Matsumoto and S. Y. Yoshida for help constructing Figs 5 and 6, respectively, and E. Diel and I. Boothby for preparing samples in Figs 5, 7 and 9. This work was supported by a Japan Science and Technology Corporation (JST) Exploratory Research for Advanced Technology (ERATO) grant (JPMJER2001). H.R.U. was supported by the Science and Technology Platform Program for Advanced Biological Medicine (AMED/MEXT), a Japan Society of the Promotion of Science (JSPS) KAKENHI grant-in-aid for scientific research (JP18H05270), a grant-in-aid from the Human Frontier Science Program and a MEXT Quantum Leap Flagship Program (MEXT QLEAP) grant (JPMXS0120330644). K.M. was supported by a JSPS KAKENHI grant-in-aid for scientific research (20K06885) and a JST Moonshot R&D grant (JPMJMS2023). A.E. was supported by the European Research Council (ERC) Calvaria project, the Vascular Dementia Research Foundation and the Deutsche Forschungsgemeinschaft (DFG, German Research Foundation) under Germany's Excellence Strategy within the framework of the Munich Cluster for Systems Neurology (EXC 2145 SyNergy, ID 390857198). K.C. was supported by a Burroughs Wellcome Fund Career Awards at the Scientific Interface, the Searle Scholars Program, the Packard award in Science and Engineering, the NARSAD Young Investigator Award, the McKnight Foundation Technology Award, the JPB Foundation (PIIF and PNDRF), the Institute for Basic Science (IBS-R026-D1) and the NIH grants 1-DP2-ES027992 and U01MH117072. J.W.L. is supported by NIH grants U19NS104653 and P50MH094271. Resources that may help to enable general users to establish the methodology are freely available online at http://www.chunglabresources.org.

Author contributions

Introduction (D.S.R. and J.W.L.); Experimentation (D.S.R., W.G., K.M., C.P., K.C., A.E., H.R.U. and J.W.L.); Results (D.S.R., W.G., K.M., C.P., K.C., A.E., H.R.U. and J.W.L.); Applications (D.S.R., W.G., K.M., C.P., K.C., A.E., H.R.U. and J.W.L.); Reproducibility and data deposition (D.S.R., W.G., K.M., C.P., K.C., A.E., H.R.U. and J.W.L.); Limitations and optimizations (D.S.R., W.G., K.M., C.P., K.C., A.E., H.R.U. and J.W.L.); Outlook (D.S.R. and J.W.L.); overview of the Primer (D.S.R. and J.W.L.).

Competing interests

H.R.U. is co-founder of CUBICStars, Inc. and a co-inventor on the following patent applications covering the CUBIC reagents: PCT/JP2014/070618 (pending, patent applicant is RIKEN, other co-inventors are E. A. Susaki and K. Tainaka); PCT/JP2017/016410 (pending, patent applicant is RIKEN, other co-inventors are K. Tainaka and T. Murakami). K.C. is an inventor for patent applications covering some technologies described in this paper and co-founder of LifeCanvas Technologies. A.E. and C.P. have filed a patent on whole-body clearing and imaging related technologies. The other authors declare no competing interests.

Peer review information

Nature Reviews Methods Primers thanks Alan King Lun Liu, Woong Sun, Valery Tuchin and the other, anonymous, reviewer(s) for their contribution to the peer review of this work.

RELATED LINKS

Aivia: https://www.aivia-software.com/
Arivis Vision4D: https://imaging.arivis.com/en/imaging-science/arivis-vision4d
Cell Image Library: http://www.cellimagelibrary.org/home
ilastik: https://www.ilastik.org/
Image Data Resource: http://idr.openmicroscopy.org/about/
Imaris: https://imaris.oxinst.com/
Intellisis: https://www.zeiss.com/microscopy/us/products/microscope-software/zen-intellesis-image-segmentation-by-deep-learning.html
Napari: https://napari.org/
Online repository for tissue clearing-validated antibodies: https://idisco.info/validated-antibodies/
Trainable Weka Segmentation: https://imagej.net/plugins/tws/

nature protocols

REVIEW ARTICLE

https://doi.org/10.1038/s41596-020-0360-2

Tutorial: avoiding and correcting sample-induced spherical aberration artifacts in 3D fluorescence microscopy

Erin E. Diel[1], Jeff W. Lichtman[1,2,3] and Douglas S. Richardson[1,2]✉

Spherical aberration (SA) occurs when light rays entering at different points of a spherical lens are not focused to the same point of the optical axis. SA that occurs inside the lens elements of a fluorescence microscope is well understood and corrected for. However, SA is also induced when light passes through an interface of refractive index (RI)-mismatched substances (i.e., a discrepancy between the RI of the immersion medium and the RI of the sample). SA due to RI mismatches has many deleterious effects on imaging. Perhaps most important for 3D imaging is that the distance the image plane moves in a sample is not equivalent to the distance traveled by an objective (or stage) during *z*-stack acquisition. This non-uniform translation along the *z* axis gives rise to artifactually elongated images (if the objective is immersed in a medium with a higher RI than that of the sample) or compressed images (if the objective is immersed in a medium with a lower RI than that of the sample) and alters the optimal axial sampling rate. In this tutorial, we describe why this distortion occurs, how it impacts quantitative measurements and axial resolution, and what can be done to avoid SA and thereby prevent distorted images. In addition, this tutorial aims to better inform researchers of how to correct RI mismatch–induced axial distortions and provides a practical ImageJ/Fiji-based tool to reduce the prevalence of volumetric measurement errors and lost axial resolution.

Spherical aberration occurs when light entering the periphery of a spherical lens is focused to a different point on the optical axis than paraxial light rays that enter near the lens's center (Fig. 1a). Lens-induced SA is well understood and is corrected for in the optical components of modern microscopes. However, SA can also be induced by the sample. If converging or diverging light passes through an interface of differing refractive indices (RIs), SA will occur. Two scenarios for imaging through an RI-mismatched interface commonly occur: imaging with an oil immersion objective into a watery live-cell sample and imaging into a high-RI mounting medium or tissue-clearing solution with an air immersion objective. SA created by these types of RI mismatches has three deleterious effects on imaging. First, because all the rays of light originating from a point object do not converge precisely at the image plane, images are dim and blurred. This can be seen in both wide-field (Fig. 1b) and confocal (Fig. 1c) light paths, although the confocal pinhole may reduce axial blur relative to that of wide-field microscopy at the cost of further signal loss. Second, owing to refraction of the more peripheral rays entering the objective—especially at high numerical aperture (NA) values—the nominal focus position (where the focal plane would reside in the absence of refraction) is shifted (Fig. 1b,c). Again, this is seen in both wide-field (Fig. 1b) and confocal (Fig. 1c) microscopes. However, in the confocal microscope, the refraction of both the focusing excitation light and the emitted fluorescence must be considered. The focal shift is related to the NA of the objective and the degree of the RI mismatch. Third, and perhaps most important for 3D imaging, the distance the image plane moves in a sample is not equivalent to the distance traveled by an objective (or stage) during *z*-stack acquisition (Fig. 1d). This non-uniform translation along the *z* axis gives rise to artifactually elongated images (if light travels from a high-RI immersion medium to a lower-RI sample) or compressed images (if imaging from a low-RI immersion medium to a higher-RI sample).

Avoiding spherical aberration–based axial distortion

When preparing samples for a microscopy experiment, the choices of mounting medium and microscope objective are often made independently. Mounting media are primarily chosen on the basis of their antifade properties (ability to prevent photobleaching), whereas objectives are selected on the basis of their theoretical achievable resolution. The resulting RI mismatches have little effect on image quality for thin samples or 2D imaging within a few micrometers of a coverslip. However, 3D fluorescence microscopy images are rapidly degraded by SA if the objective's immersion medium and the sample mounting medium differ in RI or if an incorrect thickness of coverslip is used[1]. Therefore, the choice of immersion medium

---

[1]Harvard Center for Biological Imaging, Harvard University, Cambridge, MA, USA. [2]Department of Molecular and Cellular Biology, Harvard University, Cambridge, MA, USA. [3]Center for Brain Science, Harvard University, Cambridge, MA, USA. ✉e-mail: drichardson@fas.harvard.edu

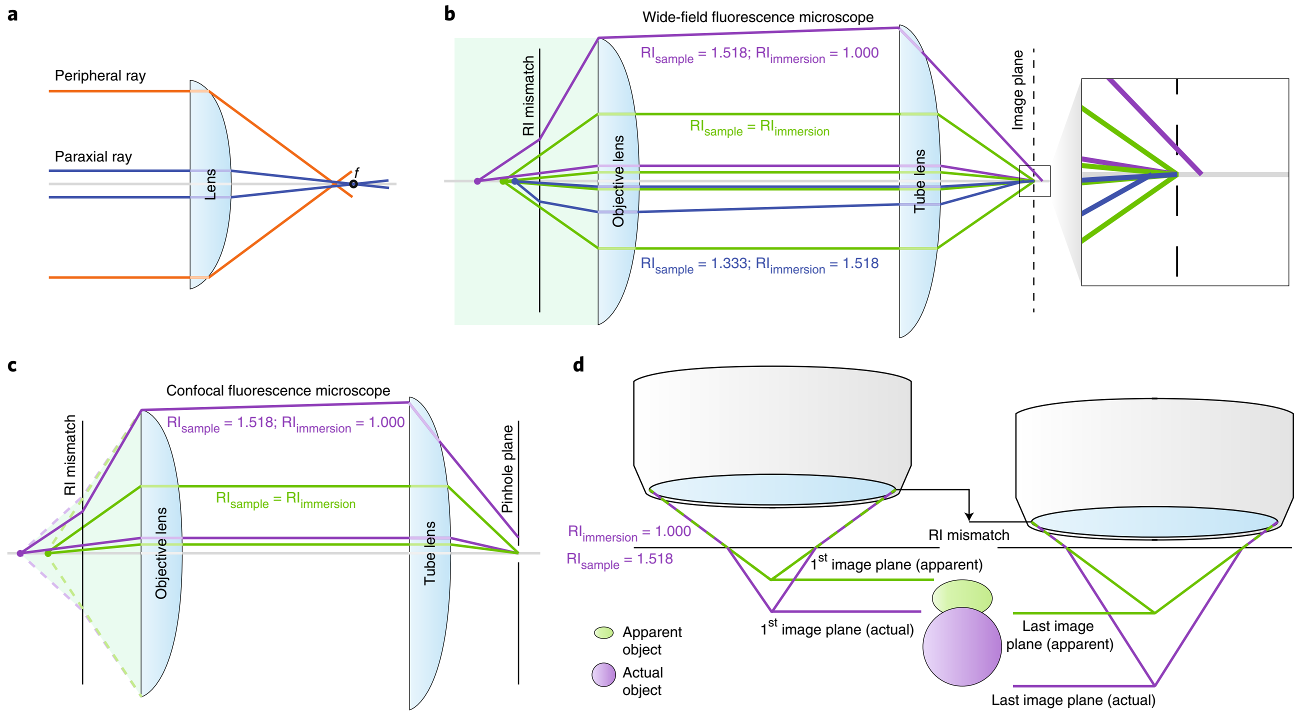

Fig. 1 | Refractive index mismatches induce spherical aberration and axial distortion. a, Lens-based SA occurs when light rays entering near the edge of a lens (peripheral rays, orange) are focused before the focal point (*f*). Light rays entering near the center of the objective (paraxial rays, blue) intersect the optical axis (gray) at the focal point. **b**, Ray trace of light traveling from a point source to the image plane in a wide-field fluorescence microscope. Green shading represents collimated excitation light exiting the objective. Dots (point sources) and lines (ray traces) represent the path light travels when $\mathrm{RI}_{\mathrm{sample}} > \mathrm{RI}_{\mathrm{immersion}}$ (purple), $\mathrm{RI}_{\mathrm{sample}} = \mathrm{RI}_{\mathrm{immersion}}$ (green), and $\mathrm{RI}_{\mathrm{sample}} < \mathrm{RI}_{\mathrm{immersion}}$ (blue). The point source must be located in a different focal plane in each situation to ensure its image is focused near the image plane (dashed line); however, when an RI-mismatched interface exists, SA occurs (see zoomed region, right). **c**, Ray trace of light traveling from a point source to the pinhole plane in a confocal fluorescence microscope. As in **b**, ray tracing diagrams are shown for RI-matched (green) and $\mathrm{RI}_{\mathrm{sample}} > \mathrm{RI}_{\mathrm{immersion}}$ (purple) under confocal illumination and detection. In a confocal system, both excitation light (shading within green or purple dashed lines) and emitted fluorescence light rays (green or purple solid lines) undergo refraction if an RI-mismatched interface exists (purple). **d**, An objective is moved axially (black arrow) in a stepwise manner to obtain a 3D image. If there is no change in the RI between the objective and the focal point, no refraction will occur (green lines) and the distance the objective moves (black arrow) is equivalent to the distance moved by the focal plane (green horizontal lines). However, if an RI-mismatched interface exists between the objective and the object to be imaged, refraction occurs, and the focal point is shifted (purple lines). In this scenario, the movement of the objective (black arrow) is not equivalent to the movement of the focal plane (purple horizontal lines). Therefore, when imaging a spherical object ('actual object', purple) that is embedded in a medium with an RI value higher than that of the immersion medium of the objective, a 3D rendering of the object will be compressed in the axial dimension ('apparent object', green) because the acquisition software has assigned the distance of the objective's travel—not the focal plane's travel—to the object's *z* axis.

and objective should be made in unison, with the goal being to match the RI of an objective's immersion medium as closely as possible to the RI of the sample's mounting medium. For example, water immersion or dipping objectives have long been preferred for imaging into living samples because the average RI of a cell (1.360–1.380) is closer to that of water than typical microscope immersion oil[2,3]. Further, many water immersion and dipping objectives have correction collars that can be adjusted to compensate for coverslip thickness, temperature and/or RI mismatch[3,4]. Correction collars therefore extend the useful RI range of a water immersion objective beyond 1.333[3]. Silicone oil immersion objectives (RI = 1.400) offer another alternative for live-cell imaging. The higher RI of silicone oil enables these objectives to be designed with higher NAs, making them particularly suited to super-resolution live-cell imaging[5,6] (see also Table 1). Researchers should take note because sacrificing theoretical resolution by using a lower-NA glycerol immersion objective to image samples in glycerol-based commercial mounting media can produce a higher-quality image compared with using a higher-NA oil immersion objective (see 'Common instances of spherical aberration–based axial distortion in 3D imaging').

A perfect RI match between immersion and mounting medium is not always possible. As an alternative, specialized hardware that can compensate for RI mismatches can be used. A dipping cap can be installed to convert an air objective into a 'pseudo' dipping lens by attaching a cover with a glass window to the sample side of the objective[7]. The glass window is inserted directly into the mounting medium and maintains a constant air gap between the front lens and the mounting medium as the objective moves up and down while imaging the sample, preventing SA-induced axial distortions. Another option is to translate the sample inside a chamber filled with mounting medium while the imaging objective(s) remain(s) stationary outside the chamber[8]. A third option is to place a deformable mirror or spatial light modulator (referred to as

Table 1 | Summary of common refractive indices in microscopy

RIs of common objective immersion media		RIs of common biological samples	
Immersion medium	**RI**	**Sample**	**RI**
Air	1.000	Live tissue	1.360–1.380
Water	1.333	Fixed tissue in glycerol-based mounting medium	1.400–1.470
Silicone oil	1.405	Fixed tissue in high-RI mounting medium	1.520
85% Glycerol	1.456	Aqueous-based cleared tissue	1.380–1.460
Oil	1.518	Solvent-based cleared tissue	1.500–1.560

adaptive optics) to correct the many types of aberrations that can occur across a field of view[9]. Finally, radially symmetric phase masks have been used to equilibrate the SA across all depths of a sample, enabling simplified image restoration by deconvolution after image aquisition[10]. Although these options are useful, they require specialized equipment that may not be an option for every researcher. Therefore, methodologies to correct for axial distortion via post-processing are still required.

Common instances of spherical aberration–based axial distortion in 3D imaging

Throughout this tutorial, we will focus on one historic and two modern RI mismatches in 3D fluorescence microscopy. First, when confocal microscopy was pioneered in the early 1990s, live biological samples (RI = up to 1.380) were primarily imaged with oil immersion objectives (RI = 1.518) because these had the highest NAs and were thought to achieve the highest possible theoretical resolution. As discussed above, the use of oil immersion objectives for live-cell imaging produces an artificial stretching of the data in the axial dimension. Second, modern-day fixed fluorescent samples are primarily mounted in glycerol-based antifade mounting media (RI = 1.400–1.470) and imaged with air (RI = 1.000) or oil (RI = 1.518) immersion objectives. Imaging of this nature will artificially compress (air objective) or stretch (oil objective) the 3D images. Third, imaging of tissue that is millimeters in thickness is now commonplace via advanced confocal and light-sheet microscopy techniques in combination with tissue-clearing approaches (RI = 1.380–1.560) (ref. [11]). In all three of these situations, the RIs of the most common objective immersion media (air, glycerol, oil) rarely match the RI of the sample to be imaged (Table 1). Although oil or glycerol immersion objectives provide a reasonable RI match to many samples, the primary role of these immersion media is to increase the NA of an objective and thus its theoretical resolution. Unfortunately, increasing the NA of an objective results in a decrease in working distance and field of view (unless the diameter of the front lens is also increased). Therefore, most fluid immersion objectives are limited to a working distance of a few hundred micrometers and are incompatible with 3D imaging of thick samples. For these reasons, air objectives are used for imaging thick sectioned and/or cleared tissue because of their long working distances and large fields of view. Air objectives will always induce SA-based axial distortion when used for 3D imaging because the RI of any sample is >1.000 (the RI of air). The appearance of axial distortion from the use of air objectives is therefore quite common in published works. RI mismatches in cleared-tissue imaging are especially hard to avoid (Table 1) and can be found in several published works, including early pioneering studies[12,13]. The artificial compression of 3D images that occurs when imaging into high-RI cleared samples has a severe impact on quantitative measurement of volume and can also affect axial resolution.

Calculating axial distortion correction factors (high to low RI mismatch)

If an RI mismatch cannot be avoided, 3D images must be corrected for axial distortion. SA-based axial distortion of images was first noted during the early development of confocal microscopes. At this time, confocal microscopes primarily used high-NA oil immersion objectives (RI = 1.518) to image live-cell cultures (RI = 1.360–1.380) or fixed-cell cultures (RI = 1.400–1.470) with lower RIs. This RI mismatch resulted in an artificial stretch in the axial dimension during imaging. Using a simple ray optics approach, Carlsson[14] first proposed that this focal shift could be predicted by calculating a correction factor by obtaining the ratio of the RI of a sample's mounting medium to the RI of the imaging objective's immersion medium ($n_{\text{sample}}/n_{\text{immersion}}$). Although Carlsson's calculation provides a good approximation for low-NA objectives, it does not account for the increased axial distortion that is observed with high-NA objectives. Therefore, at high NA, the Carlsson formula underestimates the focal shift. Soon after, Visser et al.[15] developed a formula to calculate axial distortion that considered the NA of the objective (Eq. 1).

$$\Delta_f = \frac{\tan\left(\sin^{-1}\frac{NA}{n_1}\right)}{\tan\left(\sin^{-1}\frac{NA}{n_2}\right)}\Delta_s \qquad (1)$$

Here, Δ_f represents the movement of the focal plane within the sample and Δ_s represents the movement of the stage or objective. Unfortunately, Sheppard et al.[16] and Hell et al.[17] later showed that Eq. 1 overestimates the axial distortion at high NA values because it considers only the most peripheral rays emitted from an objective lens and ignores the relatively greater contribution from paraxial rays. In 1993, Hell et al.[17] provided a wave optics solution that is now widely accepted as the most accurate estimation of axial distortion. Using this method, they were able to predict the decrease in resolution, the decrease in signal intensity and the focal distortion at various imaging depths with high precision. However, wave optics requires complex calculations, and this complexity has probably contributed to the underutilization of this method within the microscopy community. Currently, if microscopists desire to correct an axially distorted image after acquisition, they have the choice of two simple, but inaccurate, equations or one highly complex mathematical formula. Here, we describe two simple modifications to Eq. 1 that can be used to improve its accuracy at high NA and/or large RI mismatches.

Rather than calculating the focal shift of only the most peripheral rays (Visser et al.[15], Eq. 1), we recommend calculating the mean or median depth at which 100 rays equally spaced along the radius of an objective's front lens intersect the optical axis in the sample. We have found that this simple ray optics approach approximates the complex, and difficult to implement, wave optics methods of Hell et al[17] quite well. Therefore, we recommend the use of Eq. 2 (mean) or 3 (median) (see derivation in Supplemental Note 1) for correcting axial distortion when imaging through RI mismatches.

$$\frac{d\prime}{d} = \frac{1}{100}\cdot\sum_{k=1}^{100}\frac{\tan\left(\sin^{-1}\frac{k\mathrm{NA}}{100n_1}\right)}{\tan\left(\sin^{-1}\frac{k\mathrm{NA}}{100n_2}\right)} \tag{2}$$

$$\frac{d\prime}{d} = \frac{\tan\left(\sin^{-1}\frac{0.5\mathrm{NA}}{n_1}\right)}{\tan\left(\sin^{-1}\frac{0.5\mathrm{NA}}{n_2}\right)} \tag{3}$$

In Eqs. 2 and 3, d'/d is a correction factor that relates the actual focal position (d') to the expected focal position (d). k is an integer used to increment through equally spaced rays along the radius of the optical axis. Figure 2 shows that Eqs. 2 and 3 perform better than the ray optics approaches of Carlsson and Visser et al. as compared with the wave optics calculations from Hell et al. In addition, Eqs. 2 and 3 are not biased by high NA values (Fig. 2a) or large differences in RI values (Fig. 2b), as is Eq. 1. Therefore, Eqs. 2 and 3 are simple formulas for estimating the focal shift when imaging from a high (oil immersion) to low (water) RI. We discuss the differences between the mean and median approaches in the 'Mean versus median correction factor' section below.

3D imaging from a high-RI oil immersion medium to a lower-RI live-cell sample is rare today because most researchers know to select water or silicone oil immersion objectives for these types of experiments. However, imaging from a high RI to a low RI in fixed samples is still common. Most commercially available mounting media are glycerol based and have an RI close to 1.450. Clearly, this is poorly matched to the RI of immersion oil (1.518). According to Eqs. 2 and 3, axial correction factors of 0.92 or 0.94, respectively, should be applied to images acquired under these conditions (RI immersion = 1.518; RI sample = 1.45; NA = 1.4). However, in practice the axial distortion of these samples is often minimal because the short working distances of high-NA oil immersion objectives (100–200 μm) limits the maximal axial distortion (stretch) to tens of micrometers.

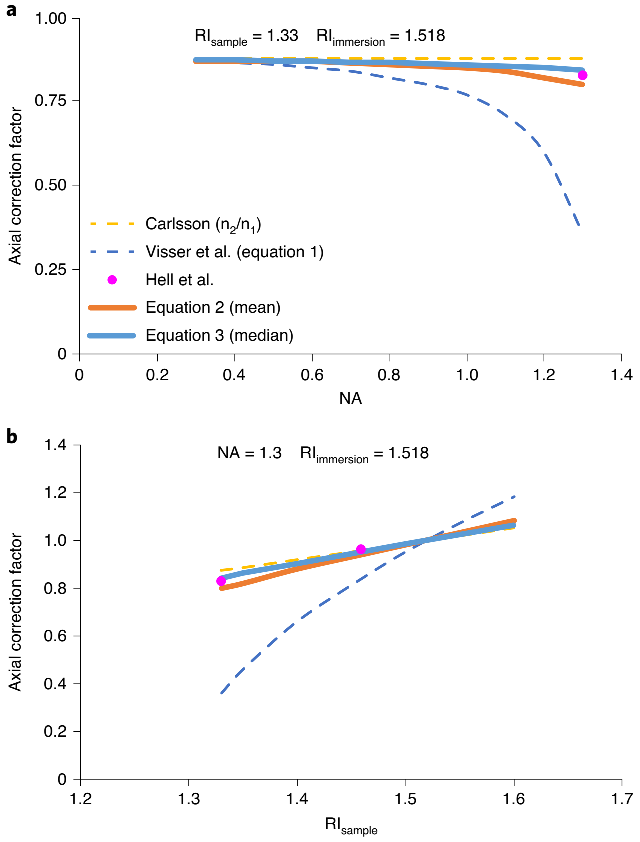

Fig. 2 | Comparison of methods for determining refractive index-mismatch correction factors (high to low refractive index). Correction factors were calculated and plotted using equations and data from Carlsson[14], Visser et al.[15] (Eq. 1), Hell et al.[17] and Eqs. 2 and 3 of the current paper. **a**, The axial correction factor was calculated across NA values of 0.3–1.3 for an oil immersion objective (RI = 1.518) imaging into a solution of RI = 1.33. All methods show close agreement at NA < 0.5. **b**, The axial correction factor was calculated for an NA = 1.3 oil immersion objective imaging into solutions ranging in RI from 1.3 to 1.6. Equations 2 and 3 of the current paper (solid blue and orange lines) show the best agreement with wave optics calculations by Hell et al. (magenta dots).

Calculating axial distortion correction factors (from low to high RI)

Currently, a greater concern is the opposite imaging situation: imaging from a low-RI immersion medium into a high-RI sample. This occurs when air immersion objectives are chosen to facilitate imaging large fields of view (due to lower magnification) or thicker samples (due to longer working distances). It can also occur when immersion objectives are used to image into samples cleared with high-RI tissue-clearing solutions. Therefore, it is important to compare the performance of the various axial distortion correction strategies when imaging from a low-RI immersion medium (such as air) into a high-RI mounting medium or tissue-clearing solution. To our knowledge, a wave optics approach has not been applied to this low

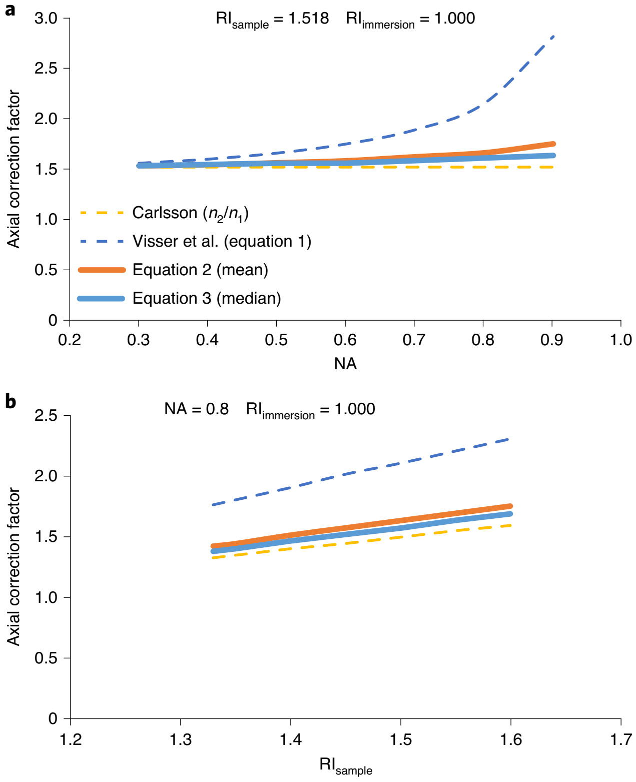

Fig. 3 | Comparison of methods for determining refractive index mismatch correction factors (low to high refractive index). Correction factors were calculated and plotted using equations and data from Carlsson[14], Visser et al.[15] (Eq. 1), and Eqs. 2 and 3 of the current paper. **a**, The axial correction factor was calculated across NA values of 0.3–0.9 for an air immersion objective (RI = 1.000) imaging into a solution of RI = 1.518. **b**, The axial correction factor was similarly calculated for an NA = 0.8 air immersion objective (RI = 1.000) imaging into solutions ranging in RI from 1.33 to 1.60.

RI to high RI imaging scenario. However, ray optics can be easily extended to this context. Figure 3 displays correction factors for imaging into high-RI samples with air immersion objectives calculated with the same ray optics approaches used in Fig. 2. Again, the Carlson and Visser equations appear to underestimate or overestimate, respectively, the correction factor at high NA values.

Experimental demonstration of correcting axial distortions

Validation using fluorescent beads

To confirm the validity of Eqs. 2 and 3 when imaging from low to high RI, a simple experiment can be performed. Fluorescent beads are fixed to a microscope slide and overlaid with solutions of differing RI (see Supplementary Methods). A coverslip is then placed above these solutions on a spacer (Fig. 4a). If a 3D field of view is imaged at the interface of these solutions and the neighboring empty space, the focal shift due to SA can be calculated. Figure 4b displays such an experiment, in which 2-μm fluorescent beads were placed 200 μm below a coverslip. Droplets of immersion media with RI = 1.333 and RI = 1.518 were placed over the beads. When images were taken at the interface of these solutions with a 0.45-NA air immersion objective, the beads in high-RI medium (1.333 or 1.518) appeared elevated above the glass slide relative to those residing in air (Fig. 4b–d). In this example (RI immersion = 1.000; RI sample = 1.000, 1.333 or 1.518; and NA = 0.45), Eqs. 2 and 3 calculate nearly identical correction factors for the following conditions: 1.00 (beads in air), 1.35 (beads in RI = 1.333), and 1.54 (Eq. 3) or 1.55 (Eq. 2) (beads in RI = 1.518). If Eqs. 2 and 3 are accurate, multiplying the z spacing of the images by the correction factor should restore the beads to their correct axial positions. Figure 4c (right panels) and 4d show exactly this (using Eq. 2). Therefore, Eqs. 2 and 3 can be used to correct 3D volumetric data that is distorted by imaging from a low-RI immersion medium into a high-RI sample.

Correcting axial distortion in 3D volumes

Figure 1d depicts how SA causes the image plane to move through a sample at a different rate than the objective (or stage) travels during 3D image acquisition. This mismatched travel speed results in an SA-induced z-axis elongation or compression that must be corrected before performing quantitative volumetric analysis. Figure 5a illustrates one of the common experimental conditions discussed above: imaging a sample in a glycerol-based commercial mounting medium (RI = 1.460). If a glycerol objective is chosen, the immersion medium is well matched to the RI of the mounting medium and no axial distortion correction is required. Here, a measurement along the z axis represents the true thickness of the tissue section (Fig. 5a). When the exact same region is imaged with an air immersion objective of equivalent NA, the resulting image is axially compressed to approximately 60% of its actual thickness (Fig. 5a). To correct for this compression, a correction factor should be calculated using Eq. 2 or 3 and the values RI immersion = 1.000, RI sample = 1.460, and NA = 0.8. Next, the z step of the acquired image is multiplied by the correction factor (1.59, via Eq. 2) to stretch the image to its actual thickness (Fig. 5a, compare air immersion original (Org) with z-corrected (Zcor)). Similarly, when imaging a cleared organoid (clearing solution RI = 1.560, see Supplementary Methods) with a 0.45-NA air immersion objective, the raw data are artificially compressed in the axial dimension. Volumetric analysis of the original and corrected images suggests the volume of the organoid is underestimated by more than 1.5× if uncorrected (Fig. 5b). A correction factor of 1.59 (calculated using Eq. 2) adjusts the axial dimension of the image, and a more accurate estimation of the spheroid's volume is obtained. Therefore, before performing volumetric measurements on 3D images acquired through an RI-mismatched interface, it is essential that the axial distortion be first corrected following the methods outlined below.

Experimental demonstration of determining axial sampling rates

Effect of spherical aberration on axial sampling

SA-induced distortion can also affect the achievable axial resolution of a microscope. Because the movement of the focal

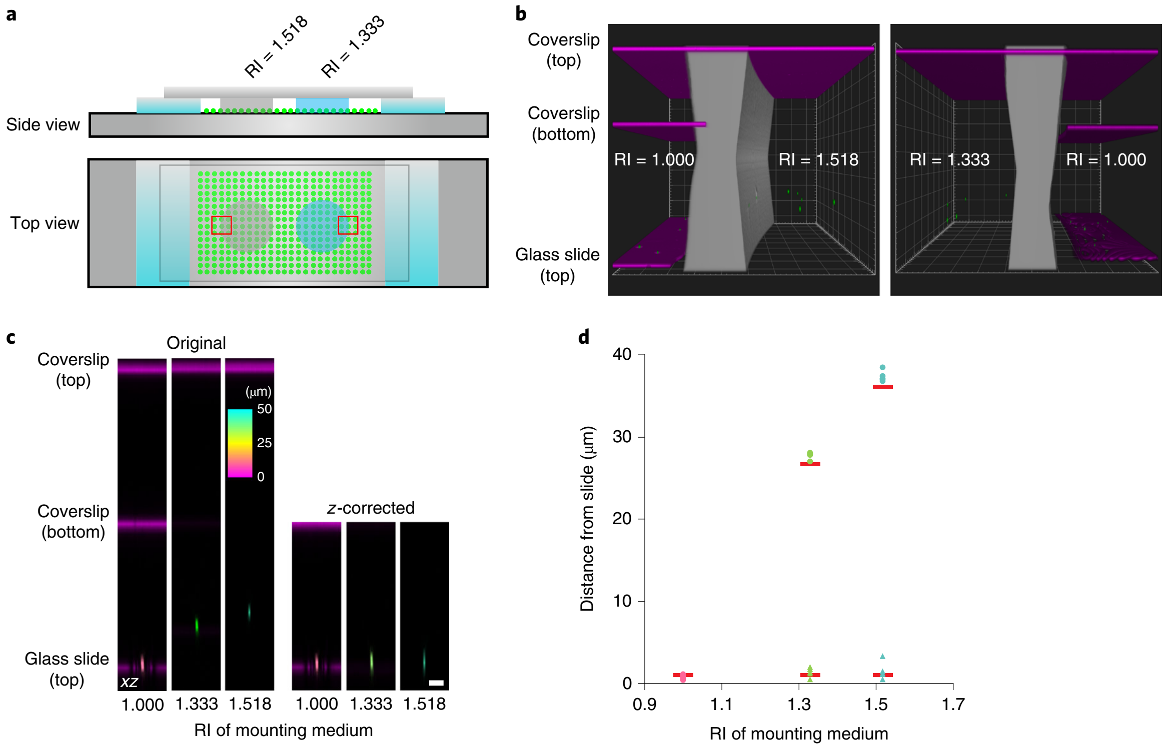

Fig. 4 | Refractive index mismatches induce a focal shift. a, Diagram of the fluorescent bead preparation for measuring focal shift in media of various RI values. Fluorescent beads (green circles) were adhered to a microscope slide between double-sided tape spacers (Supplementary Methods). Drops of RI = 1.333 (blue) and RI = 1.518 (gray) liquids were placed over the beads. A no. 1.5 coverslip was placed on the liquid drops and spacers. Red boxes indicate areas of air–liquid interfaces, where multiple beads residing in both RIs could be imaged in a single field of view. **b**, 3D rendering of volumes captured at the air–liquid interface, as indicated in **a**, using 200-µm spacers. The left panel images through a liquid with RI = 1.518, and the right panel images through RI = 1.333. Beads (2 µm; green) were visualized by fluorescence microscopy; the coverslip and glass slide surfaces were visualized by reflected light imaging (magenta), and the edge of the droplet was detected via transmitted light (intensity is inverted and pseudo-colored gray; see Supplementary Methods). Beads appear elevated when overlaid with solution. White boxes are 40 µm^2. **c**, The experiment in **b** was repeated with a 100-µm spacer. Orthogonal (*xz*) color-coded depth projections of individual fluorescent beads are presented. The color of the bead indicates its distance from the glass slide according to the color scale. Reflections from the coverslip and microscope slide are shown in magenta. *z*-corrected images of the 1.333- and 1.518-RI embedded beads are also shown in the right-hand panels. Scale bar, 10 µm. **d**, Distance from the glass slide (apparent focal shift) was calculated and plotted for five beads outside the liquid drops (RI = 1.000, pink dots), five beads in the RI = 1.333 medium (green dots), and five beads in the RI = 1.518 medium (cyan dots). The distances between the beads in RI = 1.333 and RI = 1.518 and the slide were remeasured after applying a *z* correction as in **c** (green and cyan triangles, respectively). Red bars indicate the expected bead positions predicted by Eq. 2.

plane within a sample is accelerated or decelerated relative to the physical movement of the objective, the optimal *z* step (axial sampling rate) must be adjusted accordingly. It is well understood that to maximize the resolution of a microscope in any dimension, the sampling rate (number of pixels) must be at least twice the theoretical resolution limit of the imaging system (referred to as Nyquist sampling). Several equations (for an example, see Supplementary Note 2) can be used to determine the correct *z* step. Commercial microscope software uses these equations to recommend an ‘optimal’ axial sampling rate. Unfortunately, these equations will recommend too small (if imaging from high to low RI) or too large (if imaging from low to high RI) of a *z* step when imaging through an RI-mismatched interface. Therefore, when imaging into a lower-RI sample (relative to the immersion medium of the objective), the *z* planes will be too close together, and excessive photobleaching or phototoxicity may be induced in the sample. Conversely, when imaging into a higher RI sample, the *z* step will be too large, and the achievable resolution of the microscope will be reduced. Figure 5c demonstrates that imaging at the suggested *z* step fails to resolve all labeled axons in an axial (*xz*) maximum intensity projection of a thick tissue volume. All images were corrected after imaging for axial distortion, demonstrating that the sampling rate must be determined before, not after, imaging is performed.

Correct axial sampling improves segmentation

The initial step of most image analysis routines is to segment objects of interest. Failure to adjust the axial sampling rate (*z* step) according to any RI-mismatches that exist between the sample and the objective’s immersion medium will impact a researcher’s ability to properly segment individual objects. Figure 6a displays an automated segmentation of the image in Fig. 5c. More objects are segmented (12 versus 7) when the correct axial sampling rate is calculated before imaging and the *z* spacing is corrected after acquisition. The increase in the

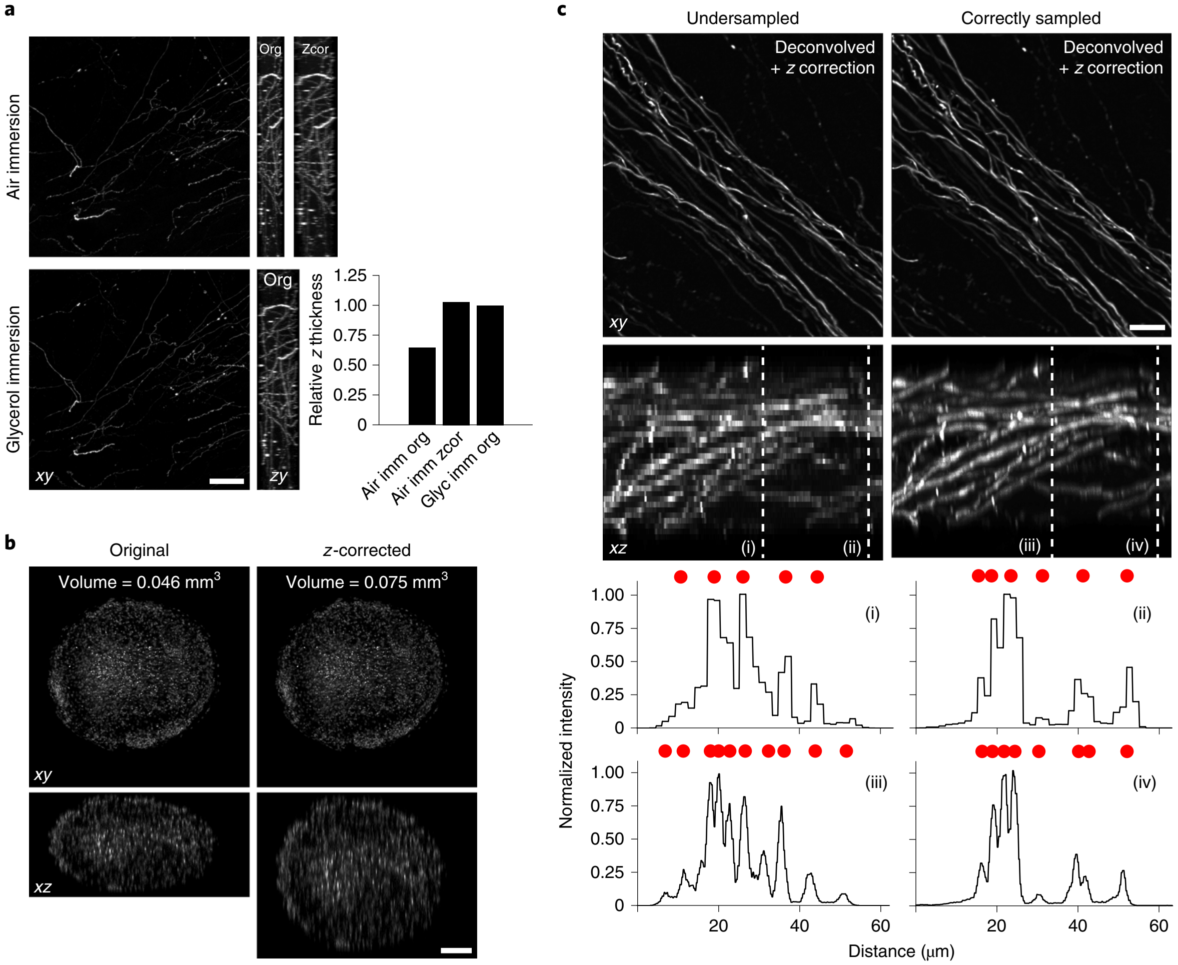

Fig. 5 | Refractive index mismatches induce spherical aberration and axial distortion. a, A 50-μm-thick region of mouse brain tissue expressing the tdTomato fluorescent protein in a subset of neurons was imaged with a 20× 0.8-NA air or a 25× 0.8-NA glycerol immersion objective (Supplementary Methods). Gamma-adjusted (0.5) maximum intensity projections are displayed for the lateral (*xy*) and axial (*zy*) planes. The *zy* plane is shown before (Org) and after (Zcor) *z*-axis compression correction for the air objective. The relative thickness (*z* dimension), normalized to the glycerol immersion projection (Glyc Imm Org), is displayed for the air immersion objective's original (Air Imm Org) and *z*-corrected (Air Imm Zcor) projections. Scale bar, 50 μm. **b**, Lateral (*xy*) and axial (*xz*) slices through an organoid labeled with the SiR-DNA nuclear dye are presented. Organoids were cleared (Supplementary Methods) and imaged in dibenzyl ether (RI = 1.560) with a 10× 0.45-NA objective. Volumetric measurements were calculated for 3D-rendered uncorrected and *z*-corrected datasets. Scale bar, 100 μm. **c**, Lateral (*xy*) and axial (*xz*) maximum intensity projections were calculated for confocal image stacks acquired through the same mouse brain section as in **a**. The volume was imaged twice: (1) using the manufacturer's recommended *z* step (undersampled) and (2) at an adjusted *z* step that accounts for SA-induced focal shift (see Supplementary Note 2). To quantitate the number of neuronal processes resolved under different sampling conditions, pixel intensity profiles were determined along the indicated dotted lines and plotted; Roman numerals in the images correspond to those in the plots. Red dots represent individually resolved axons. Scale bar, 10 μm.

number of segmented objects results for two reasons. First, in an undersampled dataset, thin objects that lie parallel to the lateral plane may appear on only a single (or very few) slice(s). Therefore, the object's 3D volume is small and falls below the volume threshold value that is set to exclude small, artifactual objects. If an object's volume is below the set threshold, it is deemed too small to be relevant and is excluded. These objects cannot be recovered by lowering the threshold because the image becomes overwhelmed with small punctate structures that often represent debris or staining artifacts. In Fig. 6a, the threshold was set to 10,000 pixels. Four thin objects that lie in the lateral plane can be segmented only in the properly sampled dataset (Fig. 6a, right panel, white arrowheads). Second, objects lying directly above one another can falsely appear connected if the axial sampling rate is insufficient to resolve both structures. Figure 6b displays two axons that could not be segmented in the undersampled dataset but are clearly two separate objects when the sample is reimaged at the correct axial sampling rate. Therefore, it is critical to calculate an adjusted axial sampling rate (*z* step) before imaging to ensure optimal axial resolution as described in the methods outlined below. It is essential to understand that axial resolution cannot be increased or recovered through post-processing if the original image is under sampled.

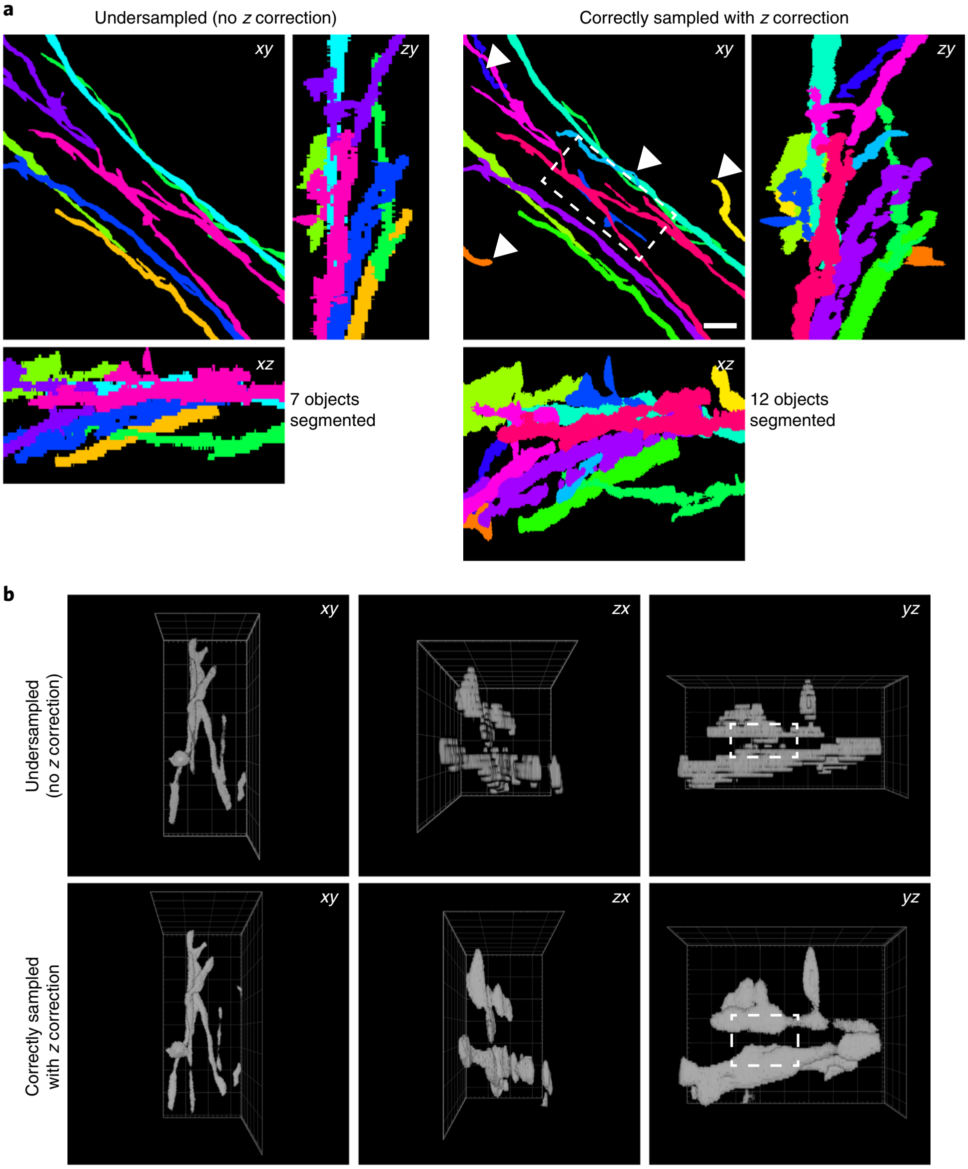

Fig. 6 | Correcting axial sampling improves segmentation. a, An N-class thresholding based on k-means classification (hierarchical k-means, Icy (http://icy.bioimageanalysis.org/download/)) automated segmentation routine was applied to the data in Fig. 5c. Each color represents an individually segmented object. Maximum intensity projections of the volume are presented along the *xy*, *xz*, and *zy* planes. White arrowheads indicate thin objects that are excluded in the undersampled dataset because of their *z* compression. Scale bar, 10 μm. **b**, 3D renderings of the white boxed region in **a** (right-hand *xy* image). Volume renderings along the *xy*, *zx*, and *yz* axes are shown. White dashed boxes in the *yz* images highlight an area that is poorly segmented in the undersampled data. White grids in background measure 10 × 10 μm.

An ImageJ/Fiji-based macro for axial distortion correction and optimal *z*-step determination

Equations 2 and 3 allow less complex calculations than wave optics methods but are still not simple enough for rapid manual calculation. Therefore, we have developed an ImageJ/Fiji-based[18,19] macro that allows researchers to (i) ensure the highest achievable axial resolution and prevent excess phototoxicity by calculating the optimal *z* step for their experiment before imaging and (ii) correct any axial distortions (compression or stretch) after imaging (see Box 1 for a step-by-step procedure for installation and application of the macro). The macro is run before imaging to calculate an optimal axial sampling rate (use the 'Provide recomended Z-step only' option as indicated in Box 1, step 8A(iv)). After imaging is complete, the macro is rerun to adjust the *z* spacing of the acquired dataset and correct SA-induced axial distortion using Eqs. 2 and/or 3 (Box 1, step 8A(viii–xiv)). If sufficient metadata exist, the macro will warn users if their acquisition *z* step was too large during imaging and thus limited the achievable axial resolution.

Mean versus median correction factor

Equations 2 and 3 present two ray optics–based approaches for calculating a correction factor for SA-induced axial distortion.

Box 1 | Installation and application of the focal shift correction macro ● Timing Installation: 15 min; calculate sampling rate: 2 min; correcting axial distortion: minutes to hours depending on number and size of files

This box provides a step-by-step procedure for the installation (Steps 1–7) and use (Step 8) of the macro. The source code can be copied directly from the Supplementary Software. Correct use of the macro before image acquisition (Step 8A(i–v)) will ensure that the full resolving power of the microscope is utilized. Following acquisition, Step 8A(vii–xiv) describes how to correct RI mismatch–induced axial distortion before 3D visualization and analysis. Alternatively, the post-acquisition processing steps can be avoided if a microscope's control software allows the input of RI-mismatch correction factors (Step 8B).

Macro installation procedure

1 Install or update to the current version of ImageJ[19] (https://imagej.nih.gov/ij/download.html) or Fiji[18] (https://fiji.sc/). If using ImageJ, you must also install a current version of the Bioformats plugin (https://docs.openmicroscopy.org/bio-formats/5.8.2/users/imagej/installing.html).
2 Open ImageJ/Fiji.
3 Open a new macro editor window ('Plugins' > 'New' > 'Macro').
4 Copy the source code from the Supplementary Software and paste it into the macro editor window.
5 On the 'Language' dropdown menu, select 'IJ1 Macro'.
6 Click 'File' > 'Save as' and save the macro to the ImageJ 'plugins' folder. The file name must contain an underscore ('_').
7 Restart ImageJ/Fiji and locate the macro at the bottom of the 'Plugins' dropdown menu.

Procedure for using the macro

8 To use the macro to calculate an optimal axial sampling rate (before image acquisition) and correct axially distorted images after acquisition, follow option A. To use the macro in conjunction with microscope control software that allows user-input RI mismatch correction factors, follow option B.
  (A) **Using the macro to calculate an optimal axial sampling rate and correct axially distorted images**
    (i) Ensure that the macro is saved in the ImageJ/Fiji 'plugins' folder (see step 6 above).
    (ii) Run the macro by selecting it from the 'Plugins' menu.
    (iii) Fill in the requested information as shown in the example screenshot below:

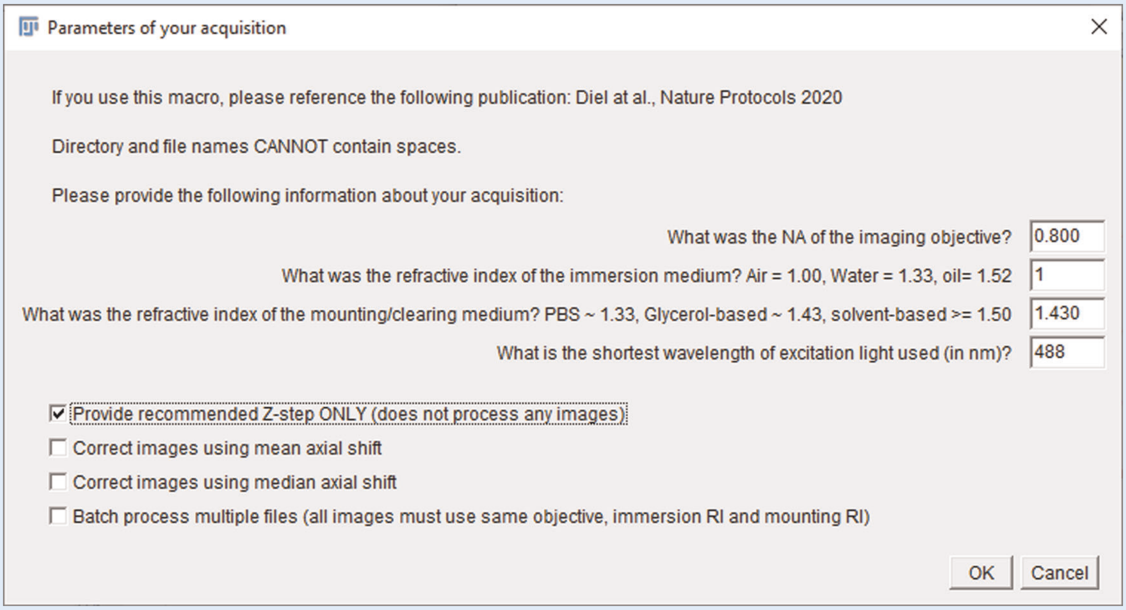

If you use this macro, please reference the following publication: Diel at al., Nature Protocols 2020

Directory and file names CANNOT contain spaces.

Please provide the following information about your acquisition:

What was the NA of the imaging objective? 0.800
What was the refractive index of the immersion medium? Air = 1.00, Water = 1.33, oil= 1.52 1
What was the refractive index of the mounting/clearing medium? PBS ~ 1.33, Glycerol-based ~ 1.43, solvent-based >= 1.50 1.430
What is the shortest wavelength of excitation light used (in nm)? 488

☑ Provide recommended Z-step ONLY (does not process any images)
☐ Correct images using mean axial shift
☐ Correct images using median axial shift
☐ Batch process multiple files (all images must use same objective, immersion RI and mounting RI)

    (iv) Check 'Provide recommended Z-step ONLY' to output the recommended *z* step without processing any data.
    (v) Click 'OK'. The recommended *z* step will be printed in the ImageJ/Fiji 'Log' window.
    (vi) Proceed to the microscope to image the sample.
    (vii) Enter the macro's recommended *z* step into the corresponding location of the microscope control software.
    (viii) Once imaging is completed, place all Bioformats-compatible image files (such as ome.tif, .czi, .lif, .nd2, .oif files) to be processed into a single folder (directories, subdirectories and files names must not contain spaces).
    (ix) Create an empty 'output' folder.
    (x) Run the macro by selecting it from the 'Plugins' menu in ImageJ/Fiji.
    (xi) Fill in the requested information as shown in the example screenshot above (step 8A(iii)).
    (xii) Check 'Correct images using mean axial shift' to use Eq. 2 (mean) and/or 'Correct images using median axial shift' to use Eq. 3 (median) when calculating the *z*-correction factor.
    (xiii) Check 'Batch process multiple files' if more than one image is to be processed (all images must have been acquired using the same conditions: NA, immersion RI, mounting RI) and click 'OK'.
    (xiv) Locate the input and output folders when requested. The corrected images will be saved to the output folder as .tif stacks and can be opened directly.

Box 1 | (continued)

(B) **Using the macro together with microscope acquisition software with an RI mismatch correction function**
  (i) Ensure that the macro is saved in the ImageJ/Fiji 'plugins' folder (see step 6 above).
  (ii) Run the macro by selecting it from the 'Plugins' menu.
  (iii) Fill in the requested information as shown in the example screenshot above.
  (iv) Check 'Provide recommended Z-step ONLY'.
  (v) Click 'OK'. Along with the recommended *z* step, an axial distortion correction factor will be printed in the ImageJ/Fiji 'Log' window.
  (vi) Proceed to the microscope to image the sample.
  (vii) Enter the macro's recommended *z* step in the corresponding location of the microscope control software.
  (viii) Enter the macro's recommended axial correction factor in the corresponding location of the microscope control software (screenshot below displays location for Carl Zeiss' ZEN Black or Blue software).

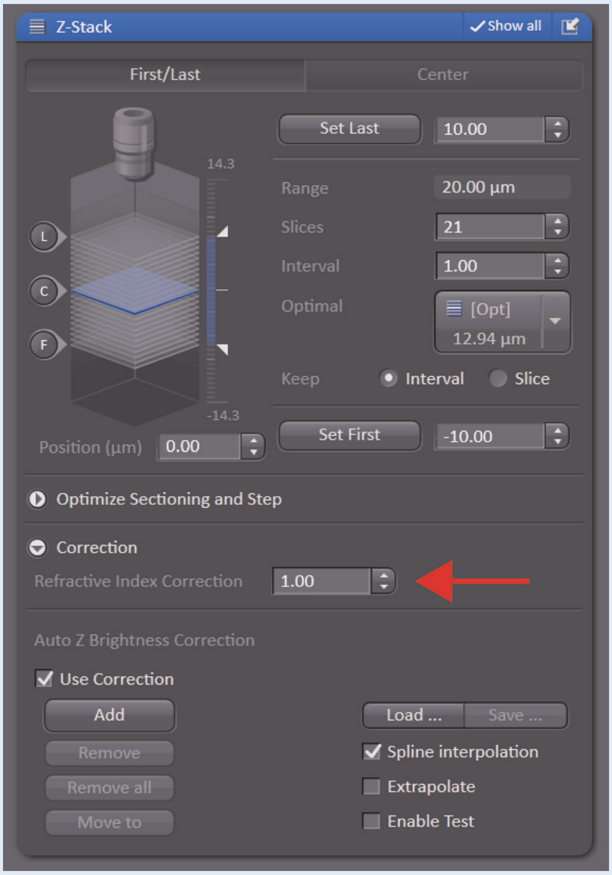

Set Last 10.00
Range 20.00 µm
Slices 21
Interval 1.00
Optimal [Opt] 12.94 µm
Keep ● Interval ○ Slice
Position (µm) 0.00
Set First -10.00
Refractive Index Correction 1.00
☑ Use Correction
☑ Spline interpolation
☐ Extrapolate
☐ Enable Test

  (ix) No further processing is required after image acquisition.

Equation 2 calculates the mean intersection point of 100 rays with the optical axis, whereas Eq. 3 calculates the median intersection point. For objectives with low NA (< ~0.5) imaging through minimal RI mismatches (< ~0.15), the two methods calculate nearly identical correction factors (Fig. 2). At higher NA (>0.5) and larger RI mismatches (>0.15), Eqs. 2 and 3 differ slightly but agree well with the wave optics calculations of Hell et al. (Fig. 2). Equation 2 calculates a higher degree of correction at high NA and large RI differences, whereas Eq. 3 (median) determines less correction is required relative to wave optics. Of the ray optics approaches investigated here, Eqs. 2 and 3 show the closest agreement to wave optics calculations across various NAs and RIs when imaging from a high-RI medium into a lower-RI sample (Fig. 2). The differences in correction factors calculated by Eqs. 2 and 3 and wave optics formulas are minimal. For example, the calculated focal shift for a 1.3-NA oil immersion objective imaging into a RI = 1.333 water solution are all within 20 nm of one another, well below the resolving power of the microscope. Although we do not have wave optics data for the inverse situation (imaging from a low-RI immersion medium into a higher-RI sample), Eqs. 2 and 3 are still in good agreement with one another (Fig. 3). Both equations show a response to increasing NA (unlike Carlsson), but neither is as heavily influenced by NA as Visser et al. (Fig. 3a). Therefore, Eqs. 1 and 2 provide accurate correction factors for imaging through high to low or low to high RI mismatches.

Limitations of the macro

The macro is not able to correct the lateral or axial blur that is introduced by SA or improve lateral or axial resolution after acquisition. SA-induced blur increases with objective NA and imaging depth. Increases in computing power now allow deconvolution to be applied to large 3D datasets, and deconvolution has been used to correct for the blur and axial shift induced by SA. SA correction via deconvolution requires a model of the blur introduced by SA and other factors such as diffraction within the entire optical path (microscope and sample), called the point spread function (PSF). Theoretical PSFs can be calculated, but they do not always consider SA and are commonly isometric in the axial dimension. Therefore, care must be taken when using theoretical PSFs to ensure that a model of SA blur is included and that axial shifts are corrected. Both open-source and commercial software are available for performing this level of deconvolution[20,21]. In addition, experimentally determined PSFs can be measured and used for deconvolution. Experimental PSFs can be obtained by imaging beads submerged in the sample mounting medium at various depths under a coverslip (Fig. 4a). For relatively thin samples, beads placed at a depth of half the sample's thickness may suffice. For thick samples, PSFs measured at multiple distances may be necessary[22–24].

Reporting Summary

Further information on research design is available in the Nature Research Reporting Summary linked to this article.

Data availability

All original (raw) data are available from the authors upon reasonable request.

Code availability

All necessary code and instructions for running the axial correction macro are provided in the Supplementary Software and Box 1.

References

1. Gibson, S. F. & Lanni, F. Experimental test of an analytical model of aberration in an oil-immersion objective lens used in three-dimensional light microscopy. *J. Opt. Soc. Am. A* **9**, 154–166 (1992).
2. Zhang, Q. et al. Quantitative refractive index distribution of single cell by combining phase-shifting interferometry and AFM imaging. *Sci. Rep.* **7**, 2532 (2017).
3. Keller, H. E. Objectives for confocal microscopy. in *Handbook of Biological Confocal Microscopy* (ed Pawley, J. B.) (Springer, 1995).
4. Jonkman, J., Brown, C. M., Wright, G. D., Anderson, K. I. & North, A. J. Tutorial: guidance for quantitative confocal microscopy. *Nat. Protoc.* **15**, 1585–1611 (2020).
5. Heine, J. et al. Three dimensional live-cell STED microscopy at increased depth using a water immersion objective. *Rev. Sci. Instrum.* **89**, 053701 (2018).
6. Schmidt, N. C., Kahms, M., Huve, J. & Klingauf, J. Intrinsic refractive index matched 3D dSTORM with two objectives: comparison of detection techniques. *Sci. Rep.* **8**, 13343 (2018).
7. Dodt, H. U. et al. Ultramicroscopy: development and outlook. *Neurophotonics* **2**, 041407 (2015).
8. Engelbrecht, C. J. & Stelzer, E. H. Resolution enhancement in a light-sheet-based microscope (SPIM). *Opt. Lett.* **31**, 1477–1479 (2006).
9. Ji, N. Adaptive optical fluorescence microscopy. *Nat. Methods* **14**, 374–380 (2017).
10. Patwary, N., King, S. V., Saavedra, G. & Preza, C. Reducing effects of aberration in 3D fluorescence imaging using wavefront coding with a radially symmetric phase mask. *Opt. Express* **24**, 12905–12921 (2016).
11. Richardson, D. S. & Lichtman, J. W. Clarifying tissue clearing. *Cell* **162**, 246–257 (2015).
12. Chung, K. et al. Structural and molecular interrogation of intact biological systems. *Nature* **497**, 332–337 (2013).
13. Renier, N. et al. iDISCO: a simple, rapid method to immunolabel large tissue samples for volume imaging. *Cell* **159**, 896–910 (2014).
14. Carlsson, K. The influence of specimen refractive-index, detector signal integration, and nonuniform scan speed on the imaging properties in confocal microscopy. *J Microsc.-Oxford* **163**, 167–178 (1991).
15. Visser, T. D., Oud, J. L. & Brakenhoff, G. J. Refractive-index and axial distance measurements in 3-D microscopy. *Optik* **90**, 17–19 (1992).
16. Sheppard, C. J., Gu, M., Brain, K. & Zhou, H. Influence of spherical aberration on axial imaging of confocal reflection microscopy. *Appl. Opt.* **33**, 616–624 (1994).
17. Hell, S., Reiner, G., Cremer, C. & Stelzer, E. H. K. Aberrations in confocal fluorescence microscopy induced by mismatches in refractive-index. *J. Microsc.* **169**, 391–405 (1993).
18. Schindelin, J. et al. Fiji: an open-source platform for biological-image analysis. *Nat. Methods* **9**, 676–682 (2012).
19. Schneider, C. A., Rasband, W. S. & Eliceiri, K. W. NIH Image to ImageJ: 25 years of image analysis. *Nat. Methods* **9**, 671–675 (2012).
20. Ghosh, S. & Preza, C. Fluorescence microscopy point spread function model accounting for aberrations due to refractive index variability within a specimen. *J. Biomed. Opt.* **20**, 75003 (2015).
21. Model, M. A., Fang, J., Yuvaraj, P., Chen, Y. & Zhang Newby, B. M. 3D deconvolution of spherically aberrated images using commercial software. *J. Microsc.* **241**, 94–100 (2011).
22. Kim, B. & Naemura, T. Blind depth-variant deconvolution of 3D data in wide-field fluorescence microscopy. *Sci. Rep.* **5**, 9894 (2015).
23. Preza, C. & Conchello, J. A. Depth-variant maximum-likelihood restoration for three-dimensional fluorescence microscopy. *J. Opt. Soc. Am. A* **21**, 1593–1601 (2004).
24. Ghosh, S. & Preza, C. Three-dimensional block-based restoration integrated with wide-field fluorescence microscopy for the investigation of thick specimens with spatially variant refractive index. *J. Biomed. Opt.* **21**, 46010 (2016).

Acknowledgements

We thank S. Piccinotti and L. Rubin for providing organoid samples. We thank the Harvard Center for Biological Imaging for infrastructure and support. J.W.L. was supported by the following funding sources: National Institutes of Health grants P50 MH094271, U24 NS109102, and U19 NS104653 and Department of Defense MURI award GG008784.

Author contributions

The idea for calculating axial distortion correction factors as described in this tutorial was conceived by D.S.R. and J.W.L. E.E.D. and D.S.R. carried out experiments and analyzed data. D.S.R., J.W.L. and E.E.D. wrote the manuscript. All authors contributed to editing the final manuscript.

Competing interests

The authors declare no competing interests.

Additional information

Supplementary information is available for this paper at https://doi.org/10.1038/s41596-020-0360-2.

Correspondence and requests for materials should be addressed to D.S.R.

Peer review information *Nature Protocols* thanks Chrysanthe Preza and the other, anonymous, reviewer(s) for their contribution to the peer review of this work.

Reprints and permissions information is available at www.nature.com/reprints.

Publisher's note Springer Nature remains neutral with regard to jurisdictional claims in published maps and institutional affiliations.

Received: 15 October 2019; Accepted: 18 May 2020;
Published online: 31 July 2020

Related links

References that contributed to the development of this protocol

Visser, T. D. et al. *Optik* **90**, 17–19 (1992): https://www.researchgate.net/publication/285251956_Refractive_index_and_axial_distance_measurements_in_3-D_microscopy

Hell, S., Reiner, G., Cremer, C. & Stelzer, E. H. K. *J. Microsc.* **169**, 391–405, (1993): https://onlinelibrary.wiley.com/doi/abs/10.1111/j.1365-2818.1993.tb03315.x nature research

Corresponding author(s): Douglas S Richardson

Last updated by author(s): Apr 8, 2020

Reporting Summary

Nature Research wishes to improve the reproducibility of the work that we publish. This form provides structure for consistency and transparency in reporting. For further information on Nature Research policies, see Authors & Referees and the Editorial Policy Checklist.

Statistics

For all statistical analyses, confirm that the following items are present in the figure legend, table legend, main text, or Methods section.

n/a	Confirmed	
☐	☒	The exact sample size (*n*) for each experimental group/condition, given as a discrete number and unit of measurement
☐	☒	A statement on whether measurements were taken from distinct samples or whether the same sample was measured repeatedly
☒	☐	The statistical test(s) used AND whether they are one- or two-sided *Only common tests should be described solely by name; describe more complex techniques in the Methods section.*
☒	☐	A description of all covariates tested
☒	☐	A description of any assumptions or corrections, such as tests of normality and adjustment for multiple comparisons
☒	☐	A full description of the statistical parameters including central tendency (e.g. means) or other basic estimates (e.g. regression coefficient) AND variation (e.g. standard deviation) or associated estimates of uncertainty (e.g. confidence intervals)
☒	☐	For null hypothesis testing, the test statistic (e.g. *F*, *t*, *r*) with confidence intervals, effect sizes, degrees of freedom and *P* value noted *Give P values as exact values whenever suitable.*
☒	☐	For Bayesian analysis, information on the choice of priors and Markov chain Monte Carlo settings
☒	☐	For hierarchical and complex designs, identification of the appropriate level for tests and full reporting of outcomes
☒	☐	Estimates of effect sizes (e.g. Cohen's *d*, Pearson's *r*), indicating how they were calculated

Our web collection on statistics for biologists contains articles on many of the points above.

Software and code

Policy information about availability of computer code

Data collection	ZEN Black version 2.6 (Carl Zeiss Microscopy) microscope control software was used for image acquisition.
Data analysis	Vision 4D version 3.1 (arivis AG), Fiji version 1.52p and Icy version 2.0.3.0 were used for image analysis

For manuscripts utilizing custom algorithms or software that are central to the research but not yet described in published literature, software must be made available to editors/reviewers. We strongly encourage code deposition in a community repository (e.g. GitHub). See the Nature Research guidelines for submitting code & software for further information.

Data

Policy information about availability of data

All manuscripts must include a data availability statement. This statement should provide the following information, where applicable:

- Accession codes, unique identifiers, or web links for publicly available datasets
- A list of figures that have associated raw data
- A description of any restrictions on data availability

All original (raw) data is available from the authors upon reasonable request.

Field-specific reporting

Please select the one below that is the best fit for your research. If you are not sure, read the appropriate sections before making your selection.

☒ Life sciences ☐ Behavioural & social sciences ☐ Ecological, evolutionary & environmental sciences

For a reference copy of the document with all sections, see nature.com/documents/nr-reporting-summary-flat.pdf

Life sciences study design

All studies must disclose on these points even when the disclosure is negative.

Sample size	3-5 data points were measured for each experimental condition. All data points showed little variability and closely agreed with calculated theoretical values. Therefore, these sample sizes were deemed sufficient.
Data exclusions	No data was excluded.
Replication	All replications were successful and agreed closely to theoretical calculations. All individual data points are reported in the figures.
Randomization	No statistical analysis was done to compare groups. All measurements were compared to theoretical calculations.
Blinding	Blinding was not relevant as no statistical analysis was done to compare groups.

Reporting for specific materials, systems and methods

We require information from authors about some types of materials, experimental systems and methods used in many studies. Here, indicate whether each material, system or method listed is relevant to your study. If you are not sure if a list item applies to your research, read the appropriate section before selecting a response.

Materials & experimental systems

n/a	Involved in the study
☒	☐ Antibodies
☒	☐ Eukaryotic cell lines
☒	☐ Palaeontology
☐	☒ Animals and other organisms
☒	☐ Human research participants
☒	☐ Clinical data

Methods

n/a	Involved in the study
☒	☐ ChIP-seq
☒	☐ Flow cytometry
☒	☐ MRI-based neuroimaging

Animals and other organisms

Policy information about studies involving animals; ARRIVE guidelines recommended for reporting animal research

Laboratory animals	Adult C57BL/6J male mice were used
Wild animals	Study did not involve wild animals
Field-collected samples	Study did not include field-collected samples
Ethics oversight	All experiments were conducted in accordance with procedures approved by the Institutional Animal Care and Use Committees of Harvard University.

Note that full information on the approval of the study protocol must also be provided in the manuscript.

Sample Mounting Methods

For reference, these are the HCBI's suggestions on how best to mount cleared tissue samples for imaging.

Example 1: Use for thin (<500 um) samples. (NOT FOR SOLVENT-CLEARED SAMPLES)

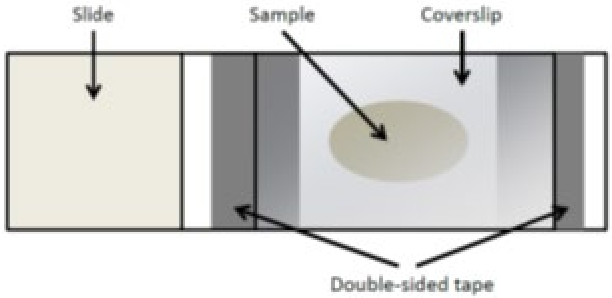

1) Layer double-sided tape on either side of your sample until it is of equal height (each layer of tape is approximately 50 um thick)
2) Place sample on slide and overlay with mountant (usually clearing solution)
3) Place coverslip over sample and press onto tape
4) Seal one side with nail polish, wax, super glue or epoxy (Loctite 401 works very well). Samples need to be imaged immediately when sealed with nailpolish).
5) Add mountant if necessary
6) Seal opposite side with nailpolish, wax, super glue, or epoxy

Alternative: 35mm coverslip bottom dish mounting

1) Place sample on dish
2) If sample is likely to move, embed in a thin film of 2% low melt point agarose (dissolved in the mountant and melted) or add a small drop of KrazyGlue or Loctite 401 to each side
3) Optional – sample can also be embedded in 2% agarose and mounted on dish prior to final clearing step. Apply final clearing solution and clear in place before imaging.
4) Apply mountant to keep wet

Example 2: Use for thick (>500 um) samples (THIS IS COMPATIBLE WITH SOLVENT-CLEARED SAMPLES)

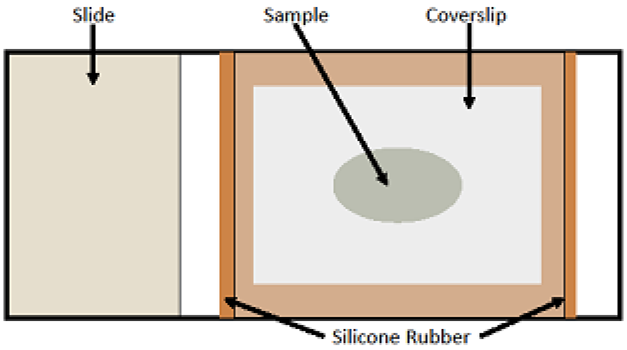

1) Cut a piece of silicon rubber (1 mm thick) approximately 1” x 1.5”.
2) Cut a hole in the middle large enough for your sample
3) Run a thin bead of Loctite 401 glue around the square ~ 2 mm from the inner edge.
4) Press a microscope slide on top ensuring that there are no gaps in the Loctite seal, but try to prevent any Loctite from entering the sample area
5) Place sample on slide and overlay with mountant (usually clearing solution)
6) Place coverslip over sample and press onto silicone. Be careful not to trap too many air bubbles. Some solution will leak out, this is OK.
7) Seal the edges of the coverslip with Loctite 401. Solvent-cleared samples should be imaged right away as they will oxidize and slowly go cloudy.

Example 3: Sample mounting for microscopes with multi-view sample chambers

1) Obtain or 3D print a mounting pedestal that can be attached to your rotation stage
2) Place a small drop of KrazyGlue on the end
3) Hold the capillary against a DRY, FLAT area of your tissue (orient the long axis of the tissue parallel to the capillary – see diagram) for ~30 s.

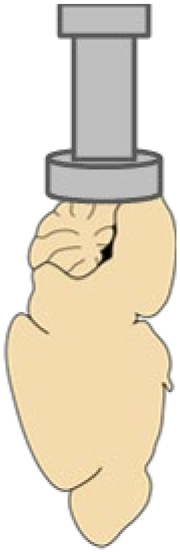

4) Invert the sample, allow glue to dry for further 2-3 mins, prior to placing into the microscope.

HARVARD
CBI

Thank you to our sponsors!

ZEISS

logos biosystems

lifecanvas technologies

BRUKER

Nikon

Leica

3i Intelligent Imaging Innovations